UC San Diego

UC San Diego Electronic Theses and Dissertations

Title

Utilizing the Redox Activity of Polyoxometalates: Electrocrystallization of Metal Oxide Networks and Thermogalvanic Electrolytes

Permalink

https://escholarship.org/uc/item/2t73k9vg

Author

Chang, Haeun

Publication Date

2024

Peer reviewed|Thesis/dissertation

eScholarship.org Powered by the California Digital Library
University of California

UNIVERSITY OF CALIFORNIA SAN DIEGO

Utilizing the Redox Activity of Polyoxometalates: Electrocrystallization of Metal Oxide Networks and Thermogalvanic Electrolytes

A Dissertation submitted in partial satisfaction of the requirements
for the degree Doctor of Philosophy

in

Chemistry

by

Haeun Chang

Committee in charge:

Professor Alina M. Schimpf, Chair
Professor Guy Bertrand
Professor Renkun Chen
Professor Andrew C. Kummel
Professor Julia M. Stauber

2024

Copyright

Haeun Chang, 2024

All rights reserved.

The Dissertation of Haeun Chang is approved, and it is acceptable in quality and form for publication on microfilm and electronically.

University of California San Diego

2024

DEDICATION

To my family

TABLE OF CONTENTS

DISSERTATION APPROVAL PAGE iii

DEDICATION iv

TABLE OF CONTENTS v

LIST OF FIGURES vii

LIST OF TABLES xi

ACKNOWLEDGEMENTS xii

VITA xiv

ABSTRACT OF THE DISSERTATION xv

Chapter 1 Introduction 1

1.1 Polyoxometalates 1

1.2 Redox properties of POMs 2

1.3 Electrochemical synthesis of polyoxometalate-based coordination networks 3

1.4 Polyoxometalates as thermogalvanic cell electrolytes 8

REFERENCES 11

Chapter 2 General Methods 19

2.1 General synthesis 19

2.2 General electrochemical cell setup for electrocrystallization 21

2.3 Variable-temperature cyclic voltammetry 21

REFERENCES 23

Chapter 3 Electrocrystallization of Preyssler-Based Metal Oxide Coordination Networks 24

3.1 Introduction 24

3.2 Results and Discussion 26

3.4 Conclusion 35

3.5 Supplemental Information 36

REFERENCES 63

Chapter 4 Polyoxometalates as Thermogalvanic Electrolytes.....67

4.1 Introduction.....67

4.2 Results and Discussion.....68

4.3 Supplemental Information.....75

REFERENCES 90

LIST OF FIGURES

Figure 1.1. Families of polyoxometalates. Reprinted with permission from reference 2. 2

Figure 1.2. Previously reported Preyssler-based all-inorganic metal-oxide frameworks. Reprinted with permission from *J. Am. Chem. Soc.* **2019**, *141* (51), 20261–20268. Copyright 2019 American Chemical Society. 5

Figure 1.3. Electrocrystallization experimental set-up example. Reprinted with permission from *Chem. Mater.* **1998**, *10* (10), 3005–3015. Copyright 1998 American Chemical Society. 7

Figure 2.1. An example of electrochemical cell set up for temperature-dependent cyclic voltammetry. 22

Figure 3.1. Crystal structure of Co-{P_5W_{30}} shown in (001) direction. 26

Figure 3.2. Representation of O_{cap1}–Co–O_{cap2} connections in Co-{P_5W_{30}}. 28

Figure 3.3. Representation of $Co_2(H_2O)_9$ motif resulting from O_{belt}–Co connections in Co-{P_5W_{30}}. 28

Figure 4.1. Cyclic voltammogram of 1 mM {P_2W_{18}} in 0.1 M sodium acetate (pH = 3.5) measured at 21.5 °C. 71

Supplemental Figure 3.1. Powder X-ray diffraction patterns of (i) Co-{P_5W_{30}}, (ii) Ni-{P_5W_{30}}, and (iii) Zn-{P_5W_{30}} compared to (iv) powder pattern simulated from single-crystal X-ray diffraction data. 45

Supplemental Figure 3.2. W*4f* X-ray photoelectron spectra of Co-{P_5W_{30}}. 45

Supplemental Figure 3.3. Co*2p* X-ray photoelectron spectra of Co-{P_5W_{30}}. 46

Supplemental Figure 3.4. Electron titration of Co-{P_5W_{30}}. 46

Supplemental Figure 3.5. Thermogravimetric analysis data of Co-{P_5W_{30}}. Weight loss of 11.9 % is accounted for water lost from the structure. 47

Supplemental Figure 3.6. Thermogravimetric analysis data of Ni-{P_5W_{30}}. Weight loss of 11.2 % is accounted for water lost from the structure. 48

Supplemental Figure 3.7. Powder X-ray diffraction pattern of (i) Zn-{P_5W_{30}}, compared to simulated powder patterns of (ii) Zn^0 P63/mmc, and (iii) crystal structure of Zn-{P_5W_{30}}..... 48

Supplemental Figure 3.8. Preliminary crystal structure solution of single-crystal isolated from an electrocrystallization reaction of electrolytic solution of $K_{14}[NaP_5W_{30}O_{110}]\bullet 14H_2O$ (65.0 mg, 7.88 μmol) and $Y(OAc)_3\bullet 2H_2O$ (183.2 mg, 542.0 μmol) prepared in 10 ml of 0.05 M KOAc buffer (pH = 5.6). 49

Supplemental Figure 3.9. Simulated powder X-ray pattern of the preliminary structure shown in Supplemental Figure 3.8 compared to the experimental powder X-ray pattern of bulk product from the same reaction. 49

Supplemental Figure 3.10. FT-IR spectra of (i) {P_5W_{30}} and (ii) white precipitate isolated from {P_5W_{30}} addition to $Y(OAc)_3$ solution in 0.05 M $KOAc_{(aq)}$ (pH = 5.6). The IR spectrum of the precipitate shows characteristic peaks of {P_5W_{30}} in 2000–1000 cm^{-1}, suggesting that the

precipitate is result of aggregation between Y^{3+} and $\{P_5W_{30}\}$ due to strong ion pairing strength between two species. 50

Supplemental Figure 3.11. Crystal structure of Y-$\{P_5W_{30}\}$ 51

Supplemental Figure 3.12. Powder X-ray diffraction pattern of (i) Y-$\{P_5W_{30}\}$ and (ii) simulated powder patten from Y-$\{P_5W_{30}\}$ single-crystal X-ray diffraction data. 52

Supplemental Figure 3.13. Representation of O_{cap1}–Y–Y–O_{cap2} conncections in Y-$\{P_5W_{30}\}$ crystal structure. 53

Supplemental Figure 3.14. Representation of O_{belt}–Y connections in Y-$\{P_5W_{30}\}$ crystal structure 54

Supplemental Figure 3.15. FT-IR spectra of (i) anodic deposit during Co-$\{P_5W_{30}\}$ synthesis and (ii) $\{P_5W_{30}\}$. The IR spectrum of deposit shows characteristic P–O stretches of $\{P_5W_{30}\}$, supporting$\{P_5W_{30}\}$ incorporation in anodic byproduct. 55

Supplemental Figure 3.16. Powder X-ray diffraction pattern of (i) cathodic product from undivided cell synthesis with copper sacrificial anode, compared to simulated powder patterns of (ii) Cu *Fm-3m* and (iii) crystal structure of Co-$\{P_5W_{30}\}$. 56

Supplemental Figure 3.17. Powder X-ray diffraction pattern of (i) cathodic product from undivided cell synthesis with cobalt wire sacrificial anode, compared to (ii) simulated powder pattern of crystal structure of Co-$\{P_5W_{30}\}$. 57

Supplemental Figure 3.18. Powder X-ray diffraction pattern of (i) cathodic product of **divided cell** synthesis with cobalt sacrificial anode, compared to (i) simulated powder pattern of Co-$\{P_5W_{30}\}$ crystal structure. 57

Supplemental Figure 3.19. Scanning electron microscopy image of electrosynthesized Co-$\{P_5W_{30}\}$ crystals on cathode. 58

Supplemental Figure 3.20. Snapshot of video microscopy on Co-$\{P_5W_{30}\}$ single-crystal. 58

Supplemental Figure 3.21. Powder X-ray diffraction pattern of (i) metallic pellet isolated from cathodic surface after Co-{P5W30} synthesis, compared to (ii) simulated powder pattern of cobalt metal in P63/mmc space group. 59

Supplemental Figure 3.22. Powder X-ray diffraction patterns of Zn-$\{P_5MoW_{29}\}$ taken daily for 8 days since synthesis, compared to simulated powder pattern of preliminary crystal structure solved from day 4 sample. The network was exposed to air throughout the period. 59

Supplemental Figure 3.23. Preliminary crystal structure solution of Zn-$\{P_5MoW_{29}\}$ on day 4. 60

Supplemental Figure 3.24. Chronopotentiograms of (i) Co-$\{P_5W_{30}\}$, (ii) Ni-$\{P_5W_{30}\}$, (iii) Zn-$\{P_5W_{30}\}$, and (iv) Y-$\{P_5W_{30}\}$. 61

Supplemental Figure 3.25. ^{31}P NMR spectrum of $\{P_5W_{30}\}$ used for electrocrystallization of coordination networks. The phosphorus peak around -9.4 ppm is consistent with literature reported value.[26] 62

Supplemental Figure 3.26. Scheme of Co-$\{P_5W_{30}\}$ electrocrystallization in divided cell using sacrificial Co anode 62

Supplemental Figure 4.1. A typical setup for VTCV experiment. 76

Supplemental Figure 4.2. ^{31}P NMR spectrum of $\{P_5W_{30}\}$ in H_2O..... 77

Supplemental Figure 4.3. IR spectrum of $\{P_5W_{30}\}$..... 77

Supplemental Figure 4.4. Cyclic voltammograms of 1 mM $\{P_2W_{18}\}$ in 0.1 M sodium acetate (pH = 3.5) collected at 2 and 49 °C. The violet voltammogram was taken after cooling down the solution from 49 °C to 2 °C. 78

Supplemental Figure 4.5. Variable-temperature cyclic voltammograms of 1 mM $\{P_2W_{18}\}$ in 0.1 M sodium acetate (pH = 3.5) collected at 2.0 – 48.5 °C with a sweep rate of 100 mV/s..... 78

Supplemental Figure 4.6. Rates of cathodic peak (left column), half-wave (middle column), and anodic peak (right column) potential shifts per unit temperature change, extracted from VTCVs on 1 mM $\{P_2W_{18}\}$ in 0.1 M sodium acetate (pH = 3.5) for each redox process..... 79

Supplemental Figure 4.7. ΔSrc as a function of $Zox2 - Zred2$ for $\{P_2W_{18}\}$..... 80

Supplemental Figure 4.8. Variable-temperature cyclic voltammograms of 1 mM $\{P_2W_{18}\}$ in 0.1 M sodium acetate (pH = 5.9) collected at 2.0 – 49.0 °C with a sweep rate of 100 mV/s..... 81

Supplemental Figure 4.9. Rates of cathodic peak (left column), half-wave (middle column), and anodic peak (right column) potential shifts per unit temperature change, extracted from VTCVs on 1 mM $\{P_2W_{18}\}$ in 0.1 M sodium acetate (pH = 5.9) for each redox process..... 82

Supplemental Figure 4.10. VTCVs of 1 mM $\{P_2W_{18}\}$ in 1 M HCl(aq) collected at 19.0 – 48.9 °C temperature range with a sweep rate of 100 mV/s. 83

Supplemental Figure 4.11. Rates of cathodic peak (left column), half-wave (middle column), and anodic peak (right column) potential shifts per unit temperature change, extracted from VTCVs on 1 mM $\{P_2W_{18}\}$ in 1 M HCl(aq) for each redox process..... 84

Supplemental Figure 4.12. Variable-temperature cyclic voltammograms of 1 mM $\{P_5W_{30}\}$ in 1 M HCl(aq) collected at 20.0 – 51.0 °C with a sweep rate of 100 mV/s. 85

Supplemental Figure 4.13. Rates of cathodic peak (left column), half-wave (middle column), and anodic peak (right column) potential shifts per unit temperature change, extracted from VTCVs on 1 mM $\{P_5W_{30}\}$ in 1 M HCl(aq) for the first two redox processes. 85

Supplemental Figure 4.14. Variable-temperature cyclic voltammograms of 1 mM $\{P_5W_{30}\}$ solution prepared in 1 M HCl(aq) with 50 mM KCl, measured in the temperature range of 22.0 – 48.0 °C at a sweep rate of 100 mV/s..... 86

Supplemental Figure 4.15. Rates of cathodic peak (left column), half-wave (middle column), and anodic peak (right column) potential shifts per unit temperature change, extracted from VTCVs on 1 mM $\{P_5W_{30}\}$ in 1 M HCl(aq) with 50 mM KCl for the first two redox processes. 86

Supplemental Figure 4.16. Variable-temperature cyclic voltammograms of 1 mM $\{P_5W_{30}\}$ solution prepared in 1 M HCl(aq) with 100 mM KCl, measured in the temperature range of 22.0 – 48.0 °C at a sweep rate of 100 mV/s..... 87

Supplemental Figure 4.17. Rates of cathodic peak (left column), half-wave (middle column), and anodic peak (right column) potential shifts per unit temperature change, extracted from VTCVs on 1 mM $\{P_5W_{30}\}$ in 1 M HCl(aq) with 100 mM KCl for the first two redox processes. 87

Supplemental Figure 4.18. Variable-temperature cyclic voltammograms of 1 mM {P_5MoW_{29}} solution prepared in 1 M HCl(aq) collected in 22.0 – 50.5 °C temperature range with 100 mV/s sweep rate. Only the first two redox processes are represented in this plot. 88

Supplemental Figure 4.19. (Top row) Rates of cathodic peak (left column), half-wave (middle column), and anodic peak (right column) potential shifts per unit temperature change, extracted from VTCVs on 1 mM {P_5MoW_{29}} in 1 M HCl(aq) for the first redox process. (Bottom row) Cathodic peak, half-wave, and anodic peak potentials measured at varied temperatures for the second redox process are shown without linear fits..... 89

Supplemental Figure 4.20. Full representations of variable-temperature cyclic voltammograms of 1 mM {P_5MoW_{29}} solution in 1 M HCl(aq). 89

LIST OF TABLES

Table 4.1. Charge square difference of redox couple ($Zox2 - Zred2$), number of electrons transferred (n), approximate Seebeck coefficients (Se), and calculated entropy change (ΔSrc) for each redox process of 1 mM $\{P_5W_{30}\}$ and $\{P_2W_{18}\}$ in 1 M HCl(aq). 74

Supplemental Table 3.1. Crystallographic parameters of electrochemically synthesized coordination networks. 40

Supplemental Table 3.2. Summary of Co connections in Co-$\{P_5W_{30}\}$ 41

Supplemental Table 3.3. Summary of Ni connections in Ni-$\{P_5W_{30}\}$. 42

Supplemental Table 3.4. Summary of Zn connections in Zn-$\{P_5W_{30}\}$. 43

Supplemental Table 3.5. Summary of Y connections in Y-$\{P_5W_{30}\}$. 44

Supplemental Table 3.6. Inductively coupled plasmon mass spectroscopy data of electrocrystallized coordination networks. 47

Supplemental Table 3.7. Enegy-dispersive X-ray spectroscopy data of anodic product of undivided cell Co-$\{P_5W_{30}\}$ synthesis with platinum wire anode. 55

ACKNOWLEDGEMENTS

First, I would like to thank Professor Alina M. Schimpf for her support and mentorship. I also extend my gratitude to all my committee members, past and present: Professor Guy Bertrand, Professor Renkun Chen, Professor Andrew C. Kummel, Professor Julia M. Stauber, and Professor Joshua S. Figueroa, for their invaluable guidance throughout the past six years.

The members of the Schimpf Group: Hankyeol, Jessica, Alec, Carl, Khin, Linfeng, Liana, Hang, Olivia, and Kody, made my day-to-day work enjoyable. Similarly, the members of the Figueroa Group: Vincent, Myles, Joanne, Alejandra, Mike, Adam, Ritchie, and Krista, inspired me daily.

I owe special thanks to Drs. Milan Gembicky, Jake Bailey, and Erika Samolova of the X-ray crystallography facility, who were the heroes of my work. I also thank Drs. Anthony Mrse and Xuemei Huang for their assistance with NMR, Dr. Neal Arakawa for his help with ICP-MS, and Ricardo De Luna for his help with TGA.

I am grateful to all members of the inorganic track of UCSD Chemistry Department for their generosity with reagents, instrumentation, and assistance. Drs. Thomas Chan and Nicole Torquato, thank you for training me on electrochemistry. I would also like to extend my sincere thanks to my collaborators at the University of Oregon, especially Professor Carl K. Brozek, Dr. Jiawei Huang, and Jacob McKenzie, for insightful discussion and being generous hosts.

I thank my friends, Drs. Deborah Kim, Stephanie Mora Garcia, and Liana Alves for being there for me throughout grad school. I extend a special thanks to Dr. Jeremy D. Hilgar for everything he is to me.

Lastly, I thank my mom, dad, sister and brother for their unwavering support and love.

Chapter 3, in part, is currently being prepared for submission for publication of the material. The dissertation author would like to acknowledge the contributions of the co-authors Linfeng Chen, Carl Lemmon, Erika Samolova, Milan Gembicky, and Alina M. Schimpf. The dissertation author was the primary researcher and author of this material.

The author would like to thank the collaborators Erik Svensson Grape, Jiawei Huang, Dwaipayan Roychowdhury, Tekalign T. Debela, Andrew Jenkins, Christopher H. Hendon, and Carl K. Brozek for collaborative work on the project that provided a foundation for the studies presented in Chapter 4.

VITA

2014 Bachelor of Engineering in Biotechnology, Yonsei University

2020 Master of Science in Chemistry, University of California San Diego

2024 Doctor of Philosophy in Chemistry, University of California San Diego

PUBLICATIONS

Svensson Grape, E.; Huang, J.; Roychowdhury, D.; Debela, T. T.; Chang, H.; Jenkins, A.; Schimpf, A. M.; Hendon, C. H.; Brozek, C. K. Converting Heat to Electrical Energy Using Highly Charged Polyoxometalate Electrolytes. *ACS Applied Energy Materials* **2024**. *Just accepted.*

Geisenhoff, J. Q.; Yin, H.; Oget, N.; Chang, H.; Chen, L.; Schimpf, A. M. Controlled CO Labilization of Tungsten Carbonyl Precursors for the Low-Temperature Synthesis of Tungsten Diselenide Nanocrystals. *Frontiers in Nanotechnology* **2022**, *4*, 2673–3013.

Kim, S.; Chang, H.; Choi, J.-Y.; Song, Y.; Heller, M. J. Ultrathin Sub-3 nm Nitrogen-Doped Graphene Quantum Dot Layers Coated TiO2 Nanocomposites as High-Performance Photocatalysts. *Chemical Physics Letters* **2019**, *714*, 1–5.

Xie, Y.; Vincent, A. H.; Chang, H.; Rinehart, J. D. Strengthening Nanocomposite Magnetism through Microemulsion Synthesis. *Nano Research* **2018**, *11* (8), 4133–4141.

Oh, T.; Kim, S.; Choi, J.-Y.; Chang, H.; Heller, M. J. Enhancement of Fluorescent Resonant Energy Transfer and the Antenna Effect in DNA Structures with Multiple Fluorescent Dyes. *RSC Advances* **2017**, *7* (24), 14902–14909.

ABSTRACT OF THE DISSERTATION

Utilizing the Redox Activity of Polyoxometalates: Electrocrystallization of Metal Oxide Networks and Thermogalvanic Electrolytes

by

Haeun Chang

Doctor of Philosophy in Chemistry

University of California San Diego, 2024

Professor Alina M. Schimpf, Chair

Polyoxometalates (POMs) are anionic metal oxo clusters composed of groups 5 and 6 transition metals such as vanadium, niobium, tantalum, molybdenum, and tungsten. These metals, in high oxidation states, are coordinated to terminal oxo ligands and connected through bridging oxo ligands, making POMs oxidation-inert but easily reducible. The reduction processes in POMs are reversible, which coupled with their structural integrity, makes them ideal

for developing novel materials for applications in energy storage and conversion, molecular electronics, and catalysis. This dissertation specifically discusses POM applications in the electrosynthesis of metal oxide frameworks and thermogalvanic cell electrolytes.

Chapter 3 presents the development of new coordination networks using Preyssler anions as modular building blocks using electrocrystallization, a method that uses electrochemical redox reactions to form crystalline compounds. The resulting structures exhibit one-dimensional chains connected through cap-to-cap coordination. Notably, these are the first examples of electrocrystallized Preyssler-based metal oxide coordination networks. The chapter details the synthetic processes, structural analysis, and characterization of these coordination networks.

Chapter 4 discusses the utilization of POMs as potential electrolytes in thermogalvanic cells, which are promising for converting low-grade thermal energy into electrical energy. The chapter presents two POM thermogalvanic systems based on Dawson and Preyssler-type clusters. The chapter covers the electrochemical analyses of the systems and discusses potential factors, such as ion concentration and pH, that could impact the S_e values.

Chapter 1 Introduction

1.1 Polyoxometalates

Polyoxometalates, often abbreviated as POMs, are anionic metal oxo clusters that are commonly composed of group 5 and 6 transition metals, such as vanadium, niobium, tantalum, molybdenum, and tungsten.[1] Metals of high oxidation states are coordinated to terminal oxo ligands and connected to each other through bridging oxo ligands in these discrete polyatomic molecules. Broadly, POMs are classified into two families, isopolymetalates and heteropolymetalates as shown in **Figure 1.1**.[2] Exemplified by Lindqvist structure ($[M_6O_{19}]^{n-}$), isopolymetalates consist of one metal element and oxygen. On the other hand, heteropolymetalates include multiple metal elements or oxyanions of main group elements as well in their compositions. Notable examples of heteropolymetalates are Keggin ($[XM_{12}O_{40}]^{n-}$; X = Si, P, B, M = W, Mo),[3] Wells–Dawson ($[X_2M_{18}O_{62}]^{n-}$; X = P, As, M = W, Mo),[4] and Preyssler ($[ZP_5W_{30}O_{110}]^{n-}$; Z = center cation[5]) clusters.

POMs of vanadium, molybdenum, and tungsten form through oxyanion condensation in low pH through a chemical process called olation.[6] Therefore, in general, syntheses of these POMs are done by dissolving orthometalate precursors in water or organic solvents and acidifying the solution. [7,8] The resulting clusters can be isolated by adding salts to the reaction to provide countercations and recrystallizing the compounds. Some polyoxovanadates, -molybdates, and -tungstates may lose metal oxyanions when exposed to high pH environment and form lacunary structures.[7,8] There are ways to alter the composition post-synthetically, such as counterion[9,10] or center cation exchanges,[10] and organic ligand functionalization.[11]

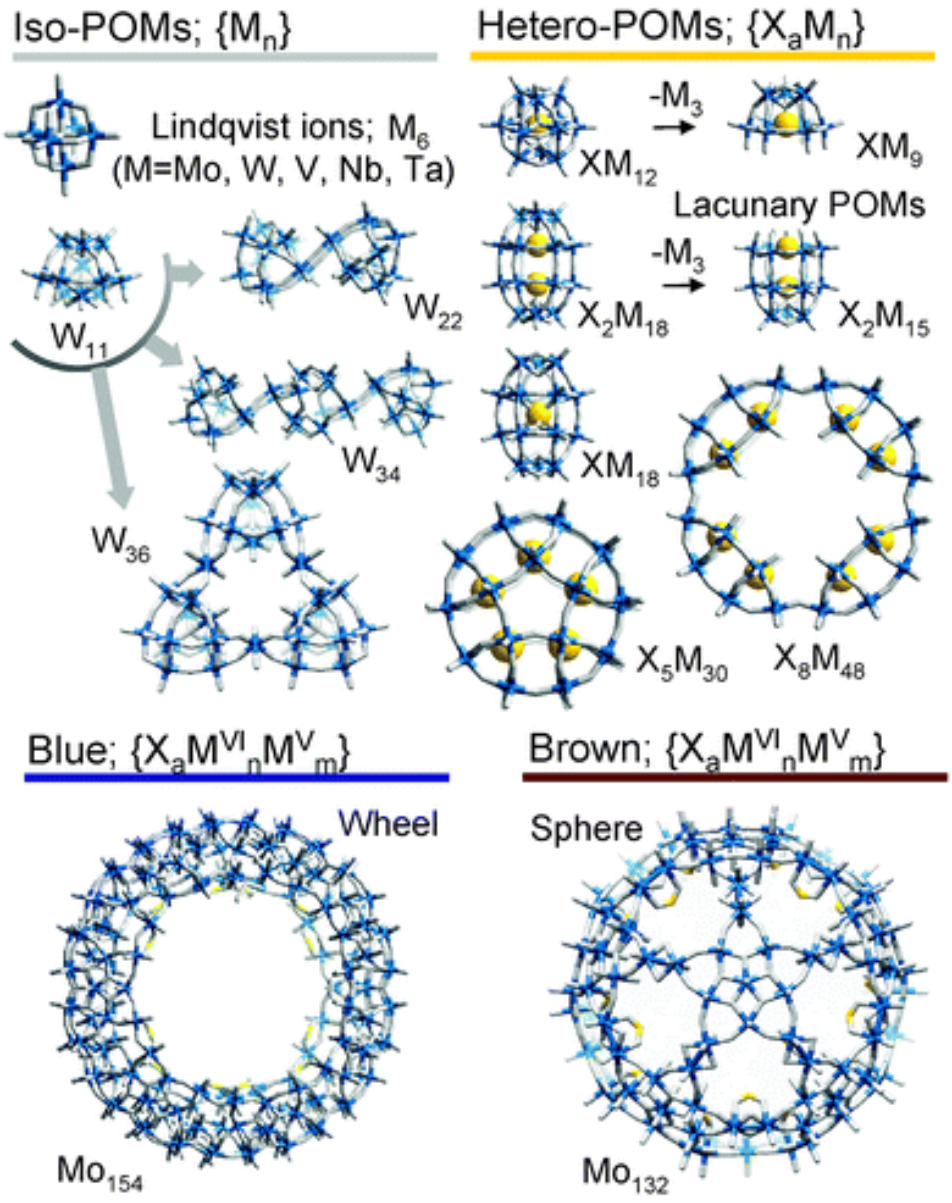


Figure 1.1. Families of polyoxometalates. Reprinted with permission from reference 2.

1.2 Redox properties of POMs

As mentioned above, metals in POMs are often in their high oxidation states. This makes POMs oxidation-inert, but easily reducible. Reducibility of POMs was first noted in Keggin-type polyoxomolybdate and -tungstate, $[XM_{12}O_{40}]^{3-}$ in 20th century.[12] Owing to the characteristic blue color seen in reduced POM species, the terms “molybdenum blue” and “heteropoly blue” were

coined to depict these reduced POM compounds. Further investigations on heteropoly blues discovered that reduction processes are reversible with marginal influence in structures in many different species of POMs, including Keggin-, Wells–Dawson-, and Preyssler-type anions.[13–15]

Owing to their reversible redox properties coupled with structural integrity, these clusters were used in developing novel materials with application in energy storage and conversion,[16,17] molecular electronics,[18–21] and catalysis.[22–25] Specifically, in the scope of this dissertation, POM applications in electrosynthesis of metal oxide frameworks and thermogalvanic cell electrolytes will be discussed.

1.3 Electrochemical synthesis of polyoxometalate-based coordination networks

1.3.1 Polyoxometalate-based metal oxide coordination networks

Bottom-up molecular self-assembly has greatly impacted material design over the past decades.[26] Through judicious choice of molecular building blocks, innumerous materials of atomic-precision with interesting structural, physicochemical and electrochemical properties were synthesized. Among such building blocks, POMs have gained a significant interest.[27–30] As molecular analogues of metal oxides, POMs share similarities in optical and electronic properties with those of semiconductor quantum dots.[31] They vary largely in structure and composition, and the high-nuclearity nature of these anionic clusters offers a wide range of reversible redox states.[32] These attractive features as a building block have been found useful in materials development for various applications, such as catalysis,[22,33–35] electronics,[36,37] magnetism,[38–41] and medicine.[42–44]

Undoubtedly, coordination networks are one of the most highlighted classes of molecular materials.[45,46] As they often feature high porosity and interesting electronic properties, coordination networks are desirable targets for material scientists. Recently, there has been an

appreciable effort in the community to incorporate POMs in coordination networks and utilize the rich chemistry of the clusters in porous of enviroments.[28,30] In particular, POM-based frameworks (POMFs) with all-inorganic composition have attracted attention as they offer a great opportunity to develop materials from metal oxide motifs with atom-defined tunability.[47–52] A new set of inorganic POMFs of Preyssler-type anions ($[ZP_5W_{30}O_{110}]^{14-}$, Z = Na^+, Sm^{3+}, Bi^{3+}), linked by a variety of first-row transition-metal cations, has been recently synthesized through simple solution-phase reactions (**Figure 1.2**).[53,54] With exceptional structural integrity even when reduced, this class of materials has shown its potential as a tunable molecular counterpart to solid-state metal oxides and is definitely worth of further development.

One of the ways to develop new POM-based molecular metal oxide frameworks is to employ a synthetic strategy that exploits the rich redox behavior of POMs. To leverage electroactivity of POMs as synthetic handle, electrocrystallization is a promising synthetic platform.

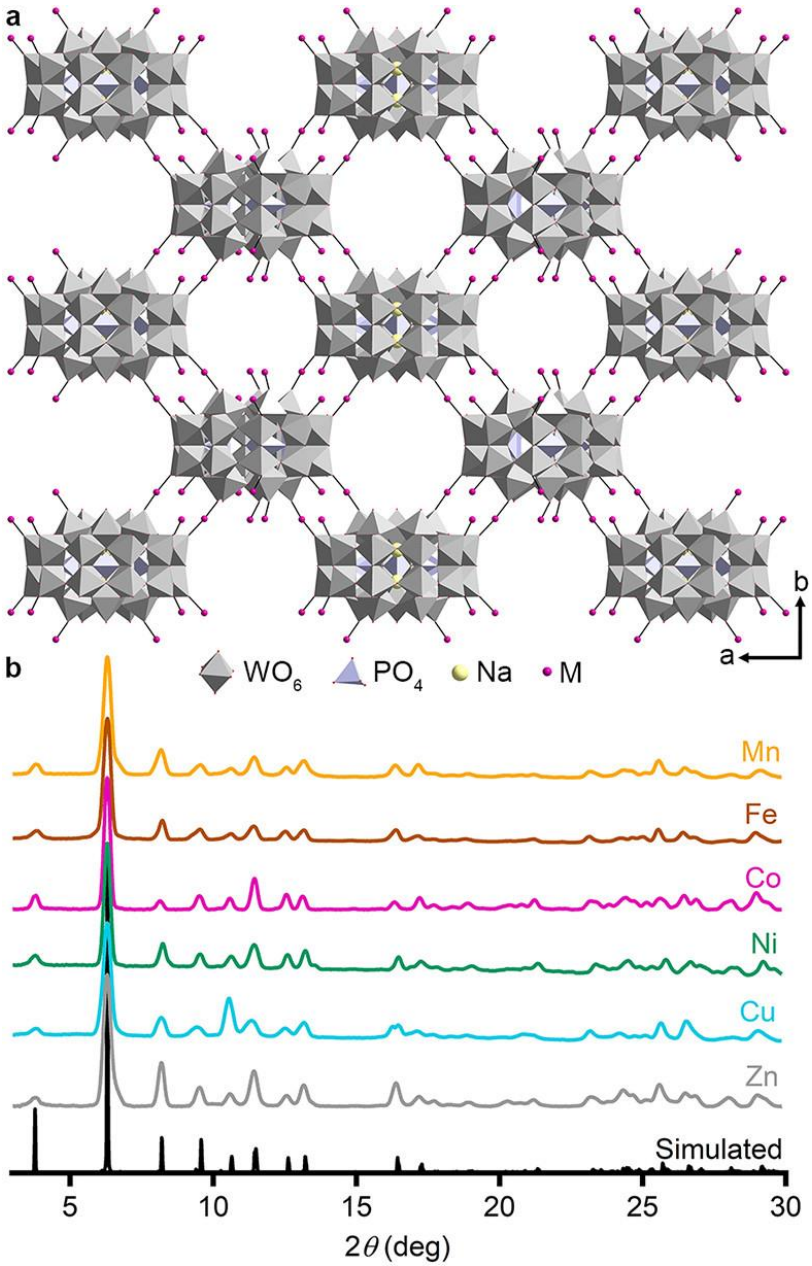


Figure 1.2. Previously reported Preyssler-based all-inorganic metal-oxide frameworks. Reprinted with permission from *J. Am. Chem. Soc.* **2019**, *141* (51), 20261–20268. Copyright 2019 American Chemical Society.

1.3.2 Electrocrystallization

Electrosynthesis, performed in an electrochemical cell, can achieve better selectivity and yield compared to conventional redox reactions using chemical reductants or oxidants.[55–58] The reaction conditions, including solvent, electrolyte, cell configurations, electrode materials, and

whether constant current or potential is used, are some of the factors to be considered when designing experiments.[57,59]

Electrocrystallization, a type of electrosynthesis, results in crystalline materials through electrochemical reduction or oxidation of the substrate, triggering crystallization. For example, reduction on the cathode leads to substrate crystallization with charge-balancing cations from the electrolyte, while anodic crystallization involves oxidation with charge-balancing anions (**Figure 1.3**).[60] It is possible that more than one species of charge-balancing ion or substrate of different redox states to be incorporated in crystal lattice in different stoichiometric ratios.[27,60]

Though constant potential can target specific substrate redox reactions, constant current is easier to set up but offers less control over side reactions, which can affect synthesis efficiency and product purity. Using constant current, however, provides a handle to control crystallization rate, and thus can achieve improved crystallinity.[59,60]

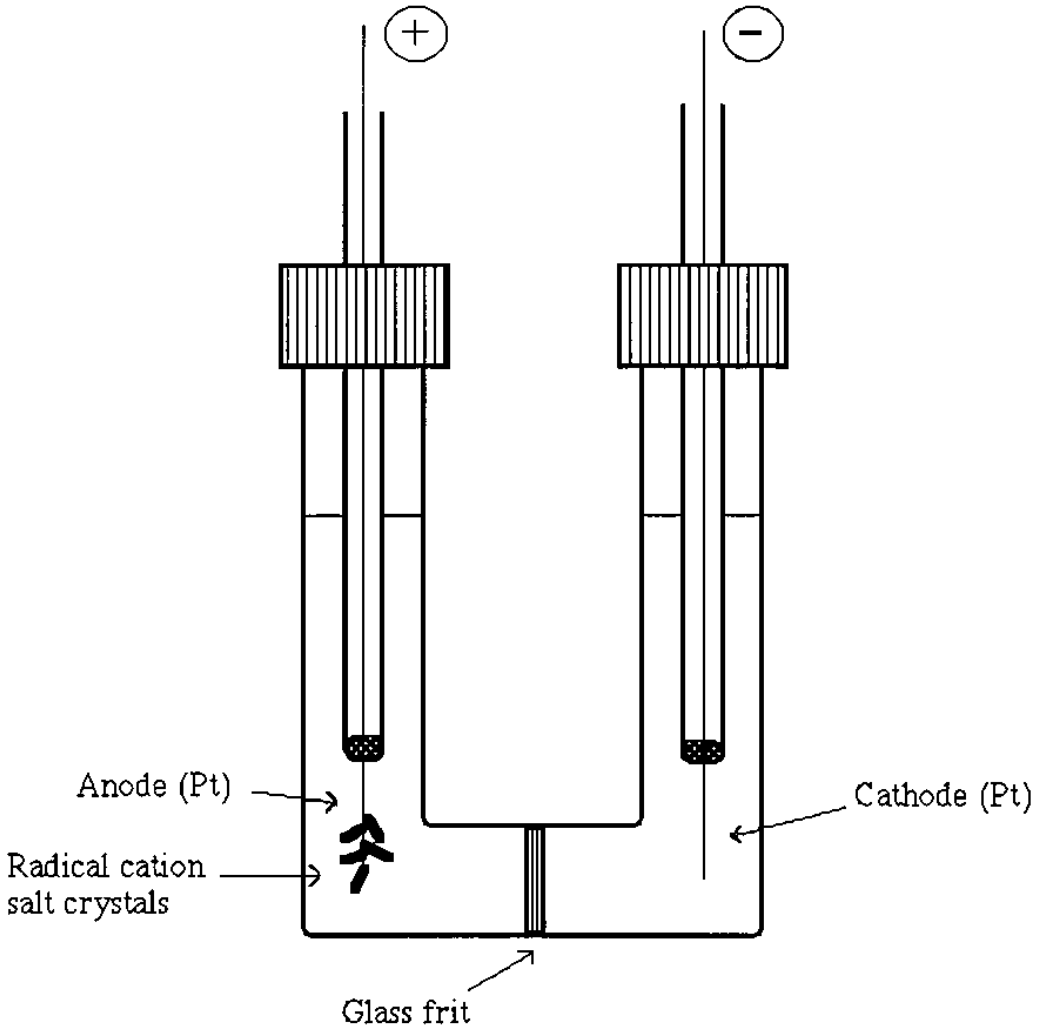


Figure 1.3. Electrocrystallization experimental set-up example. Reprinted with permission from *Chem. Mater.* **1998**, *10* (10), 3005–3015. Copyright 1998 American Chemical Society.

1.3.3 Electrocrystallization POM examples

Electrocrystallization was previously explored in developing POM-containing compounds. In the effort of development of polyoxometalate-based molecular conductors, polyoxometalates were used as counter inorganic anions to organic donor molecules to create charge-balancing salts through electrocrystallization. Polyoxometalates were chosen as they can accept electrons, coordinate to magnetically active metals, and have structural diversity which can act as a handle to tune electronic structures of donor-acceptor salts and control solubility in

organic solvents for successful electrocrystallization.[27,36] In [TTF][$PMo_{12}O_{40}$] salt synthesis, in particular, polyoxometalates were actively reduced at cathodes to trigger the electrochemical crystallization of the salt.[27,61]

Due to its anionic charge, polyoxometalates were used as templates to facilitate weaving of electroactive superatom monomers through anodic electrocrystallization. The 4-fold symmetry of $[Mo_6O_{19}]^{2-}$ guided the topology of the box weave, by ordering superatom monomers oxidized by one electron which enabled polymerization.[62]

Recently, Zhang et al. has developed bench-top electrolysis method to synthesize polyoxometalate-organic frameworks (POMOFs) and inorganic-organic hybrid compounds through electrocrystallization, utilizing polyoxovanadates $[V_{10}O_{28}]^{6-}$, Cu^{2+} salts, and organic compounds.[63,64]

1.4 Polyoxometalates as thermogalvanic cell electrolytes

1.4.1 Thermogalvanic cell principles

When primary source of energy goes through energy conversion to useful energy such as electricity, about 60% of the total source energy gets wasted as heat energy. Among this wasted heat, 66% is in the form of low-grade heat which is below 200 °C.[65] Considering the amount of energy that is being wasted in this form, finding ways to harvest low-grade heat is in crucial need. As an avenue for thermal energy recovery, thermogalvanic cell has gained attention.[65–67] Thermogalvanic cell is a type of galvanic cell that uses temperature gradient between cathode and anode to generate electrical energy.[67,68] Different temperatures cause distinct chemical equilibrium states and redox entropies at each electrode. As the system tries to equilibrate by transporting entropy, this effort gets translated to cell potential, which results in a current flow in a complete circuit.[66,69,70]

The Seebeck coefficient (S_e), a key metric to measure the performance of a thermogalvanic cell, quantifies the induced thermogalvanic cell potential generated in a material due to a temperature gradient across it.[71] In an equation, this can be defined as:

$$S_e = \partial V/\partial T \tag{1.1}$$

Seebeck coefficient is closely related to entropy. The relationship can be explained by taking two equations for free energy change:

$$\Delta G = -nFE \tag{1.2}$$

$$\Delta G = \Delta H - T\Delta S \tag{1.3}$$

By combining the two equations 1.1 and 1.2, this equation is achieved:

$$S_e = -\frac{1}{nF}\left(\frac{\partial(\Delta G)}{\partial T}\right) \tag{1.4}$$

Assuming $\Delta H = 0$, the following equation[72] can be achieved by combining equations 1.3 and 1.4:

$$S_e = \partial V/\partial T = \Delta S/nF \tag{1.5}$$

To achieve high S_e in a thermogalvanic cell, efforts have been made to develop systems with high redox entropies, especially by controlling the solvation entropy through inducing

supramolecular host-guest interactions,[73,74] exploring different solvent systems,[75–78] and employing electrolytes with redox-dependent phase changes.[79]

1.4.2 Thermogalvanic cell with POM electrolytes examples

Polyoxometalates have recently gained interest as electrolytes in thermogalvanic cell. Wang *et al.* has created a near-IR (NIR) photo-thermogalvanic cell which utilizes photothermal effect from solar radiation to generate thermogalvanic conversion.[80] Polyoxovanadate compound ({[Ni-(1,10-phenanthrolilne)$_3$][$V_{13}O_{34}$Cl]Cl}) was used as electrolyte in ionic liquid, as this redox-active species absorbs solar radiation and act as photo-thermo-electric (PTE) conversion component. The polyoxovanadate-ionic liquid system was able to achieve a large S_e of 6.38 mV/K and an optimized thermal power of 1.2 W/m^2 at a temperature difference of 70 K, with a NIR-photothermal efficiency of 16.04 and 23% at 808 and 1064 nm, respectively, making it a potential candidate for low-grade solar heat energy utilization.

Svensson Grape *et al.* focused on the direct relationship between reversible redox entropy change (ΔS_{rc}) and S_e, and linear correlation between ΔS_{rc} and the difference of squared charges of the oxidized and reduced species ($Z_{ox}^2 - Z_{red}^2$), when solvation radius *r* remain consistent throughout redox events.[81,82] Wells–Dawson cluster ($[P_2W_{18}O_{62}]^{6-}$) was used as thermogalvanic electrolyte due to its highly charged redox pair ($[P_2W_{18}O_{62}]^{6-/7-}$), while having only 1.5% of solvation shell volume difference between two species. The temperature dependency of the cluster's redox was studied by varied-temperature cyclic voltammetry and the aqueous thermogalvanic flow cell with $[P_2W_{18}O_{62}]^{6-}$ in 0.1 M sodium acetate buffer (pH = 5.5) resulted in a S_e of −1.7 mV/K at 10 K temperature difference, a value comparable to that of the state-of-the-art electrolyte $Fe(CN)_6^{4-/3-}$ in solution-phase system. These studies demonstrate promising

applications of polyoxometalate electrolytes in harvesting low-grade waste heat and converting it to electrical energy.

REFERENCES

(1) Pope, M. T. *Heteropoly and Isopoly Oxometalates*; Jørgensen, C. K., Lappert, M. F., Lippard, S. J., Margrave, J. L., Niedenzu, K., Nöth, H., Parry, R. W., Yamatera, H., Series Eds.; Inorganic Chemistry Concepts; Springer Berlin Heidelberg: Berlin, Heidelberg, 1983; Vol. 8. https://doi.org/10.1007/978-3-662-12004-0.

(2) Miras, H. N.; Vilà-Nadal, L.; Cronin, L. Polyoxometalate Based Open-Frameworks (POM-OFs). *Chem. Soc. Rev.* **2014**, *43* (16), 5679–5699. https://doi.org/10.1039/C4CS00097H.

(3) Keggin, J. F. The Structure and Formula of 12-Phosphotungstic Acid. *Proceedings of the Royal Society of London. Series A, Containing Papers of a Mathematical and Physical Character* **1934**, *144* (851), 75–100. https://doi.org/10.1098/rspa.1934.0035.

(4) Dawson, B. The Structure of the 9(18)-Heteropoly Anion in Potassium 9(18)-Tungstophosphate, K6(P2W18O62).14H2O. *Acta Cryst* **1953**, *6* (2), 113–126. https://doi.org/10.1107/S0365110X53000466.

(5) Alizadeh, M. H.; Harmalker, S. P.; Jeannin, Y.; Martin-Frere, J.; Pope, M. T. A Heteropolyanion with Fivefold Molecular Symmetry That Contains a Nonlabile Encapsulated Sodium Ion. The Structure and Chemistry of [NaP5W30O110]14-. *J. Am. Chem. Soc.* **1985**, *107* (9), 2662–2669. https://doi.org/10.1021/ja00295a019.

(6) Vilà-Nadal, L.; Mitchell, S. G.; Rodríguez-Fortea, A.; Miras, H. N.; Cronin, L.; Poblet, J. M. Connecting Theory with Experiment to Understand the Initial Nucleation Steps of Heteropolyoxometalate Clusters. *Phys. Chem. Chem. Phys.* **2011**, *13* (45), 20136–20145. https://doi.org/10.1039/C1CP21209E.

(7) Coucouvanis, D. *Inorganic Syntheses Vol. 33*; 2002.

(8) Ginsberg, A. P. *Inorganic Syntheses Vol. 27*; 1990.

(9) Gabb, D.; Pradeep, C. P.; Boyd, T.; Mitchell, S. G.; Miras, H. N.; Long, D.-L.; Cronin, L. A General Route for the Transfer of Large, Highly-Charged Polyoxometalates from Aqueous to Organic Phase. *Polyhedron* **2013**, *52*, 159–164. https://doi.org/10.1016/j.poly.2012.10.015.

(10) Takahashi, K.; Sano, T.; Sadakane, M. Preparation and Characterization of Preyssler-Type Phosphotungstic Acid, H15–n[P5W30O110Mn+], with Different Encapsulated Cations (M = Na, Ca, Bi, Eu, Y, or Ce), and Their Thermal Stability and Acid Catalyst Properties. *Zeitschrift*

für anorganische und allgemeine Chemie **2014**, *640* (7), 1314–1321. https://doi.org/10.1002/zaac.201400038.

(11) Gumerova, N. I.; Rompel, A. Synthesis, Structures and Applications of Electron-Rich Polyoxometalates. *Nature Reviews Chemistry* **2018**, *2* (2), 1–20. https://doi.org/10.1038/s41570-018-0112.

(12) Pope, M. T.; Varga, G. M. Jr. Heteropoly Blues. I. Reduction Stoichiometries and Reduction Potentials of Some 12-Tungstates. *Inorg. Chem.* **1966**, *5* (7), 1249–1254. https://doi.org/10.1021/ic50041a038.

(13) Pope, M. T.; Papaconstantinou, E. Heteropoly Blues. II. Reduction of 2:18-Tungstates. *Inorg. Chem.* **1967**, *6* (6), 1147–1152. https://doi.org/10.1021/ic50052a018.

(14) Creaser, I.; Heckel, M. C.; Neitz, R. J.; Pope, M. T. Rigid Nonlabile Polyoxometalate Cryptates [ZP5W30O110](15-n)- That Exhibit Unprecedented Selectivity for Certain Lanthanide and Other Multivalent Cations. *Inorg. Chem.* **1993**, *32* (9), 1573–1578. https://doi.org/10.1021/ic00061a010.

(15) Pope, M. T. Heteropoly and Isopoly Anions as Oxo Complexes and Their Reducibility to Mixed-Valence Blues. *Inorg. Chem.* **1972**, *11* (8), 1973–1974. https://doi.org/10.1021/ic50114a057.

(16) Li, Q.; Zhang, L.; Dai, J.; Tang, H.; Li, Q.; Xue, H.; Pang, H. Polyoxometalate-Based Materials for Advanced Electrochemical Energy Conversion and Storage. *Chemical Engineering Journal* **2018**, *351*, 441–461. https://doi.org/10.1016/j.cej.2018.06.074.

(17) Zhang, Y.; Liu, J.; Li, S.-L.; Su, Z.-M.; Lan, Y.-Q. Polyoxometalate-Based Materials for Sustainable and Clean Energy Conversion and Storage. *EnergyChem* **2019**, *1* (3), 100021. https://doi.org/10.1016/j.enchem.2019.100021.

(18) Monakhov, K. Y.; Moors, M.; Kögerler, P. Chapter Nine - Perspectives for Polyoxometalates in Single-Molecule Electronics and Spintronics. In *Advances in Inorganic Chemistry*; van Eldik, R., Cronin, L., Eds.; Polyoxometalate Chemistry; Academic Press, 2017; Vol. 69, pp 251–286. https://doi.org/10.1016/bs.adioch.2016.12.009.

(19) Wu, C.; Qiao, X.; Robertson, C. M.; Higgins, S. J.; Cai, C.; Nichols, R. J.; Vezzoli, A. A Chemically Soldered Polyoxometalate Single-Molecule Transistor. *Angewandte Chemie* **2020**, *132* (29), 12127–12132. https://doi.org/10.1002/ange.202002174.

(20) Busche, C.; Vilà-Nadal, L.; Yan, J.; Miras, H. N.; Long, D.-L.; Georgiev, V. P.; Asenov, A.; Pedersen, R. H.; Gadegaard, N.; Mirza, M. M.; Paul, D. J.; Poblet, J. M.; Cronin, L. Design and Fabrication of Memory Devices Based on Nanoscale Polyoxometalate Clusters. *Nature* **2014**, *515* (7528), 545–549. https://doi.org/10.1038/nature13951.

(21) Vilà-Nadal, L.; Mitchell, S. G.; Markov, S.; Busche, C.; Georgiev, V.; Asenov, A.; Cronin, L. Towards Polyoxometalate-Cluster-Based Nano-Electronics. *Chemistry – A European Journal* **2013**, *19* (49), 16502–16511. https://doi.org/10.1002/chem.201301631.

(22) Wang, S.-S.; Yang, G.-Y. Recent Advances in Polyoxometalate-Catalyzed Reactions. *Chem. Rev.* **2015**, *115* (11), 4893–4962. https://doi.org/10.1021/cr500390v.

(23) Liu, S.-M.; Zhang, Z.; Li, X.; Jia, H.; Ren, M.; Liu, S. Ti-Substituted Keggin-Type Polyoxotungstate as Proton and Electron Reservoir Encaged into Metal–Organic Framework for Carbon Dioxide Photoreduction. *Advanced Materials Interfaces* **2018**, *5* (21), 1801062. https://doi.org/10.1002/admi.201801062.

(24) Keita, B.; Nadjo, L. Polyoxometalate-Based Homogeneous Catalysis of Electrode Reactions: Recent Achievements. *Journal of Molecular Catalysis A: Chemical* **2007**, *262* (1), 190–215. https://doi.org/10.1016/j.molcata.2006.08.066.

(25) Lv, H.; V. Geletii, Y.; Zhao, C.; W. Vickers, J.; Zhu, G.; Luo, Z.; Song, J.; Lian, T.; G. Musaev, D.; L. Hill, C. Polyoxometalate Water Oxidation Catalysts and the Production of Green Fuel. *Chemical Society Reviews* **2012**, *41* (22), 7572–7589. https://doi.org/10.1039/C2CS35292C.

(26) Whitesides, G. M.; Mathias, J. P.; Seto, C. T. Molecular Self-Assembly and Nanochemistry: A Chemical Strategy for the Synthesis of Nanostructures. *Science* **1991**, *254* (5036), 1312–1319. https://doi.org/10.1126/science.1962191.

(27) Coronado, E.; Gómez-García, C. J. Polyoxometalate-Based Molecular Materials. *Chem. Rev.* **1998**, *98* (1), 273–296. https://doi.org/10.1021/cr970471c.

(28) Vilà-Nadal, L.; Cronin, L. Design and Synthesis of Polyoxometalate-Framework Materials from Cluster Precursors. *Nat Rev Mater* **2017**, *2* (10), 17054. https://doi.org/10.1038/natrevmats.2017.54.

(29) Liu, Q.; Wang, X. Polyoxometalate Clusters: Sub-Nanometer Building Blocks for Construction of Advanced Materials. *Matter* **2020**, *2* (4), 816–841. https://doi.org/10.1016/j.matt.2020.01.020.

(30) Liu, J.-X.; Zhang, X.-B.; Li, Y.-L.; Huang, S.-L.; Yang, G.-Y. Polyoxometalate Functionalized Architectures. *Coordination Chemistry Reviews* **2020**, *414*, 213260. https://doi.org/10.1016/j.ccr.2020.213260.

(31) Gómez-Romero, P.; Casañ-Pastor, N. Photoredox Chemistry in Oxide Clusters. Photochromic and Redox Properties of Polyoxometalates in Connection with Analog Solid State Colloidal Systems. *J. Phys. Chem.* **1996**, *100* (30), 12448–12454. https://doi.org/10.1021/jp953326g.

(32) Pope, M. T.; Müller, A. Polyoxometalate Chemistry: An Old Field with New Dimensions in Several Disciplines. *Angewandte Chemie International Edition in English* **1991**, *30* (1), 34–48. https://doi.org/10.1002/anie.199100341.

(33) Hill, C. L.; Prosser-McCartha, C. M. Homogeneous Catalysis by Transition Metal Oxygen Anion Clusters. *Coordination Chemistry Reviews* **1995**, *143*, 407–455. https://doi.org/10.1016/0010-8545(95)01141-B.

(34) Hill, C. L. Progress and Challenges in Polyoxometalate-Based Catalysis and Catalytic Materials Chemistry. *Journal of Molecular Catalysis A: Chemical* **2007**, *262* (1), 2–6. https://doi.org/10.1016/j.molcata.2006.08.042.

(35) Li, N.; Liu, J.; Dong, B.-X.; Lan, Y.-Q. Polyoxometalate-Based Compounds for Photo- and Electrocatalytic Applications. *Angewandte Chemie International Edition* **2020**, *59* (47), 20779–20793. https://doi.org/10.1002/anie.202008054.

(36) Coronado, E.; Giménez-Saiz, C.; Gómez-García, C. J. Recent Advances in Polyoxometalate-Containing Molecular Conductors. *Coordination Chemistry Reviews* **2005**, *249* (17), 1776–1796. https://doi.org/10.1016/j.ccr.2005.02.017.

(37) Chen, X.; Zhou, Y.; Roy, V. A. L.; Han, S.-T. Evolutionary Metal Oxide Clusters for Novel Applications: Toward High-Density Data Storage in Nonvolatile Memories. *Advanced Materials* **2018**, *30* (3), 1703950. https://doi.org/10.1002/adma.201703950.

(38) Clemente-Juan, J. M.; Coronado, E. Magnetic Clusters from Polyoxometalate Complexes. *Coordination Chemistry Reviews* **1999**, *193–195*, 361–394. https://doi.org/10.1016/S0010-8545(99)00170-8.

(39) Ritchie, C.; Ferguson, A.; Nojiri, H.; Miras, H. N.; Song, Y.-F.; Long, D.-L.; Burkholder, E.; Murrie, M.; Kögerler, P.; Brechin, E. K.; Cronin, L. Polyoxometalate-Mediated Self-Assembly of Single-Molecule Magnets: [XW9O34]2[MnIII4MnII2O4(H2O)4]12−. *Angewandte Chemie* **2008**, *120* (30), 5691–5694. https://doi.org/10.1002/ange.200801281.

(40) Compain, J.-D.; Mialane, P.; Dolbecq, A.; Mbomekallé, I. M.; Marrot, J.; Sécheresse, F.; Rivière, E.; Rogez, G.; Wernsdorfer, W. Iron Polyoxometalate Single-Molecule Magnets. *Angewandte Chemie International Edition* **2009**, *48* (17), 3077–3081. https://doi.org/10.1002/anie.200900117.

(41) Ibrahim, M.; Lan, Y.; Bassil, B. S.; Xiang, Y.; Suchopar, A.; Powell, A. K.; Kortz, U. Hexadecacobalt(II)-Containing Polyoxometalate-Based Single-Molecule Magnet. *Angewandte Chemie International Edition* **2011**, *50* (20), 4708–4711. https://doi.org/10.1002/anie.201100280.

(42) Rhule, J. T.; Hill, C. L.; Judd, D. A.; Schinazi, R. F. Polyoxometalates in Medicine. *Chem. Rev.* **1998**, *98* (1), 327–358. https://doi.org/10.1021/cr960396q.

(43) Hasenknopf, B. Polyoxometalates: Introduction to a Class of Inorganic Compounds and Their Biomedical Applications. *Front Biosci* **2005**, *10* (1–3), 275. https://doi.org/10.2741/1527.

(44) Čolović, M. B.; Lacković, M.; Lalatović, J.; Mougharbel, A. S.; Kortz, U.; Krstić, D. Z. Polyoxometalates in Biomedicine: Update and Overview. *Current Medicinal Chemistry 27* (3), 362–379.

(45) Kitagawa, S.; Kitaura, R.; Noro, S. Functional Porous Coordination Polymers. *Angewandte Chemie International Edition* **2004**, *43* (18), 2334–2375. https://doi.org/10.1002/anie.200300610.

(46) Givaja, G.; Amo-Ochoa, P.; J. Gómez-García, C.; Zamora, F. Electrical Conductive Coordination Polymers. *Chemical Society Reviews* **2012**, *41* (1), 115–147. https://doi.org/10.1039/C1CS15092H.

(47) Khan, M. I.; Yohannes, E.; Doedens, R. J. [M3V18O42(H2O)12(XO4)]·24 H2O (M=Fe, Co; X=V, S): Metal Oxide Based Framework Materials Composed of Polyoxovanadate Clusters. *Angewandte Chemie International Edition* **1999**, *38* (9), 1292–1294. https://doi.org/10.1002/(SICI)1521-3773(19990503)38:9<1292::AID-ANIE1292>3.0.CO;2-2.

(48) Ritchie, C.; Streb, C.; Thiel, J.; Mitchell, S. G.; Miras, H. N.; Long, D.-L.; Boyd, T.; Peacock, R. D.; McGlone, T.; Cronin, L. Reversible Redox Reactions in an Extended Polyoxometalate Framework Solid. *Angewandte Chemie International Edition* **2008**, *47* (36), 6881–6884. https://doi.org/10.1002/anie.200802594.

(49) Mitchell, S. G.; Streb, C.; Miras, H. N.; Boyd, T.; Long, D.-L.; Cronin, L. Face-Directed Self-Assembly of an Electronically Active Archimedean Polyoxometalate Architecture. *Nature Chem* **2010**, *2* (4), 308–312. https://doi.org/10.1038/nchem.581.

(50) Boyd, T.; Mitchell, S. G.; Gabb, D.; Long, D.-L.; Song, Y.-F.; Cronin, L. POMzites: A Family of Zeolitic Polyoxometalate Frameworks from a Minimal Building Block Library. *J. Am. Chem. Soc.* **2017**, *139* (16), 5930–5938. https://doi.org/10.1021/jacs.7b01807.

(51) Zhan, C.; Cameron, J. M.; Gabb, D.; Boyd, T.; Winter, R. S.; Vilà-Nadal, L.; Mitchell, S. G.; Glatzel, S.; Breternitz, J.; Gregory, D. H.; Long, D.-L.; Macdonell, A.; Cronin, L. A Metamorphic Inorganic Framework That Can Be Switched between Eight Single-Crystalline States. *Nat Commun* **2017**, *8* (1), 14185. https://doi.org/10.1038/ncomms14185.

(52) von Allmen, K. D.; Grundmann, H.; Linden, A.; Patzke, G. R. Synthesis and Characterization of 0D–3D Copper-Containing Tungstobismuthates Obtained from the Lacunary Precursor Na9[B-α-BiW9O33]. *Inorg. Chem.* **2017**, *56* (1), 327–335. https://doi.org/10.1021/acs.inorgchem.6b02217.

(53) Turo, M. J.; Chen, L.; Moore, C. E.; Schimpf, A. M. Co2+-Linked [NaP5W30O110]14−: A Redox-Active Metal Oxide Framework with High Electron Density. *J. Am. Chem. Soc.* **2019**, 5.

(54) Chen, L.; San, K. A.; Turo, M. J.; Gembicky, M.; Fereidouni, S.; Kalaj, M.; Schimpf, A. M. Tunable Metal Oxide Frameworks via Coordination Assembly of Preyssler-Type Molecular Clusters. *J. Am. Chem. Soc.* **2019**, *141* (51), 20261–20268. https://doi.org/10.1021/jacs.9b10277.

(55) Sperry, J. B.; Wright, D. L. The Application of Cathodic Reductions and Anodic Oxidations in the Synthesis of Complex Molecules. *Chem. Soc. Rev.* **2006**, *35* (7), 605–621. https://doi.org/10.1039/B512308A.

(56) Degner, D. Organic Electrosyntheses in Industry. In *Electrochemistry III*; Stekchan, E., Ed.; Springer: Berlin, Heidelberg, 1988; pp 1–95. https://doi.org/10.1007/3-540-19180-1_5.

(57) Yan, M.; Kawamata, Y.; Baran, P. S. Synthetic Organic Electrochemistry: Calling All Engineers. *Angewandte Chemie International Edition* **2018**, *57* (16), 4149–4155. https://doi.org/10.1002/anie.201707584.

(58) Utley, J. Trends in Organic Electrosynthesis. *Chem. Soc. Rev.* **1997**, *26* (3), 157–167. https://doi.org/10.1039/CS9972600157.

(59) Al-Kutubi, H.; Gascon, J.; Sudhölter, E. J. R.; Rassaei, L. Electrosynthesis of Metal–Organic Frameworks: Challenges and Opportunities. *ChemElectroChem* **2015**, *2* (4), 462–474. https://doi.org/10.1002/celc.201402429.

(60) Batail, P.; Boubekeur, K.; Fourmigué, M.; Gabriel, J.-C. P. Electrocrystallization, an Invaluable Tool for the Construction of Ordered, Electroactive Molecular Solids. *Chem. Mater.* **1998**, *10* (10), 3005–3015. https://doi.org/10.1021/cm980538s.

(61) Bellitto, C.; Bonamico, M.; Fares, V.; Federici, F.; Righini, G.; Kurmoo, M.; Day, P. BEDT-TTF Salts with .Alpha.-Keggin Poly(Oxometallates): Electrical, Magnetic, and Optical Properties of (BEDT-TTF)8[PMo12O40] and (BEDT-TTF)8[SiW12O40] and X-Ray Crystal Structure of (BEDT-TTF)8[PMo12O40].Cntdot.{(CH3CN.Cntdot.H2O)2}. *Chem. Mater.* **1995**, *7* (8), 1475–1484. https://doi.org/10.1021/cm00056a012.

(62) Champsaur, A. M.; Mézière, C.; Allain, M.; Paley, D. W.; Steigerwald, M. L.; Nuckolls, C.; Batail, P. Weaving Nanoscale Cloth through Electrostatic Templating. *J. Am. Chem. Soc.* **2017**, *139* (34), 11718–11721. https://doi.org/10.1021/jacs.7b07279.

(63) Zhang, Q.; Ondus, J.; Mills, J.; Bahadori, A.; Smith, J.; Jordan, T.; Xu, H.; Hwu, S.-J. Bench-Top Electrochemical Crystal Growth of POMOFs: In-Situ Synthesis of New Organic-Inorganic Hybrids Containing [V10O28](6+n)− Polyoxovanadate. *Journal of Solid State Chemistry* **2020**, *287*, 121368. https://doi.org/10.1016/j.jssc.2020.121368.

(64) Zhang, Q.; Ondus, J.; Sheriff, K.; Mills, J.; Bahadori, A.; Smith, J.; Hwu, S.-J. Electrochemical Synthesis of Decavanadates-Containing Inorganic Complex and Inorganic-Organic Hybrid in Aqueous Solutions. *Polyhedron* **2021**, *209*, 115459. https://doi.org/10.1016/j.poly.2021.115459.

(65) Hur, S.; Kim, S.; Kim, H.-S.; Kumar, A.; Kwon, C.; Shin, J.; Kang, H.; Sung, T. H.; Ryu, J.; Baik, J. M.; Song, H.-C. Low-Grade Waste Heat Recovery Scenarios: Pyroelectric, Thermomagnetic, and Thermogalvanic Thermal Energy Harvesting. *Nano Energy* **2023**, *114*, 108596. https://doi.org/10.1016/j.nanoen.2023.108596.

(66) ZITO, R. THERMOGALVANIC ENERGY CONVERSION. *AIAA Journal* **1963**, *1* (9), 2133–2138. https://doi.org/10.2514/3.2006.

(67) Quickenden, T. I.; Vernon, C. F. Thermogalvanic Conversion of Heat to Electricity. *Solar Energy* **1986**, *36* (1), 63–72. https://doi.org/10.1016/0038-092X(86)90061-7.

(68) Chum, H.; Osteryoung, R.; Facility, S. E. R. Review of Thermally Regenerative Electrochemical Systems, Volume 1: Synopsis and Executive Summary.

(69) Agar, JN. Thermogalvanic Cell; Delahay, P.; Tobias, C. W. *Advances in Electrochemistry and Electrochemical Engineering. Volume 3*; Wiley & Sons, 1961, 31–121.

(70) deBethune, A. J.; Licht, T. S.; Swendeman, N. The Temperature Coefficients of Electrode Potentials: The Isothermal and Thermal Coefficients—The Standard Ionic Entropy of Electrochemical Transport of the Hydrogen Ion. *J. Electrochem. Soc.* **1959**, *106* (7), 616. https://doi.org/10.1149/1.2427448.

(71) Blundell, S.; Blundell, K. M. *Concepts in Thermal Physics*; Oxford University Press, 2010.

(72) Lee, S. W.; Yang, Y.; Lee, H.-W.; Ghasemi, H.; Kraemer, D.; Chen, G.; Cui, Y. An Electrochemical System for Efficiently Harvesting Low-Grade Heat Energy. *Nat Commun* **2014**, *5* (1), 3942. https://doi.org/10.1038/ncomms4942.

(73) Zhou, H.; Yamada, T.; Kimizuka, N. Supramolecular Thermo-Electrochemical Cells: Enhanced Thermoelectric Performance by Host-Guest Complexation and Salt-Induced Crystallization. *J Am Chem Soc* **2016**, *138* (33), 10502–10507. https://doi.org/10.1021/jacs.6b04923.

(74) Xia, K. T.; Rajan, A.; Surendranath, Y.; Bergman, R. G.; Raymond, K. N.; Toste, F. D. Tunable Electrochemical Entropy through Solvent Ordering by a Supramolecular Host. *J. Am. Chem. Soc.* **2023**, *145* (46), 25463–25470. https://doi.org/10.1021/jacs.3c10145.

(75) Inoue, H.; Zhou, H.; Ando, H.; Nakagawa, S.; Yamada, T. Exploring the Local Solvation Structure of Redox Molecules in a Mixed Solvent for Increasing the Seebeck Coefficient of Thermocells. *Chem. Sci.* **2024**, *15* (1), 146–153. https://doi.org/10.1039/D3SC04955H.

(76) Liu, Y.; Zhang, Q.; Odunmbaku, G. O.; He, Y.; Zheng, Y.; Chen, S.; Zhou, Y.; Li, J.; Li, M.; Sun, K. Solvent Effect on the Seebeck Coefficient of Fe2+/Fe3+ Hydrogel Thermogalvanic Cells. *J. Mater. Chem. A* **2022**, *10* (37), 19690–19698. https://doi.org/10.1039/D1TA10508F.

(77) Laws, K.; Buckingham, M. A.; Farleigh, M.; Ma, M.; Aldous, L. High Seebeck Coefficient Thermogalvanic Cells via the Solvent-Sensitive Charge Additivity of Cobalt 1,8-Diaminosarcophagine. *Chem. Commun.* **2023**, *59* (16), 2323–2326. https://doi.org/10.1039/D2CC05413B.

(78) Taheri, A.; MacFarlane, D. R.; Pozo-Gonzalo, C.; Pringle, J. M. The Effect of Solvent on the Seebeck Coefficient and Thermocell Performance of Cobalt Bipyridyl and Iron Ferri/Ferrocyanide Redox Couples. *Aust. J. Chem.* **2019**, *72* (9), 709–716. https://doi.org/10.1071/CH19245.

(79) Zhou, H.; Matoba, F.; Matsuno, R.; Wakayama, Y.; Yamada, T. Direct Conversion of Phase-Transition Entropy into Electrochemical Thermopower and the Peltier Effect. *Advanced Materials* **2023**, *35* (36), 2303341. https://doi.org/10.1002/adma.202303341.

(80) Wang, Y.; Liu, C.; Wang, Y.; Zhu, C.; Chen, X.; Liu, B. Efficient Photo-Thermo-Electric Conversion Using Polyoxovanadate in Ionic Liquid for Low-Grade Heat Utilization. *ChemSusChem* **2021**, *14* (24), 5434–5441. https://doi.org/10.1002/cssc.202101532.

(81) Sahami, S.; Weaver, M. J. Entropic and Enthalpic Contributions to the Solvent Dependence of the Thermodynamics of Transition-Metal Redox Couples: Part II. Couples Containing Ammine and Ethylenediamine Ligands. *Journal of Electroanalytical Chemistry and Interfacial Electrochemistry* **1981**, *122*, 171–181. https://doi.org/10.1016/S0022-0728(81)80148-9.

(82) Svensson Grape, E.; Huang, J.; Roychowdhury, D.; Debela, T. T.; Chang, H.; Jenkins, A.; Schimpf, A. M.; Hendon, C. H.; Brozek, C. K. Converting Heat to Electrical Energy Using Highly Charged Polyoxometalate Electrolytes. *ACS Appl. Energy Mater.* **2024**. https://doi.org/10.1021/acsaem.4c00036.

Chapter 2 General Methods

2.1 General synthesis

2.1.1 Synthesis of the Preyssler cluster

Preyssler anions were synthesized following the preparation methods reported by Hayashi et al.[1] with minor adaptations,[2] using hydrothermal methods. Specifically, to a 200 ml Teflon-lined acid-digestion vessel, $Na_2WO_4 \bullet 2H_2O$ (29.7 g, 90.0 mmol) and NaCl (3.51 g, 60.0 mmol) were added, along with 27.0 ml of DI water and 21.0 ml of 85 % H_3PO_4. After the stirring the reaction mixture for 5 minutes, the sealed vessel was placed in an oven at 125 ℃ for 20 hours. Upon cooling to room temperature, KCl (9.00 g, 0.120 mol) was added to the reaction mixture, which was then stirred for 30 minutes. The pale-yellow precipitate was collected by vacuum filtration and redissolved in 30.0 ml of hot DI water. The solution was slowly cooled to room temperature, resulting in pale-yellow to colorless crystals. A couple of additional recrystallizations were performed to achieve pure Preyssler compound without Wells–Dawson impurities. ^{31}P NMR analysis was carried out to determine the purity of the product.

2.1.2 Synthesis of the α-Wells–Dawson cluster

Although Wells–Dawson clusters are the major byproduct of Preyssler cluster synthesis, note that recrystallizing the mother liquor of Preyssler crystals is not recommended to acquire pure α-Wells–Dawson anions in large quantities. There are many synthetic protocols reported for Wells–Dawson, however, the optimized synthesis of this compound is still in discussion.[3] After trying several different methods, synthesis of Wells–Dawson anions was ultimately carried out following the synthetic protocol by Nadjo et al. with few modifications, as the procedure allows only marginal amount of Preyssler impurities to form.[3,4] To a 300 ml aqueous solution of $Na_2WO_4 \bullet 2H_2O$ (150 g, 0.46 mol), 4 M HCl (125 ml, 0.50 mol) was added dropwise under vigorous stirring. The solution turned cloudy upon the addition of HCl, however, it eventually

turned clear with stirring. 4 M H_3PO_4 (125 ml, 0.50 mol) was then slowly added to the solution, resulting in a pale-yellow color. Keeping the specific amount of HCl and H_3PO_4 added was crucial to deter the formation of Preyssler anions. The resulting solution was refluxed for 24 hours and then cooled to room temperature. Upon cooling, KCl (75 g, 1.01 mol) was added to the solution to induce precipitation. The precipitate was collected by vacuum filtration and dissolved back into 325 ml DI water. After filtering through fine glass frit to remove any insoluble impurities, the solution was heated at 80 °C for 72 hours, resulting in a reduction in volume to 50 ml. The above synthesis can be halved. NMR analysis of the aliquots collected every 24 hours of reaction showed that the ratio of α-isomer to β-isomer increased throughout heating. Slow cooling of the solution to 4 °C allowed yellow crystals to form and be collected. An additional recrystallization in hot DI water resulted in the removal of β-isomer impurities.

2.1.3 Cation-exchange to protons on the Preyssler cluster

Acid Preyssler was synthesized following a previously reported preparation.[5] Preyssler prepared following the aforementioned procedures results in the potassium salt of Preyssler anions. To exchange the potassium cations for protons, a 100 ml ion-exchange column was prepared by packing about 50.0 g of Dowex resin (50–100 mesh) beads rehydrated in 3 M HCl overnight. A total of 500 ml 3 M HCl was flushed through the prepared column to saturate the beads with proton. Then, a total of 200–300 ml of DI water was flushed through the column to get rid of excess HCl. It should be noted that the pH of each 100 ml rinse should be checked, and second rinse is expected to be close to pH 5–7. Once the column was prepared, 10.0 g of the potassium salt of Preyssler was dissolved in 100.0 ml of DI water. This solution was passed through the column and collected. 90 ml of DI water was flushed through the in three rinses and collected with the initial solution, totaling about 200 ml. The collected solution was then heated at 40–60 °C to evaporate the water, however, this should be monitored regularly to ensure that

the compound is not heated in solid phase, to prevent decomposition. The resulting compound is light yellow.

2.2 General electrochemical cell setup for electrocrystallization

A two-electrode setup was used to synthesize Preyssler-based metal oxide networks. Both undivided and divided cells were used. Briefly, in an undivided cell setup, an electrolytic solution of polyoxometalates and transition metal salts was prepared by dissolving the substrates in 10.0 ml of 0.05 M potassium acetate buffer (pH = 5.6) in a 20 ml scintillation vial. For the divided cell setup, a custom H-cell with a fine frit was used as the vessel. The anodic compartment was charged with a 5 ml solution of metal salts dissolved in 0.05 M of KOAc (pH = 5.6). The cathodic compartment was charged with a 5 ml solution of metal salts and polyoxometalates dissolved in 0.05 M of KOAc (pH = 5.6). Exact quantities of metal salts and quantities will be mentioned in Chapter 3.

A platinum wire of 0.5 mm diameter was used as the cathode. Either a sacrificial anode of transition metal or platinum wire was used as the anode. Both anode and cathode were dipped into the solution to a depth of ~1.5 cm (ca. 0.24 cm^2). A current of 50 μA was applied for 20 hours.

2.3 Variable-temperature cyclic voltammetry

A three-electrode set up with a thermometer was used for cyclic voltammetry. A glassy carbon electrode (GCE), a saturated calomel electrode (SCE), and a platinum wire were used as the working, reference, and counter electrodes, respectively. In a ~ 20 ml vessel, an aqueous solution of polyoxometalates with specific electrolyte was prepared and a stir bar was added. The solution was sparged with a stream of nitrogen or argon gas before the measurement. The solution was cooled to 2 °C in an ice bath, then heated to 10 °C, 20 °C, 30 °C, 40 °C, and 50 °C using a hot plate and a temperature probe (**Figure 2.1**).

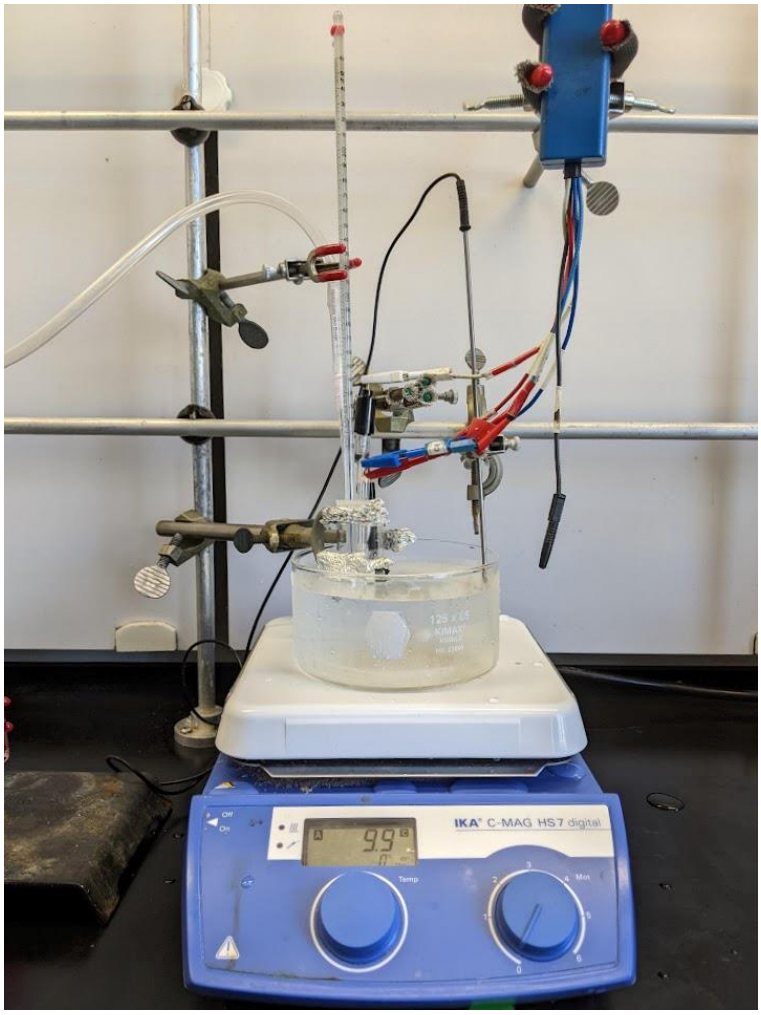


Figure 2.1. An example of electrochemical cell set up for temperature-dependent cyclic voltammetry.

REFERENCES

(1) Hayashi, A.; Haioka, T.; Takahashi, K.; Bassil, B. S.; Kortz, U.; Sano, T.; Sadakane, M. Cation Effect on Formation of Preyssler-Type 30-Tungsto-5-Phosphate: Enhanced Yield of Na-Encapsulated Derivative and Direct Synthesis of Ca- and Bi-Encapsulated Derivatives. *Zeitschrift für anorganische und allgemeine Chemie* **2015**, *641* (15), 2670–2676. https://doi.org/10.1002/zaac.201500679.

(2) Turo, M. J.; Chen, L.; Moore, C. E.; Schimpf, A. M. Co2+-Linked [NaP5W30O110]14−: A Redox-Active Metal Oxide Framework with High Electron Density. *J. Am. Chem. Soc.* **2019**, 5.

(3) Graham, C. R.; Finke, R. G. The Classic Wells−Dawson Polyoxometalate, K6[α-P2W18O62]·14H2O. Answering an 88 Year-Old Question: What Is Its Preferred, Optimum Synthesis? *Inorg. Chem.* **2008**, *47* (9), 3679–3686. https://doi.org/10.1021/ic702295y.

(4) Mbomekalle, I.-M.; Lu, Y. W.; Keita, B.; Nadjo, L. Simple, High Yield and Reagent-Saving Synthesis of Pure α-K6P2W18O62·14H2O. *Inorganic Chemistry Communications* **2004**, *7* (1), 86–90. https://doi.org/10.1016/j.inoche.2003.10.011.

(5) Takahashi, K.; Sano, T.; Sadakane, M. Preparation and Characterization of Preyssler-Type Phosphotungstic Acid, H15–n[P5W30O110Mn+], with Different Encapsulated Cations (M = Na, Ca, Bi, Eu, Y, or Ce), and Their Thermal Stability and Acid Catalyst Properties. *Zeitschrift für anorganische und allgemeine Chemie* **2014**, *640* (7), 1314–1321. https://doi.org/10.1002/zaac.201400038.

Chapter 3 Electrocrystallization of Preyssler-Based Metal Oxide Coordination Networks

3.1 Introduction

Using modular building blocks for bottom-up assembly has been widely applied in the development of new coordination networks, as it offers opportunities to couple the properties of the building-block with porosity or other mechanical advantages that these networks can provide.[1–10] By judiciously choosing the building blocks, these combinations often result in synergistic or emergent properties in the coordination networks.[1,5,11–14]

Polyoxometalates (POMs) have gained interest as due to their structural diversity and modifiability, and rich redox features, making them ideal candidates for use in assembly of coordination networks.[8–12,15–19] For example, Preyssler anions ($[NaP_5W_{30}O_{110}]^{14-}$, denoted as $\{P_5W_{30}\}$) have been used to synthesize all-inorganic metal oxide frameworks, which were self-assembled through the coordination of the cluster terminal oxo to first-row transition-metal cations.[11,12] These frameworks can be readily and reversibly reduced, owing to the rich redox properties of the cluster, and have proven to promising alternative materials to statistically doped metal oxides. In such examples, however, redox features of $\{P_5W_{30}\}$ were often perceived as contributing to framework properties but were rarely highlighted as a synthetic handle.

Electrocrystallization, a synthetic technique that utilizes electrochemical redox reactions to trigger the formation of crystalline compounds.[20] $\{P_5W_{30}\}$ is highly electroactive, and these clusters have been observed to crystallize under electrochemical reduction.[21] Furthermore, nucleophilicity of the terminal oxygens in $\{P_5W_{30}\}$, coupled with the large negative charge distributed across the cluster surface, has been shown to contribute to the formation of metal oxide frameworks.[22,23] Electrochemical reduction of these clusters may enhance their nucleophilicity, thereby promoting the growth of metal oxide frameworks. Therefore,

electrocrystallization is a promising synthetic platform for the development of new $\{P_5W_{30}\}$-based frameworks.

Herein, we present a strategy for the electrochemical synthesis of new metal oxide coordination networks based on $\{P_5W_{30}\}$. These networks are composed of clusters bridged through metal–aquo complexes of cobalt, nickel, zinc, and yttrium ($[M(H_2O)_n]^{m+}$, (M = Co, Ni, Zn, Y)), and each species is denoted as M-$\{P_5W_{30}\}$. Specifically, the coordination networks synthesized include first-row transition-metal bridged Co-, Ni-, Zn-$\{P_5W_{30}\}$, and second-row transition-metal bridged Y-$\{P_5W_{30}\}$. To date, only handful of POM-based coordination networks have been synthesized electrochemically[24,25] and to the best of our knowledge, the structure sherein are the first examples of electrocrystallized $\{P_5W_{30}\}$-based coordination networks.

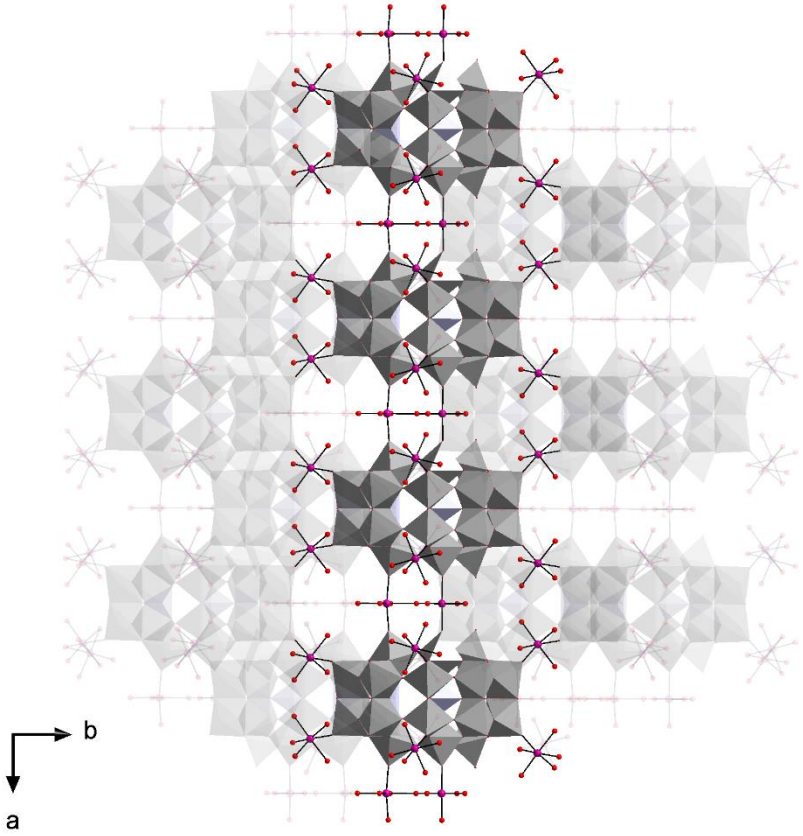


Figure 3.1. Crystal structure of Co-{P_5W_{30}} shown in (001) direction.

3.2 Results and Discussion

In the synthesis of Co-{P_5W_{30}}, a 10 ml solution of {P_5W_{30}} (65.0 mg, 7.88 μmol) and cobalt acetate tetrahydrate ($Co(OAc)_2$•$4H_2O$, 135.0 mg, 542.0 μmol) in 0.05 M potassium acetate buffer ($KOAc_{(aq)}$, pH = 5.6) was prepared. Upon dissolution, the final pH of the solution was measured as 6.1. The solution was then subjected to galvanostatic electrolysis of 50 μA in an undivided cell equipped with two platinum electrodes. In less than one minute, a dark blue deposition on the cathode was observed without a noticeable change in the color of the electrolytic solution, and black powder precipitated onto the anode. Products continued to form on the electrodes

throughout the whole duration of electrochemical reaction. Cathodic products were then collected as dark blue crystals after 20 hours of electrolysis.

X-ray diffraction analysis of a single crystal revealed a structure in the orthorhombic *Cmcm* space group (**Supplemental Table 3.1**, a = 14.0654(8) Å, b = 33.6984(19) Å, c = 30.2745(17) Å, α = 90°, β = 90°, γ = 90°). The structure features two modes of expansion resulting from different coordination environments at O_{cap} and O_{belt} of the cluster (**Figure 3.1**). At the cap region, $Co(H_2O)_4^{2+}$ units exclusively bridge clusters through Co–O_{cap} and a near-180° bond angle of O_{cap1}–Co–O_{cap2} enables the 1D elongation of the repeating chain units in the *a*-direction (**Figure 3.2**). Clusters in these chains are decorated with $Co(H_2O)_5^{2+}$ units at O_{belt}. Charge-balancing K^+ ions integrated in the crystal lattice enable the chains to pack close together through coordination by oxo and aquo ligands in the chains. This results in a polymeric expansion in the *bc* plane where a decorative $Co(H_2O)_5^{2+}$ unit shares three bridging aquo ligands with another decorative $Co(H_2O)_5^{2+}$ in proximity, resulting in a $Co_2(H_2O)_9$ motif that links chains to each other (**Figure 3.3**). The powder X-ray diffraction pattern of Co-$\{P_5W_{30}\}$ matches well with the powder pattern simulated from the single-crystal X-ray structure, indicating that the product is phase-pure (**Supplemental Figure 3.1**). Polyoxometalates have been used as anionic ligands in previously reported studies, with their nucleophilic surface oxygen coordinating the transition-metal cations.[11,12] This is the first time, however, that cap-to-cap connections are exclusively observed without any cap-to-belt connections. The yield of this synthesis was 40.3 % based on W.

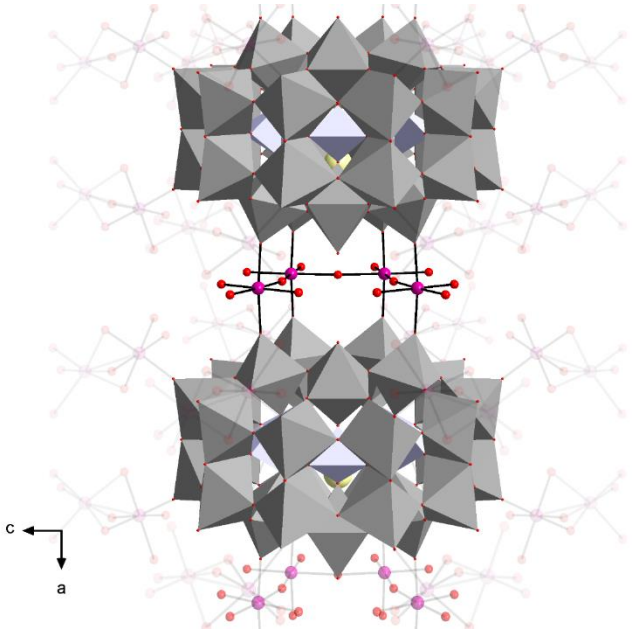


Figure 3.2. Representation of O_{cap1}–Co–O_{cap2} connections in Co-{P_5W_{30}}.

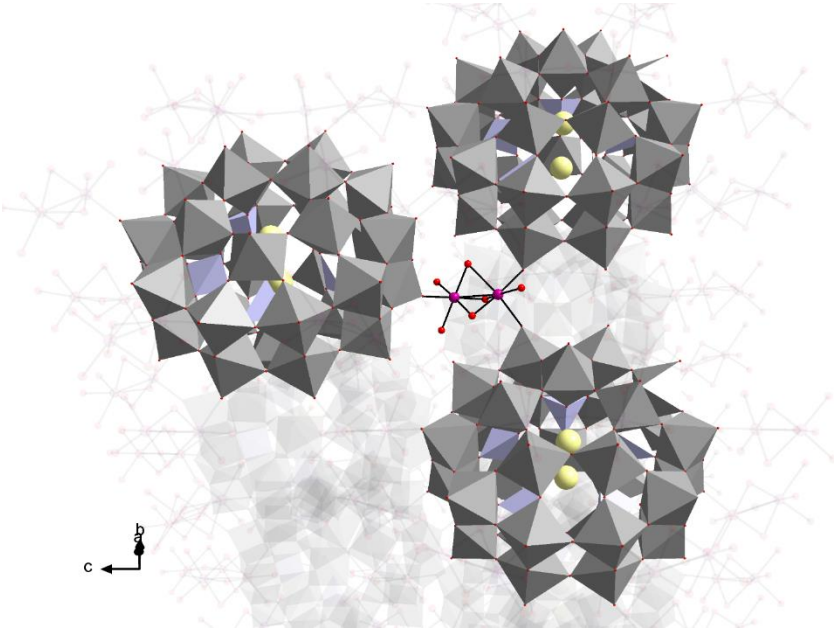


Figure 3.3. Representation of $Co_2(H_2O)_9$ motif resulting from O_{belt}–Co connections in Co-{P_5W_{30}}.

The dark blue color of Co-{P_5W_{30}} is characteristic of reduced polyoxometalates.[26–28] X-ray photoelectron spectroscopy data confirms the existence of W^{5+} in these samples, as well as Co^0

(**Supplemental Figure 3.2** and **Supplemental Figure 3.3**). To investigate the degree of reduction of Co-{P_5W_{30}}, electron titration against 0.1 M $Cu(OTf)_2$ solution was conducted. Through three titrations, it was determined that the average electron count per cluster is 8.9 electrons (**Supplemental Figure 3.4**). With inductively coupled plasmon mass spectrometry and thermogravimetric analysis, a formula of $H_{4.7}K_{6.1}Co_{5.9}[NaP_5W_{30}O_{110}]\bullet 60H_2O$ was determined for Co-{P_5W_{30}} (**Supplemental Table 3.6** and **Supplemental Figure 3.5**).

Powder X-ray diffraction of bulk Co-{P_5W_{30}} often showed no evidence of Co^0 formation at the cathode. By carefully scraping the cathode surface, however, very tiny metallic pellets were isolated in a divided cell reaction (*vide infra*), and they were identified as Co^0 through X-ray diffraction (**Supplemental Figure 3.21**). XPS was carried out on a sample where no Co^0 was detected by XRD, which was prepared by carefully isolating the material without scraping the cathode surface. XPS fit data showed that Co^0 was present in the sample, accounting for 8.53% of total Co atom count (**Supplemental Figure 3.3**). This implies the reduction of cations during electrocrystallization, as the continued formation of materials throughout electrolysis period and lack of void space in the Co-{P_5W_{30}} crystal structure suggest the electron conduction through the synthesized Co-{P_5W_{30}} material. It should be noted, however, that the sensitivity of powder XRD for detecting Co^0 at such small amounts is limited. Therefore, it is possible that Co^0 detected from XPS is indeed from the reduction of Co^{2+} at cathode surface. Meanwhile, the ratio between W^{5+} and W^{6+} was calculated to be 1:2.87, indicating that 7.8 out of 30 W atoms in {P_5W_{30}} were reduced (**Supplemental Figure 3.2**). The total number of electrons reduced per {P_5W_{30}} is 8.8 e^- per XPS analysis, which is in fair agreement with electron titration data of 8.9 e^-/{P_5W_{30}}.

Scanning electron microscopy images of Co-{P_5W_{30}} show full coverage of the cathode with thin crystalline plates growing outward (**Supplemental Figure 3.19**). A single crystalline plate was carefully isolated and the crystal faces were indexed subsequently using video microscopy. Face assignment on the crystal revealed that the primary direction of crystal growth is by (100) axis, which is the same direction as O_{cap1}–Co–O_{cap2} linkages (**Supplemental Figure 3.20**). Density functional theory (DFT) calculations and electrostatic potential (EP) mapping by Fernández et al. showed that the lowest unoccupied molecular orbital (LUMO) of {P_5W_{30}} is delocalized mainly over cap positions of {P_5W_{30}} and that O_{cap} is more nucleophilic than O_{belt}.[29] It can be hypothesized that electrochemical reduction of {P_5W_{30}} results in higher nucleophilicity at O_{cap} positions compared to O_{belt} positions initially. Therefore, metal cations are first attracted to the sandwiched location between the cap positions of two {P_5W_{30}} molecules, making it the primary site of 1D chain elongation.

To understand the full-cell reaction, efforts to identify the black anodic products were carried out, however, the exact speciation could not be identified through FT-IR or XRD analysis, due to its amorphousness (**Supplemental Figure 3.15**) Energy dispersive X-ray (EDX) analysis shows that the material's Co and {P_5W_{30}} ratio is 176.9:1, suggesting that the primary anodic reaction is Co^{2+} oxidation to Co^{3+}, which attracted some {P_5W_{30}} in the electrolytic solution (**Supplemental Table 3.7**).

To have a defined anodic reaction, sacrificial anodes were utilized. When copper wire was used, Cu^{2+} from anode oxidation diffused to the cathode and got reduced, resulting in Cu^0 crystallizing as impurities of cathodic product (**Supplemental Figure 3.16**). To ensure the presence of single transition-metal linker species, the anode was switched to cobalt wire. As Co^0 is slightly more reducing than {P_5W_{30}}, background reduction of {P_5W_{30}} was observed near the

anodic surface. The reduced $\{P_5W_{30}\}$ species from the reaction with Co^0 diffused from the anode to cathode, leading to the formation of a cathodic product with different phase than Co-$\{P_5W_{30}\}$ (**Supplemental Figure 3.17**). This product, however, exhibited poor crystallinity compared to Co-$\{P_5W_{30}\}$ and was not suitable for single-crystal X-ray diffraction.

A divided cell setup was implemented to deter the side reaction on anodic surface. In this setup, $\{P_5W_{30}\}$ was only added to cathodic compartment, whereas $Co(OAc)_2$ was added to both anodic and cathodic cells. When electrocrystallization was conducted in this experimental condition, cathodic product of same speciation as Co-$\{P_5W_{30}\}$ was synthesized and this was analyzed through powder and single-crystal X-ray diffraction (**Supplemental Figure 3.18**). By using cobalt wire as sacrificial anode in a divided cell, the chemical equation for anodic reaction can be defined as:

$$Co \rightarrow Co^{2+} + 2e^{-} \qquad (1)$$

The cathodic reaction equation was achieved by identifying the degree of reduction and elemental composition of the product. The materials were titrated against Cu^{2+} solution of a known concentration, using electronic absorption spectroscopy to determine the extent of Cu^{2+} reduction and calculate the numbers of electrons per cluster. The titration results showed that the material was reduced by 8.6 $e^-/\{P_5W_{30}\}$. By incorporating this value with the empirical formula derived from ICP-MS data, the chemical equation of cathodic reaction can be determined as:

$$[NaP_5W_{30}O_{110}]^{14-} + 5.9\ Co^{2+} + 8.6\ e^{-} \rightarrow H_{4.7}K_{6.1}Co_{5.9}[NaP_5W_{30}O_{110}] \qquad (2)$$

By combining two half reaction, the total cell reaction can be identified as:

$$[NaP_5W_{30}O_{110}]^{14-} + 5.9\ Co \rightarrow H_{4.7}K_{6.1}Co_{5.9}[NaP_5W_{30}O_{110}] + 3.2\ e^- \quad (3)$$

The 3.2 e^- on the right side of the equation can be attributed to side reactions, such as Co^{2+} reduction, and re-oxidation of reduced $\{P_5W_{30}\}$ and the material as the reaction was carried out in air.

When $Co(OAc)_2 \cdot 4H_2O$ was replaced with an equimolar amount of nickel acetate tetrahydrate ($Ni(OAc)_2 \cdot 4H_2O$) or zinc acetate dihydrate ($Zn(OAc)_2 \cdot 2H_2O$), a Ni-bridged network (Ni-$\{P_5W_{30}\}$) or Zn-bridged network (Zn-$\{P_5W_{30}\}$) of isomorphic structure were synthesized, respectively (**Supplemental Table 3.1**). In the case of Zn-$\{P_5W_{30}\}$, however, Zn^{2+} reduction to Zn^0 was much more evident than Co^{2+} reduction in the Co-$\{P_5W_{30}\}$ synthesis, as Zn^0 was easily detected through powder X-ray diffraction (**Supplemental Figure 3.7**).

When K^+ was exchanged for Li^+ or Na^+, which have lower ion-pairing strength with $\{P_5W_{30}\}$, no product was crystallized. Instead, dark blue solutions resulting from solubilized reduced $\{P_5W_{30}\}$ were observed.

To further extend the synthesis, $Co(OAc)_2 \cdot 4H_2O$ was replaced with yttrium acetate tetrahydrate ($Y(OAc)_3 \cdot 4H_2O$). The stronger ion-pairing of Y^{3+} to the cluster introduced challenges in adapting the synthetic protocols of first-row transition-metal networks. When $\{P_5W_{30}\}$ was added to a $Y(OAc)_3$ solution, which was prepared in 0.05 M KOAc buffer and had the same final pH value as $Co(OAc)_2$ electrolytic solution, a white precipitate readily formed. Electrocrystallization attempts on this suspension yielded phase-impure products (**Supplemental Figure 3.8** and **Supplemental Figure 3.9**). Fourier-transform infrared spectroscopy (FT-IR) data

of the initial white precipitate showed the characteristic P–O peaks of {P_5W_{30}}, indicating the presence of {P_5W_{30}} in the precipitate (**Supplemental Figure 3.10**). To deter precipitation prior to the electrochemical reaction, the pH of the electrolytic solution was lowered by using 0.05 M HOAc solution and acid-{P_5W_{30}} ($H_{14}[NaP_5W_{30}O_{110}]•15H_2O$), in place of KOAc buffer and potassium salt of {P_5W_{30}} ($K_{14}[NaP_5W_{30}O_{110}]•15H_2O$). The resulting Y^{3+} solution had a pH of 4.6 and was free of precipitate. Electrolysis of this solution yielded crystals of phase-pure Y^{3+}-bridged framework, Y-{P_5W_{30}} (**Supplemental Figure 3.11** and **Supplemental Figure 3.12**). The crystal structure of Y-{P_5W_{30}} is in the monoclinic space group *C2/m* (**Supplemental Table 3.1**, a = 30.889(4) Å, b = 16.1811(18) Å, c = 17.7813(19) Å, α = 90°, β = 117.516(3)°, γ = 90°), which is different from that of Co-{P_5W_{30}}, Ni-{P_5W_{30}}, and Zn-{P_5W_{30}}. In the Y-{P_5W_{30}} structure, 1D chains of clusters and transition-metal–aquo complexes are also present, but there is no direct O_{cap}–Y–O_{cap} coordination as seen in first-row transition-metal counterexamples. Instead, the structure is elongated through O_{cap}–Y–Y–O_{cap} connections (**Supplemental Figure 3.13**). Cluster-decorating $Y(H_2O)_6^{3+}$ fragments are shared by two clusters at each O_{belt} position, linking the chains through O_{belt}–Y–O_{belt} coordination (**Supplemental Figure 3.14**). With the exclusion of K^+ in the synthesis, the negative charge of {P_5W_{30}} is balanced by Y^{3+} and protons in the crystal lattice, although proton positions are not defined in the crystallographic solution.

Notably, the Y-{P_5W_{30}} structure features an O_{belt}–Y–O_{belt} connection, which is distinct from the O_{belt}–M–M–O_{belt} connection observed in 1st-row transition metal counterparts. Additionally, an O_{cap}–Y–Y–O_{cap} connection is present at the O_{cap} positions, contrasting with the O_{cap}–M–O_{cap} connection found in first-row transition-metal coordination networks. This may be due to the difference in coordination numbers between Y^{3+} and Co^{2+}, Ni^{2+}, or Zn^{2+}, in addition to the difference in ionic radii. While Co^{2+}, Ni^{2+}, and Zn^{2+} typically adopt a six-coordinated

octahedral environment in aqueous conditions, Y^{3+} coordinates to eight aquo ligands and facilitates more flexible coordination geometries.[30]

As demonstrated by the absence of product formation when K^+ is replaced with Li^+ and Na^+, ion-pairing of charge-balancing cations to $\{P_5W_{30}\}$ appears to be a significant factor in electrocrystallization, as observed in previous studies on effects of ion pairs in network assemblies.[31] The hydrodynamic radius of Y^{3+} is similar to that of K^+, but its larger positive charge results in a higher calculated charge density compared to K^+. This may lead to higher ion-pairing strength with $\{P_5W_{30}\}$. This is supported by the formation of a precipitate containing $\{P_5W_{30}\}$ when the cluster was added to a $Y(OAc)_3$ solution prepared in a 0.05 M KOAc buffer (pH = 5.6). In contrast, no precipitate was formed when $\{P_5W_{30}\}$ was dissolved in a 0.05 M KOAc buffer (pH = 5.6) or in Co-, Ni-, or $Zn(OAc)_2$ solutions prepared in the same buffer, all at the same final pH value. Indeed, Y-$\{P_5W_{30}\}$ was crystallized without K^+ in the electrolytic solution. Importantly, the extension of synthetic platform to Y^{3+} suggests potential application to other 2nd-row transition metals and lanthanides.[32]

In a previous report,[33] Zn-bridged Mo-doped Preyssler ($[NaP_5MoW_{29}O_{110}]^{14-}$, denoted as $\{P_5MoW_{29}\}$) framework demonstrated remarkable stability in retaining its reduced state. We sought to determine if the Zn-bridged $\{P_5MoW_{29}\}$ network could be synthesized electrochemically, and if so, whether similar stability could be observed in electrocrystallized Zn-$\{P_5MoW_{29}\}$. By replacing $\{P_5W_{30}\}$ with $\{P_5MoW_{29}\}$ in the synthesis of Zn-$\{P_5W_{30}\}$, an isomorphic structure in the orthorhombic *Cmcm* space group was synthesized, despite the LUMO being expected to be localized on the Mo atom. Preliminary stability of this structure was tested by powder X-ray diffraction (**Supplemental Figure 3.22**). The crystals were crushed, and powder patterns were collected daily for 8 days. On day 2, a significant change in the powder

pattern compared to day 1 was observed. This pattern remained consistent throughout the remainder of the experimental period, except for some discrepancies on day 7. On day 4, single-crystal X-ray diffraction data were collected, and a preliminary structure in the monoclinic $P2_1/m$ space group was solved (**Supplemental Figure 3.23**). This structure features a 1D chain connected through O_{belt}-Zn-O_{belt} connections. Since the Mo atom is expected to be doped in the belt position of the Preyssler anion, these connections are consistent with the expected LUMO localization,[12] suggesting the retention of reduction at the LUMO. Further XPS, crystal structure refinement, and powder XRD data collection on this network, coupled with computational calculations on $\{P_5MoW_{29}\}$ LUMOs, will help to better understand the system.

3.4 Conclusion

In summary, we have demonstrated the application of electrochemical methods in the synthesis of new metal oxide coordination networks. The resulting compounds feature unique one-dimensional chains of $\{P_5W_{30}\}$ and transition metal aquo complex fragments, connected through exclusive cap-to-cap linkages. Additionally, the compounds were crystallized directly on the electrode surface, which could facilitate convenient electrochemical studies and applications in areas such as sensing, electrochromism, and electronics. To date, these compounds are the first examples of electrocrystallized $\{P_5W_{30}\}$-based coordination networks. Electrocrystallization presents a promising synthetic platform with considerable potential for further exploration.

Chapter 3, in part, is currently being prepared for submission for publication of the material. The dissertation author would like to acknowledge the contributions of the co-authors Linfeng Chen, Carl Lemmon, Erika Samolova, Milan Gembicky, and Alina M. Schimpf. The dissertation author was the primary researcher and author of this material.

3.5 Supplemental Information

3.5.1 Chemicals

Chemical	Purity	Manufacturer
Cobalt(II) acetate tetrahydrate (Co(OAc)2•4H2O)	99.6%	Chem-Impex International
Nickel(II) acetate tetrahydrate (Ni(OAc)2•4H2O)	98%	Sigma-Aldrich
Zinc(II) acetate dihydrate (Zn(OAc)2•2H2O)	100%	Ward's Science
Yttrium(III) acetatate tetrahydrate (Y(OAc)3•4H2O)	99.9%	Fisher Chemical
Potassium acetate	>99.0%	Sigma-Aldrich
Acetic acid	99.8%	Fisher Chemical
Hydrochloric acid (HCl)	36.5%	Fisher Chemical
Sodium tungstate dihydrate	95%	Spectrum Chemical
Phosphoric acid (H_3PO_4)	85%	Acros Organics
Sodium chloride	>99%	Fisher Chemical
Potassium chloride	99%	Alfa Aesar

3.5.2 Characterization

Formula determination. The degree of reduction was determined by electron counting through titration against a 0.1 M $Cu(OTf)_2$ solution prepared in 1:2:7 mixture of methanol, toluene, and toluene, following the procedure reported previously.[11] Inductively coupled plasma mass spectrometry (ICP-MS) data were acquired using a Thermo Scientific iCAP RQ ICP-MS mass spectrometer. For sample digestion, a 1:1 mixture of 85% HNO_3 (Optima grade, Sigma-Aldrich) and 30% H_2O_2 (Trace metal grade, Sigma-Aldrich) was used. The samples were digested under ultrasonication for 48 hours. Thermogravimetric analysis (TGA) was performed under N_2 flow with a heating rate of 5 °C/s using a TA Instruments Discovery SDT 650 thermal analyzer. The % weight loss within the 20–600 °C temperature range was attributed to water loss, and the number of water molecules in the formula was rounded to the nearest whole number.

Single crystal X-ray crystallography. Single crystal X-ray diffraction data for Co-, Ni-, Zn-, and Y-{P_5W_{30}} were collected on Bruker APEX II-Ultra CCD diffractometer with APEX II detector, while data for Zn-{P_5MoW_{29}} were collected on Bruker D8 Venture diffractometer with Bruker Photon III detector. Both diffractometers were equipped with Mo Kα radiation sources and all data were collected at 100 K under a flow of nitrogen. Crystallographic solutions were achieved via direct methods with SHELXT[34] and were subsequently refined using SHELXL[35] full-matrix least-squares procedures. Anisotropic restraints were applied to all non-hydrogen atoms. Residual electron density from disordered water molecules were refined using Olex2[36] Solvent Mask.

Powder X-ray diffraction. All powder X-ray diffraction data were collected on a Bruker 3-Circle diffractometer equipped with Cu Kα radiation source and APEX II CCD detector. All data were collected at 100 K under a nitrogen flow, except for Zn-{P_5MoW_{29}} stability test data, which were collected at room temperature.

Other characterization. Fourier-transform infrared spectroscopy (FT-IR) was conducted on an Agilent Cary 630 ATR-FTIR. ^{31}P nuclear magnetic resonance spectroscopy (NMR) data were collected on a JEOL ECA 500 MHz spectrometer with an internal standard of 85% H_3PO_4 capillary tube.

3.5.3 Synthesis

Synthesis of potassium salt of {P_5W_{30}}, $K_{14}[NaP_5W_{30}O_{110}]\cdot 14H_2O$. The Preyssler clusters with K^+ as charge balancing cations were synthesized following a reported procedure.[37] Specific procedures, reagent amounts, and notes are shared in Chapter 2 of this dissertation.

Synthesis of acid form of {P_5W_{30}}, $H_{14}[NaP_5W_{30}O_{110}]\bullet 15H_2O$. The acid Preyssler clusters were synthesized through ion exchange method, following a reported procedure.[38] Specific procedures, reagent amounts, and notes are shared in Chapter 2 of this dissertation.

All M-{P_5W_{30}} syntheses were conducted in air and isolated samples were washed with methanol under an argon flow prior to characterization, except for single-crystal X-ray diffraction.

Synthesis of Co-{P_5W_{30}}. ***Undivided*:** To a 20 ml scintillation vial, $K_{14}[NaP_5W_{30}O_{110}]\bullet 14H_2O$ (65.0 mg, 7.88 μmol) and $Co(OAc)_2\bullet 4H_2O$ (135.0 mg, 542.0 μmol) were added then dissolved in 10 ml of 0.05 M KOAc buffer (pH = 5.6). To this electrolyte solution, two platinum electrodes were dipped (~ 1.5 cm, geometric area of ca. 0.24 cm^2) and current of 50 μA was applied for 20 hours. Dark blue crystals were isolated on the cathode for further measurements. ***Divided*:** To a H-cell (fine frit, ~7 mL each compartment), a 5 ml solution of $K_{14}[NaP_5W_{30}O_{110}]\bullet 14H_2O$ (32.5 mg, 3.94 μmol) and $Co(OAc)_2\bullet 4H_2O$ (67.5 mg, 271 μmol), prepared in 0.05 M KOAc buffer (pH = 5.6), was placed in the cathodic compartment. Another 5 ml solution of $Co(OAc)_2\bullet 4H_2O$ (67.5 mg, 271 μmol), prepared in 0.05 M KOAc buffer (pH = 5.6), was placed in the anodic compartment. The cell was equipped with a platinum wire (~1.5 cm dipped in solution, geometric area of ~0.24 cm^2) as the cathode and a cobalt wire as the sacrificial anode. A current of 50 μA was applied for 20 hours. Dark blue crystals formed on the cathode were isolated for further measurements.

Synthesis of Ni-{P_5W_{30}}. ***Undivided:*** To a 20-ml scintillation vial, K_{14}[NaP5W30O110]$\bullet 14H_2O$ (65.0 mg, 7.88 μmol) and Ni(OAc)2$\bullet 4H_2O$ (134.9 mg, 542.0 μmol) were added then dissolved in 10 ml of 0.05 M KOAc buffer (pH = 5.6). To this electrolyte solution, two platinum electrodes were dipped (~ 1.5 cm, geometric area of ca. 0.24 cm^2) and

current of 50 μA was applied for 20 hours. Dark blue crystals were isolated on the cathode for further measurement.

Synthesis of Zn-{P_5W_{30}}. ***Undivided:*** To a 20-ml scintillation vial, $K_{14}[NaP_5W_{30}O_{110}]•14H_2O$ (65.0 mg, 7.88 μmol) and $Zn(OAc)_2•2H_2O$ (119.0 mg, 542.0 μmol) were added then dissolved in 10 ml of 0.05 M KOAc buffer (pH = 5.6). To this electrolyte solution, two platinum electrodes were dipped (~ 1.5 cm, geometric area of ca. 0.24 cm^2) and current of 50 μA was applied for 20 hours. Dark blue crystals were isolated on the cathode for further measurement.

Synthesis of Y-{P_5W_{30}}. ***Undivided:*** To a 20-ml scintillation vial, $H_{14}[NaP_5W_{30}O_{110}]•15H_2O$ (60.9 mg, 7.88 μmol) and $Y(OAc)_3•2H_2O$ (183.2 mg, 542.0 μmol) were added then dissolved in 10 ml of 0.05 M $HOAc_{(aq)}$. To this electrolyte solution, two platinum electrodes were dipped (~ 1.5 cm, geometric area of ca. 0.24 cm^2) and current of 50 μA was applied for 20 hours. Dark blue crystals were isolated on the cathode for further measurement.

Synthesis of Zn-{P5MoW29}. ***Undivided:*** To a 20-ml scintillation vial, $K_{14}[NaP_5MoW_{29}O_{110}]•14H_2O$ (63.2 mg, 7.88 μmol) and $Zn(OAc)_2•2H_2O$ (119.0 mg, 542.0 μmol) were added then dissolved in 10 ml of 0.05 M KOAc buffer (pH = 5.6). To this electrolyte solution, two platinum electrodes were dipped (~ 1.5 cm, geometric area of ca. 0.24 cm^2) and current of 50 μA was applied for 20 hours. Dark blue crystals were isolated on the cathode for further measurement.

3.5.4 Appendix

Supplemental Table 3.1. Crystallographic parameters of electrochemically synthesized coordination networks.

	Co-{P_5W_{30}}	**Ni-{P_5W_{30}}**	**Zn-{P_5W_{30}}**	**Y-{P_5W_{30}}**
Empirical formula	$Co_{5.8}K_{7.4}NaO_{163.4}P_5W_{30}$	$Ni_{5.5}K_{9.3}NaO_{162.6}P_5W_{30}$	$Zn_{5.4}K_{7.2}NaO_{162.8}P_5W_{30}$	$Y_{5.5}NaO_{147.4}P_5W_{30}$
Formula weight	8939.31	8978.53	8933.36	8539.72
Radiation (Å)	MoK_α (λ = 0.71073)	MoK_α (λ = 0.71073)	MoK_α (λ = 0.71073)	MoK_α (λ = 0.71073)
Temperature (K)	100	100	100	100
Crystal size (mm)	0.08 × 0.05 × 0.03	0.08 × 0.05 × 0.03	0.08 × 0.05 × 0.03	0.02 × 0.18 × 0.12
Crystal system	Orthorhombic	Orthorhombic	Orthorhombic	Monoclinic
Space group	*Cmcm*	*Cmcm*	*Cmcm*	C2/m
a (Å)	14.0654(8)	14.0825(6)	14.0825(6)	30.889(4)
b (Å)	33.6984(19)	33.7686(14)	33.7686(14)	16.1811(18)
c (Å)	30.2745(17)	30.3252(13)	30.3252(13)	17.7813(19)
α (°)	90	90	90	90
β (°)	90	90	90	117.516(3)
γ (°)	90	90	90	90
Volume ($Å^3$)	14349.6(14)	14421.0(11)	14421.0(11)	7882.1(15)
Z	4	4	4	2
ρ_{calc} (g/cm^3)	4.117	4.135	4.115	3.598
μ (mm^{-1})	24.869	24.968	25.094	23.938
Goodness-of-fit on F^2	1.012	1.052	1.018	1.035
Reflections collected	43524	50661	50727	91630
Independent reflections	7567	7834	7857	7768
R_1	0.0217	0.0255	0.0290	0.0378
wR_2	0.0446	0.0479	0.0535	0.0898

Supplemental Table 3.2. Summary of Co connections in Co-{P_5W_{30}}.

Co label	Occupancy	Connectivity	$O_{cluster}$–Co Bond Distances (Å)
1	0.25	Co_1–Co_5 Co_1–O	
2	0.675(4)	Co_2–O_{belt} Co_2–Co_4 Co_2–O–Co_4	2.105(4)
3	0.313(5)	Cap to cap Co_3–O–Co_3 Co_3–O–Co_5	1.984(4) 1.985
4	0.178(4)	Co_4–O_{belt}	2.135
5	0.637(5)	Cap to cap	1.987(4) 1.988

Supplemental Table 3.3. Summary of Ni connections in Ni-{P_5W_{30}}.

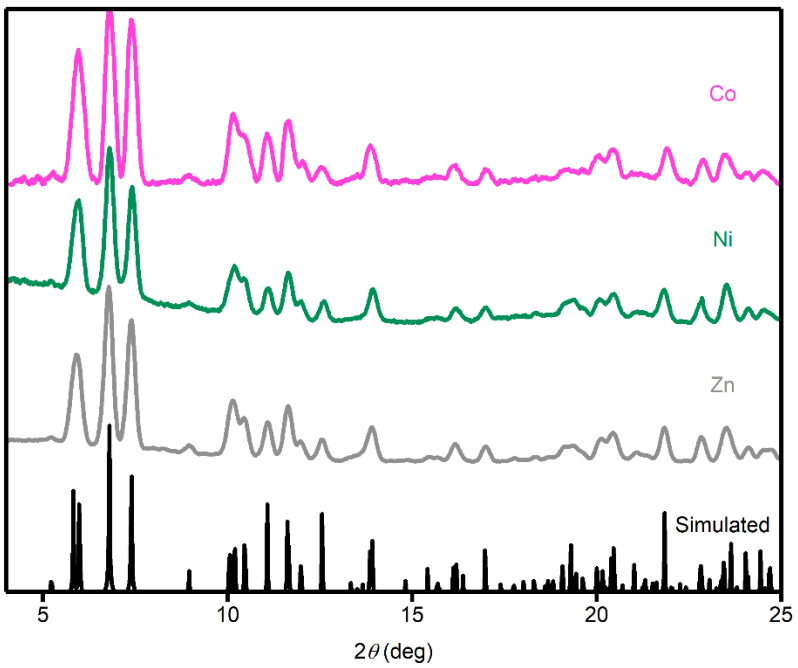
Ni label	Occupancy	Connectivity	$O_{cluster}$–Ni Bond Distances (Å)
1	0.811(4)	Ni_1–O_{belt} Ni_1–Ni_{55} Ni_1–O–Ni_{55}	2.038(5)
2	0.706(6)	Cap to cap Ni_2–O–Ni_3	1.972(5) 1.973
3	0.250(6)	Cap to cap Ni_3–O–Ni_3	1.965 1.965(5)
55	0.076(4)	Ni_{55}–O_{belt}	2.145

Supplemental Table 3.4. Summary of Zn connections in Zn-{P_5W_{30}}.

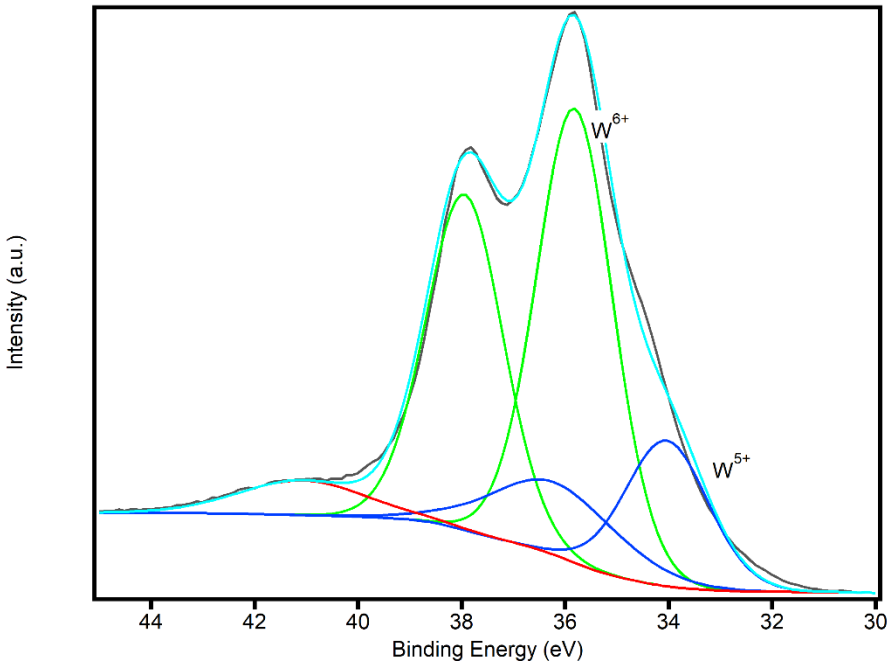
Zn label	Occupancy	Connectivity	$O_{cluster}$–Zn Bond Distances (Å)
1	0.283(6)	Cap to cap Zn_1–O–Zn_1 Zn_1–O–Zn_2	1.987 1.987(6)
2	0.675(6)	Cap to cap	1.997 1.997(6)
3	0.698(4)	Zn_3–O_{belt} Zn_3–Zn_4 Zn_3–O–Zn_4	2.108(6)
4	0.174(4)	Zn_4–O_{belt}	2.155

Supplemental Table 3.5. Summary of Y connections in Y-{P_5W_{30}}.

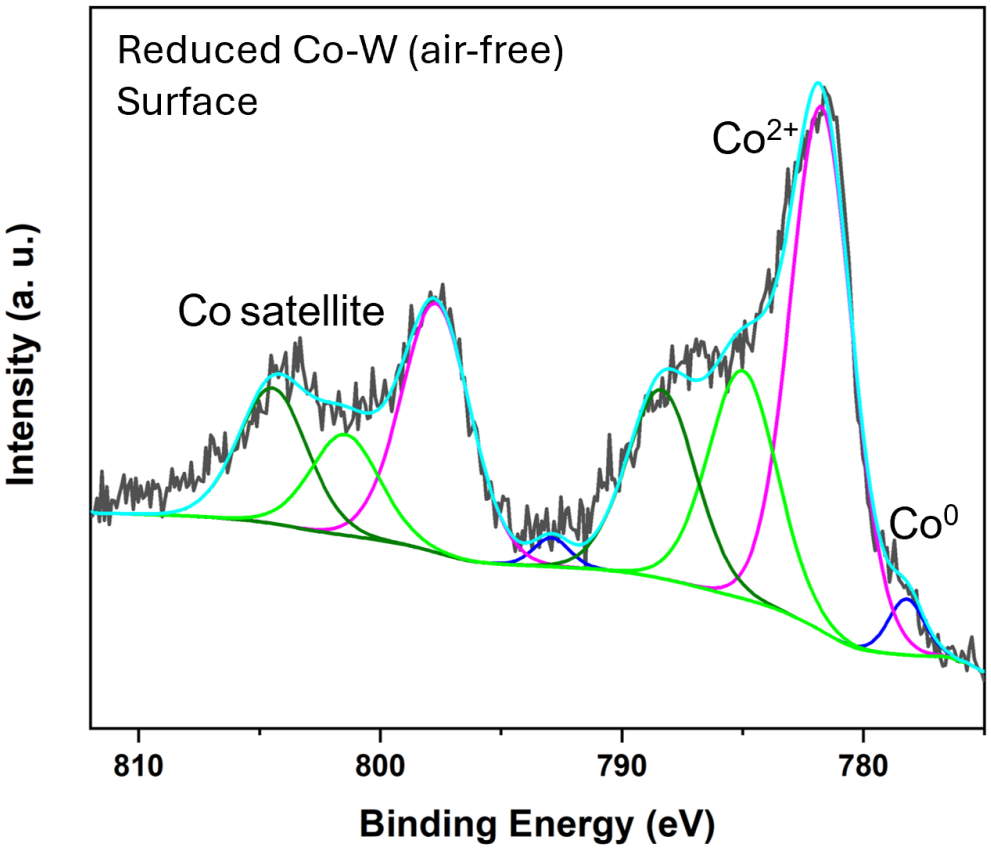
Y label	Occupancy	Connectivity	$O_{cluster}$–Y Bond Distances (Å)
1	0.517(6)	Belt to belt Y_1–O–Y_4	2.280 2.280(9)
4	0.148(5)	Belt to belt Y_4–Y_4	2.242(15) 2.290(14)
8	0.137(8)	Y_8–O_{cap} Y_8–Y_8 Y_8–O–Y_8	2.21(2)



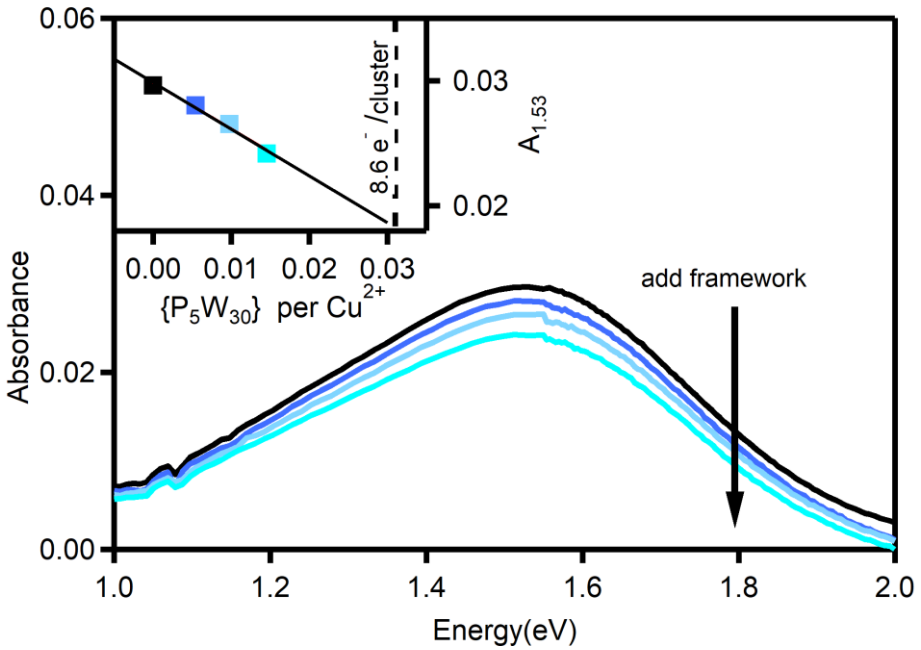
Supplemental Figure 3.1. Powder X-ray diffraction patterns of (i) Co-{P_5W_{30}}, (ii) Ni-{P_5W_{30}}, and (iii) Zn-{P_5W_{30}} compared to (iv) powder pattern simulated from single-crystal X-ray diffraction data.



Supplemental Figure 3.2. W*4f* X-ray photoelectron spectra of Co-{P_5W_{30}}.



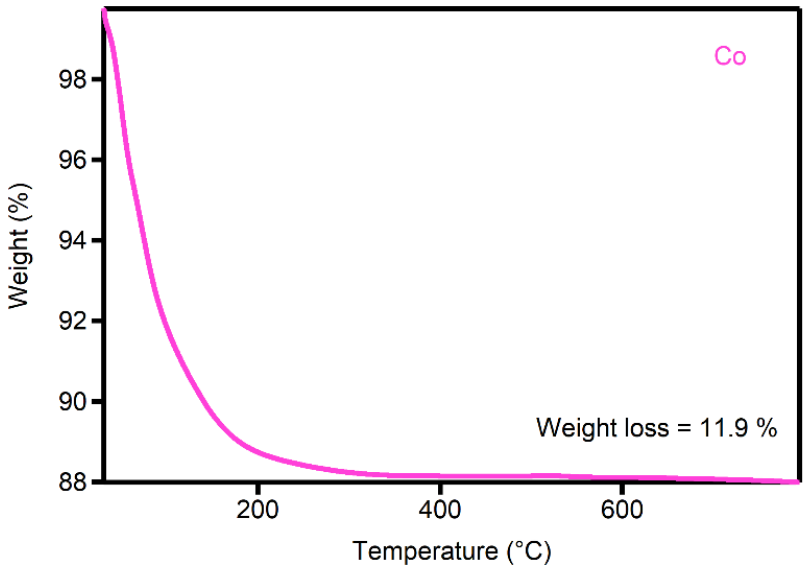
Supplemental Figure 3.3. Co*2p* X-ray photoelectron spectra of Co-{P_5W_{30}}.



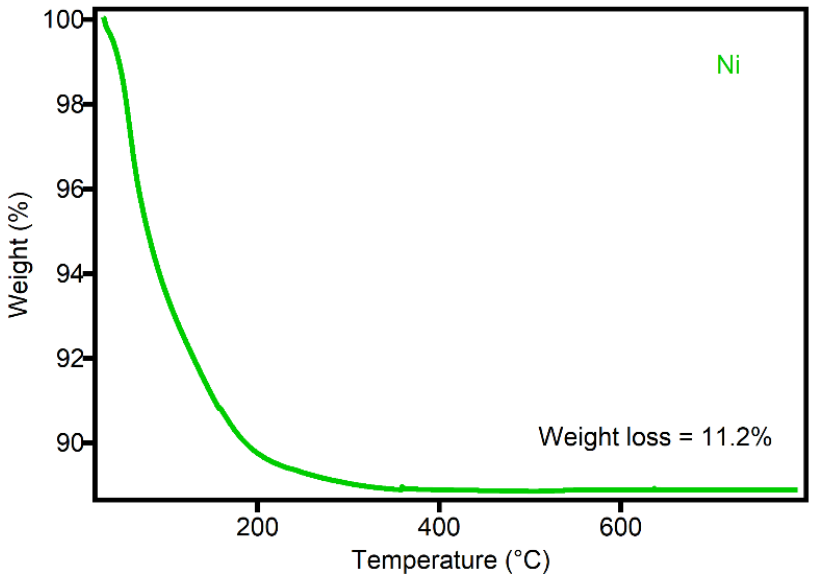
Supplemental Figure 3.4. Electron titration of Co-{P_5W_{30}}.

Supplemental Table 3.6. Inductively coupled plasmon mass spectroscopy data of electrocrystallized coordination networks.

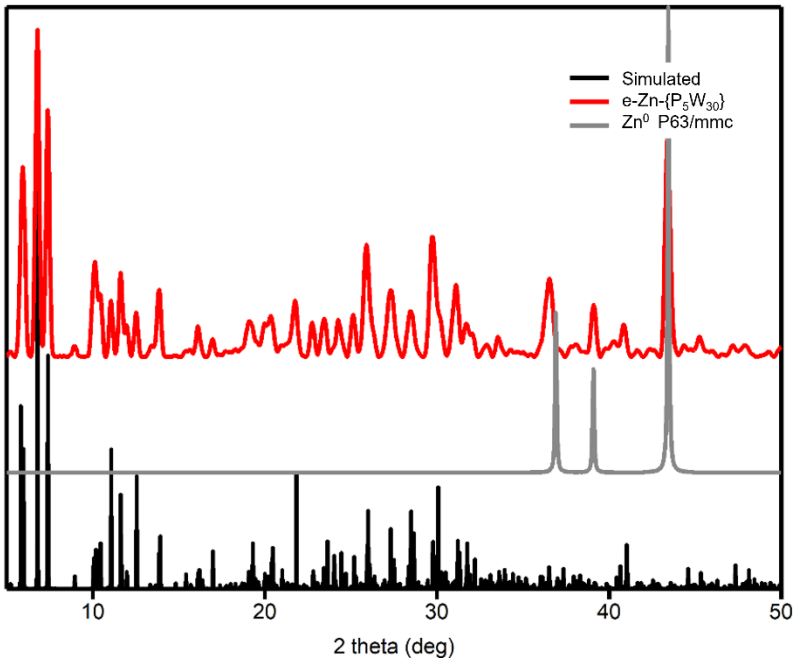
	Na	P	K	Co	Ni	Zn	Y	Mo	W
Co-{P_5W_{30}}	0.9	5.0	6.1	5.9					30
Ni-{P_5W_{30}}	1.0	5.1	6.9		5.7				30
Zn-{P_5W_{30}}	0.9	5.1	6.7			5.2			30
Y-{P_5W_{30}}	0.7	4.6					6.0		30
Zn-{P_5MoW_{29}}	0.9	4.8	6.9			7.0		1.0	29.0



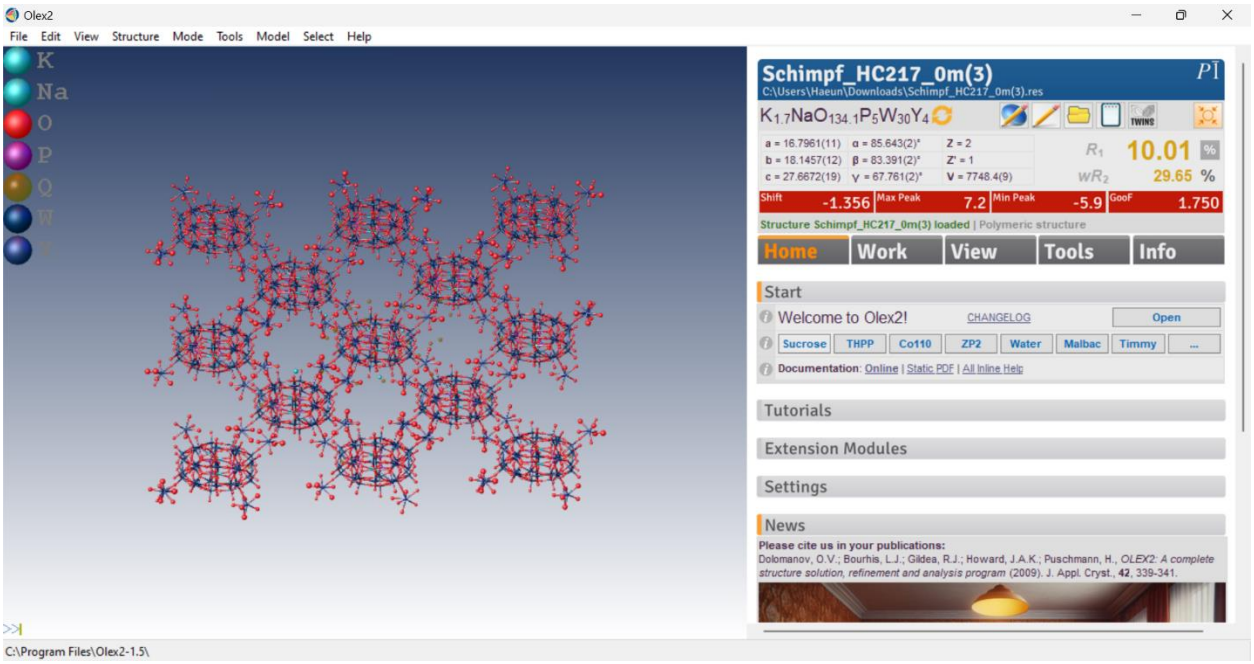
Supplemental Figure 3.5. Thermogravimetric analysis data of Co-{P_5W_{30}}. Weight loss of 11.9 % is accounted for water lost from the structure.



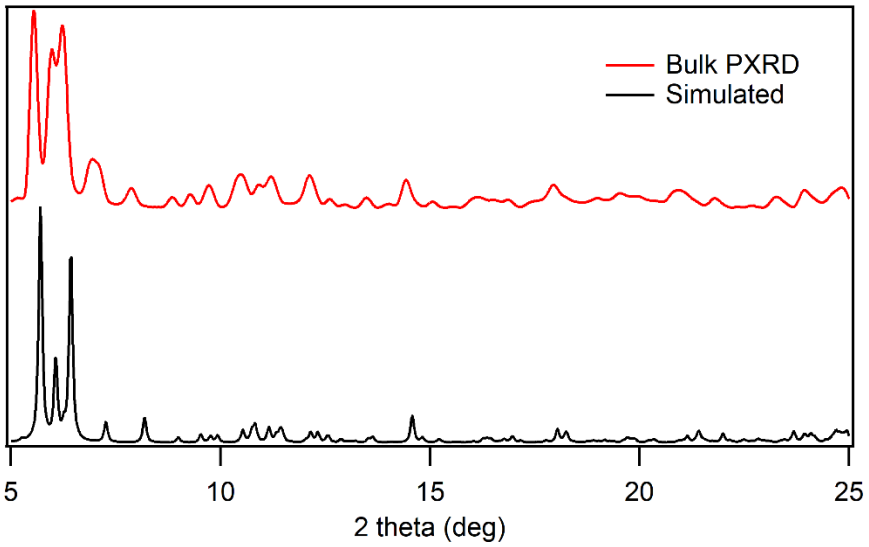
Supplemental Figure 3.6. Thermogravimetric analysis data of Ni-{P_5W_{30}}. Weight loss of 11.2 % is accounted for water lost from the structure.



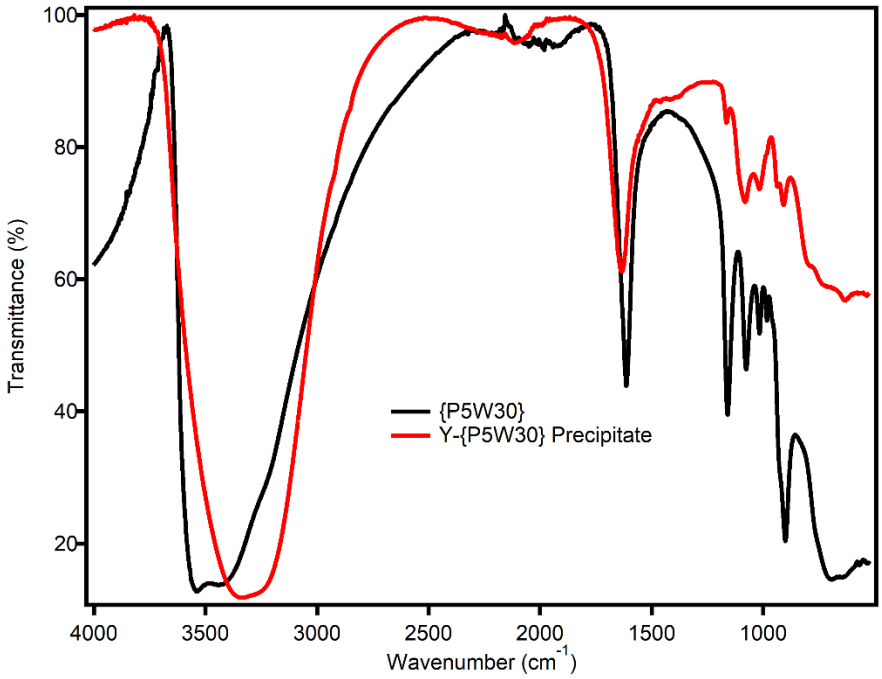
Supplemental Figure 3.7. Powder X-ray diffraction pattern of (i) Zn-{P_5W_{30}}, compared to simulated powder patterns of (ii) Zn^0 P63/mmc, and (iii) crystal structure of Zn-{P_5W_{30}}.



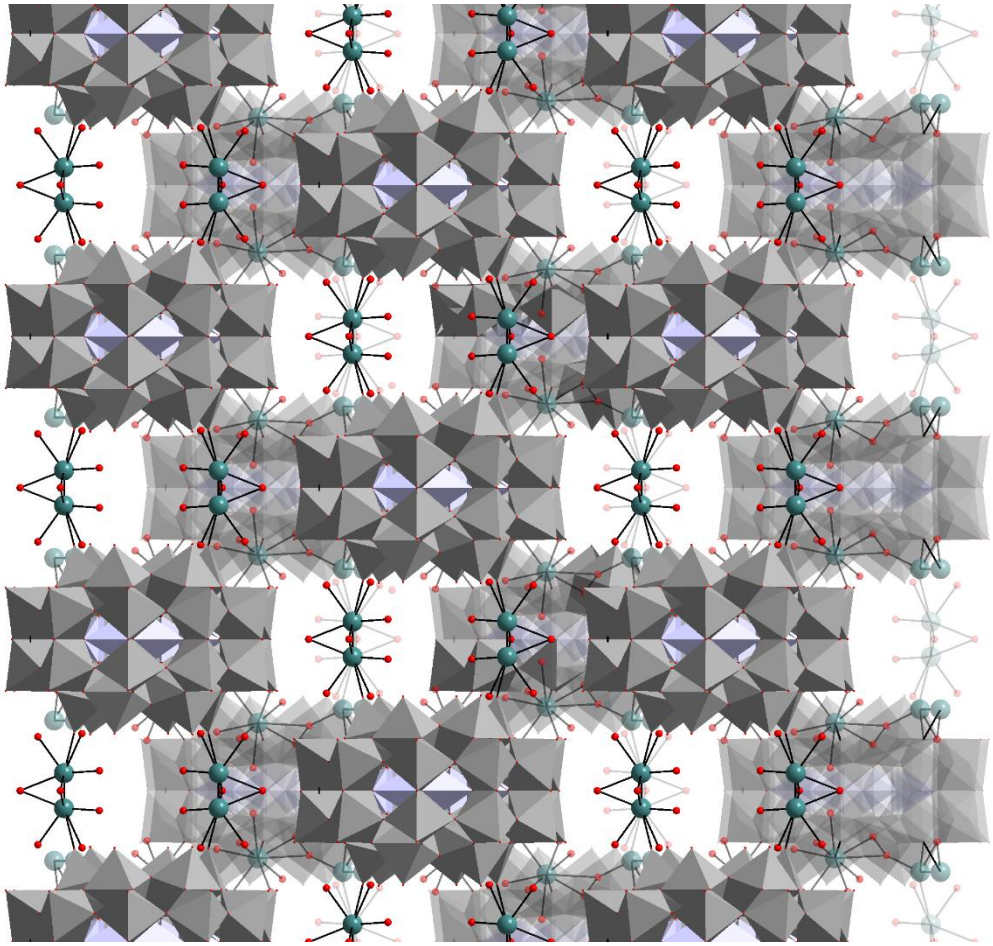
Supplemental Figure 3.8. Preliminary crystal structure solution of single-crystal isolated from an electrocrystallization reaction of electrolytic solution of $K_{14}[NaP_5W_{30}O_{110}]\bullet 14H_2O$ (65.0 mg, 7.88 μmol) and $Y(OAc)_3\bullet 2H_2O$ (183.2 mg, 542.0 μmol) prepared in 10 ml of 0.05 M KOAc buffer (pH = 5.6).



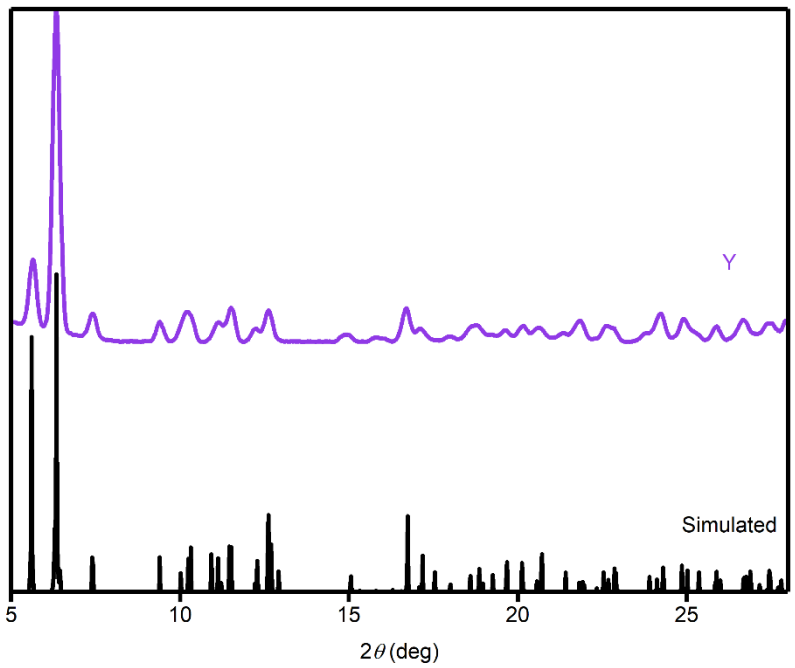
Supplemental Figure 3.9. Simulated powder X-ray pattern of the preliminary structure shown in Supplemental Figure 3.8 compared to the experimental powder X-ray pattern of bulk product from the same reaction.



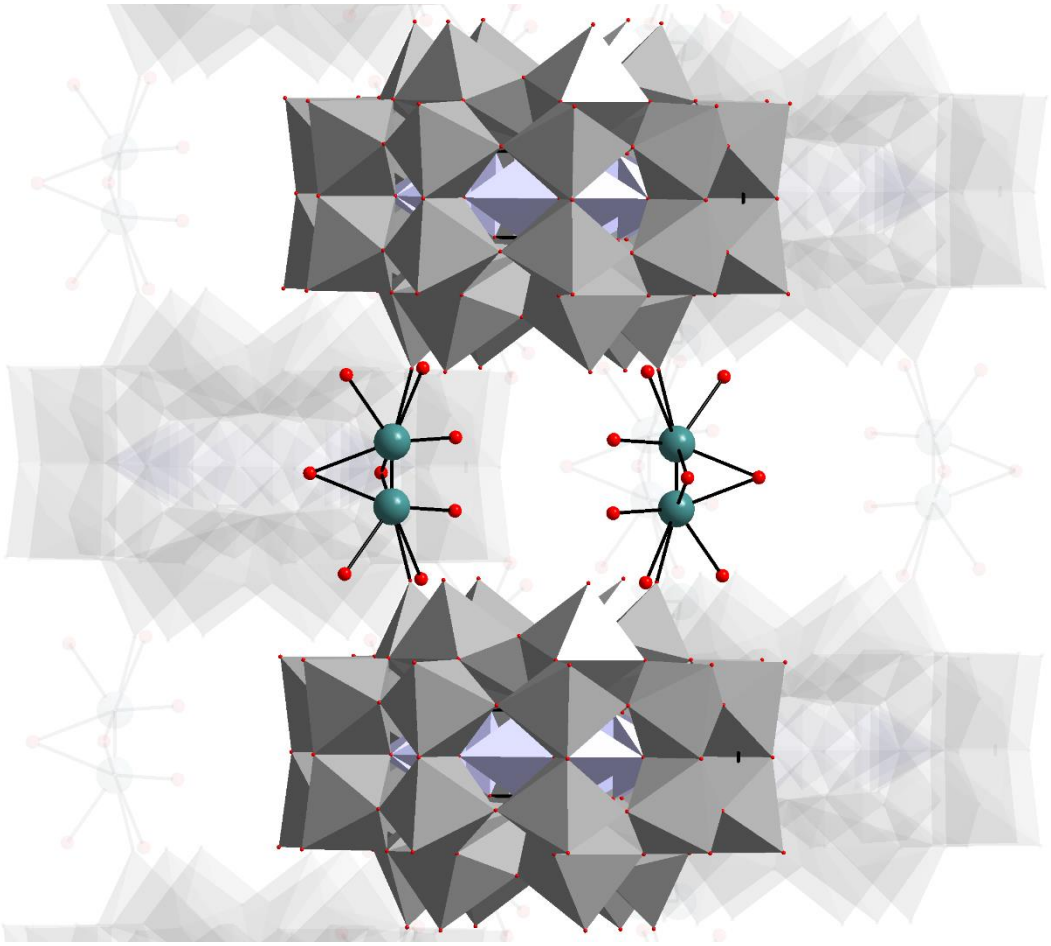
Supplemental Figure 3.10. FT-IR spectra of (i) $\{P_5W_{30}\}$ and (ii) white precipitate isolated from $\{P_5W_{30}\}$ addition to $Y(OAc)_3$ solution in 0.05 M $KOAc_{(aq)}$ (pH = 5.6). The IR spectrum of the precipitate shows characteristic peaks of $\{P_5W_{30}\}$ in 2000–1000 cm^{-1}, suggesting that the precipitate is result of aggregation between Y^{3+} and $\{P_5W_{30}\}$ due to strong ion pairing strength between two species.



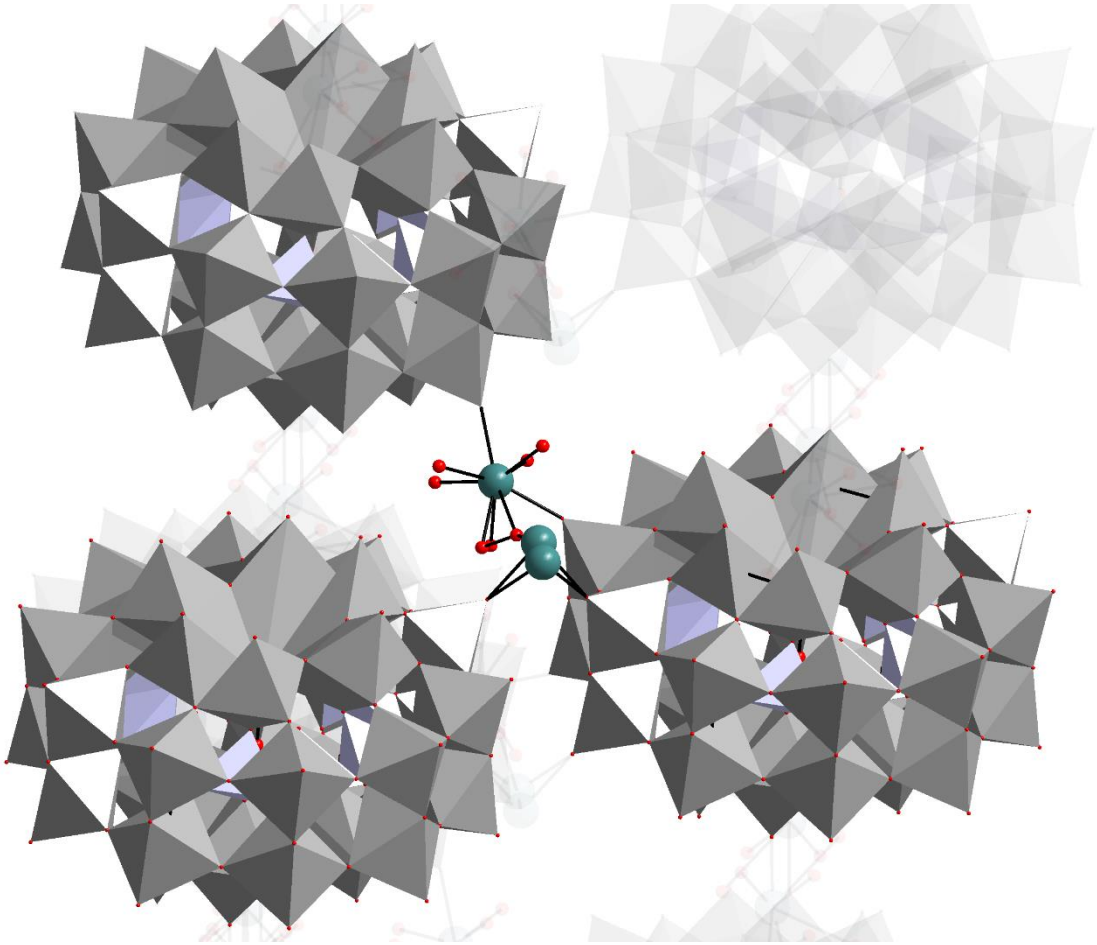
Supplemental Figure 3.11. Crystal structure of Y-{P_5W_{30}}.



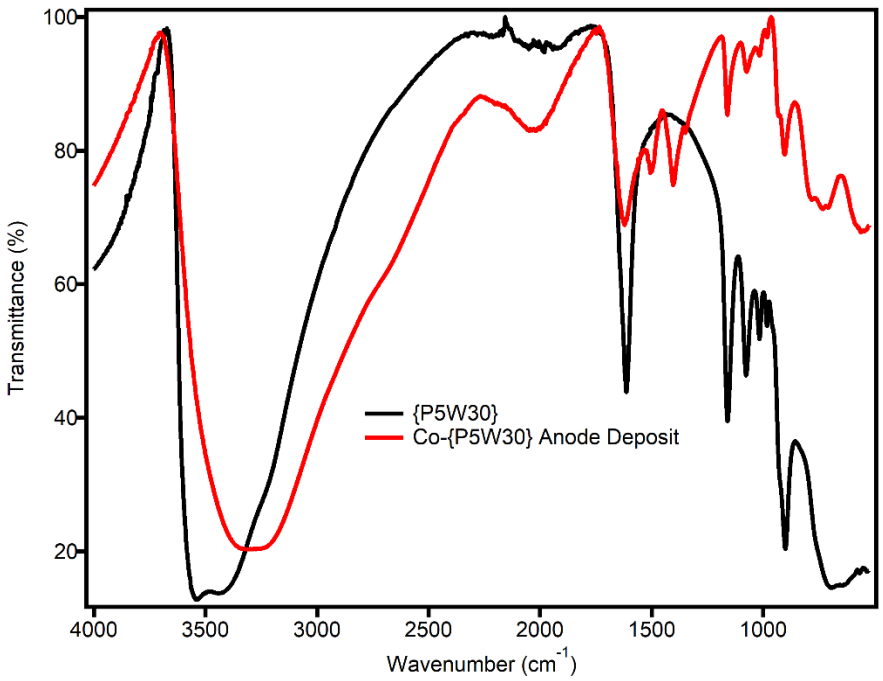
Supplemental Figure 3.12. Powder X-ray diffraction pattern of (i) Y-{P_5W_{30}} and (ii) simulated powder patten from Y-{P_5W_{30}} single-crystal X-ray diffraction data.



Supplemental Figure 3.13. Representation of O_{cap1}–Y–Y–O_{cap2} conncections in Y-{P_5W_{30}} crystal structure.



Supplemental Figure 3.14. Representation of O_{belt}–Y connections in Y-{P_5W_{30}} crystal structure.



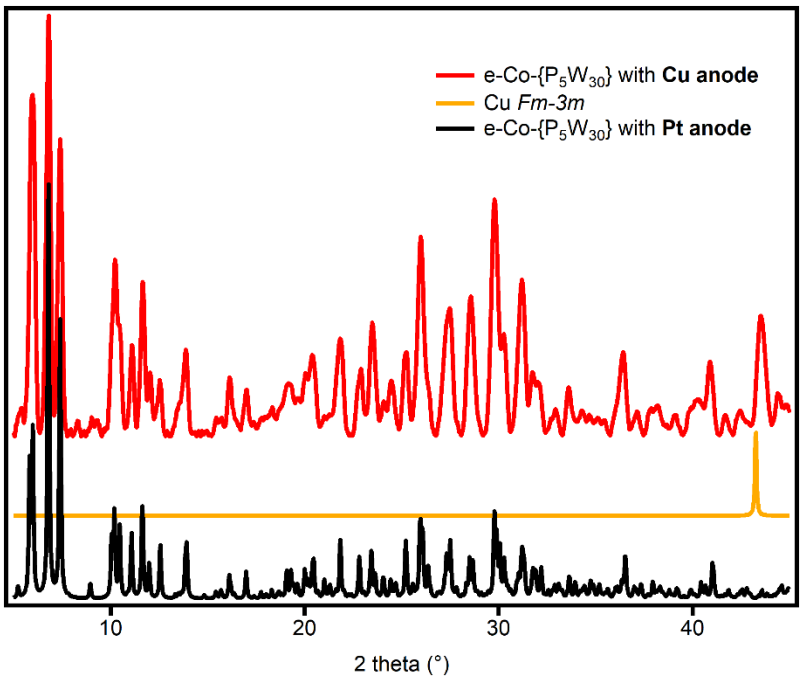
Supplemental Figure 3.15. FT-IR spectra of (i) anodic deposit during Co-{P_5W_{30}} synthesis and (ii) {P_5W_{30}}. The IR spectrum of deposit shows characteristic P–O stretches of {P_5W_{30}}, supporting{P_5W_{30}} incorporation in anodic byproduct.

Supplemental Table 3.7. Enegy-dispersive X-ray spectroscopy data of anodic product of undivided cell Co-{P_5W_{30}} synthesis with platinum wire anode.

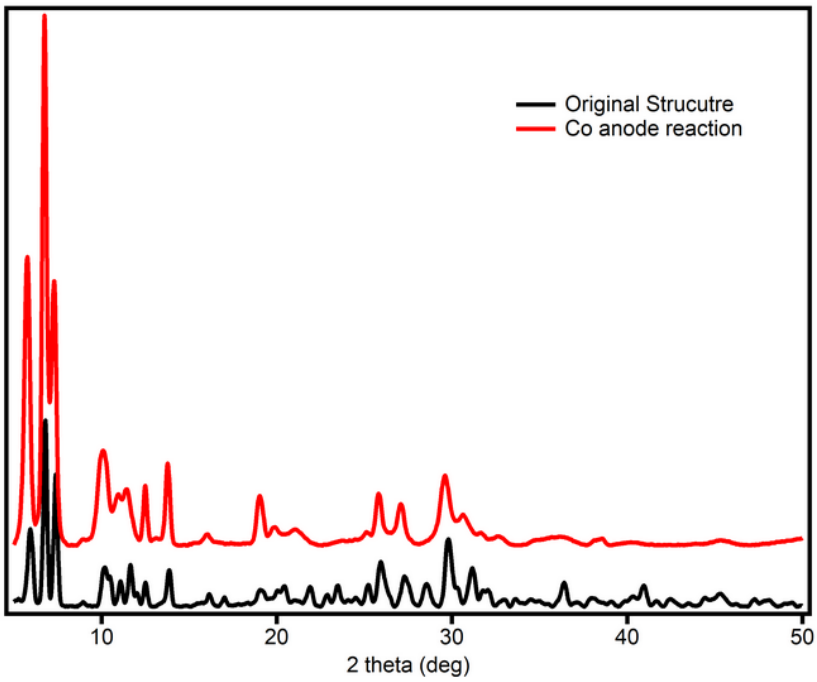
Element Line	Net Counts	Int. Cps/nA	Weight %	Weight % Error	Atom %	Atom % Error
C K	14084	469.47	16.8	± 0.2	31.6	± 0.3
O K	30022	1000.7	39.3	± 0.4	55.3	± 0.6
P K	1574	52.47	0.5	± 0.1	0.4	± 0.1
Co K	29129	970.97	28.7	± 0.4	11.0	± 0.1
W L	5346	178.20	14.6	± 0.9	1.8	± 0.1
Total			100.0		100.0	

Element Line	Net Counts	Int. Cps/nA	Weight %	Weight % Error	Atom %	Atom % Error
C K	1586	52.87	3.1	± 0.1	8.2	± 0.2
O K	20763	692.10	31.9	± 0.4	64.1	± 0.7
P K	1000	33.33	0.5	± 0.1	0.6	± 0.1
Co K	32827	1094.2	42.8	± 0.5	23.3	± 0.3
W L	5953	198.43	21.6	± 0.7	3.8	± 0.1
Total			100.0		100.0	

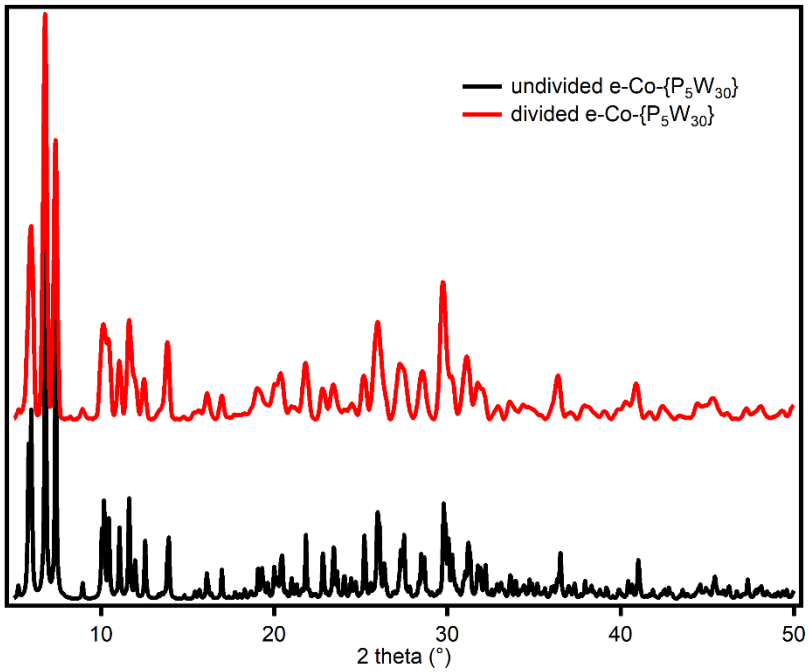
Element Line	Net Counts	Int. Cps/nA	Weight %	Weight % Error	Atom %	Atom % Error
C K	4855	161.83	7.0	± 0.1	16.8	± 0.3
O K	26777	892.57	34.1	± 0.4	61.2	± 0.7
P K	1772	59.07	0.7	± 0.1	0.7	± 0.1
Co K	35656	1188.5	36.8	± 0.4	18.0	± 0.2
W L	7442	248.07	21.3	± 1.0	3.3	± 0.2
Total			100.0		100.0	



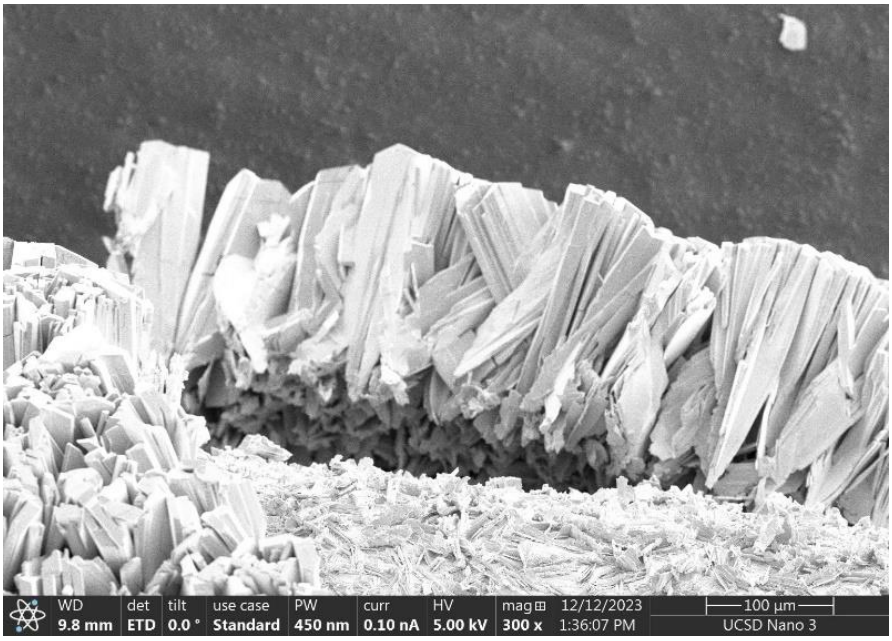
Supplemental Figure 3.16. Powder X-ray diffraction pattern of (i) cathodic product from undivided cell synthesis with copper sacrificial anode, compared to simulated powder patterns of (ii) Cu *Fm-3m* and (iii) crystal structure of Co-{P_5W_{30}}.



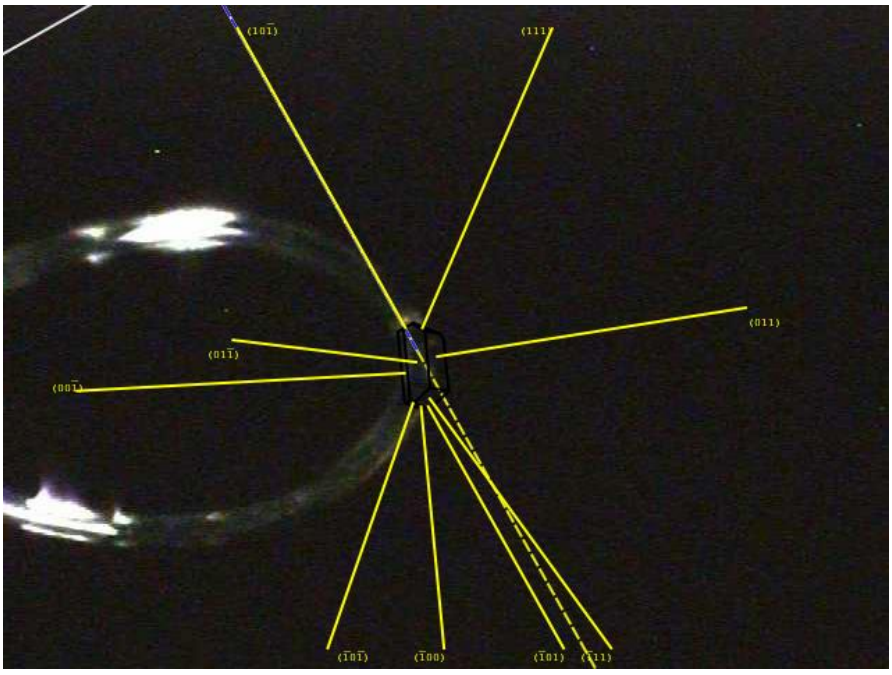
Supplemental Figure 3.17. Powder X-ray diffraction pattern of (i) cathodic product from undivided cell synthesis with cobalt wire sacrificial anode, compared to (ii) simulated powder pattern of crystal structure of Co-{P_5W_{30}}.



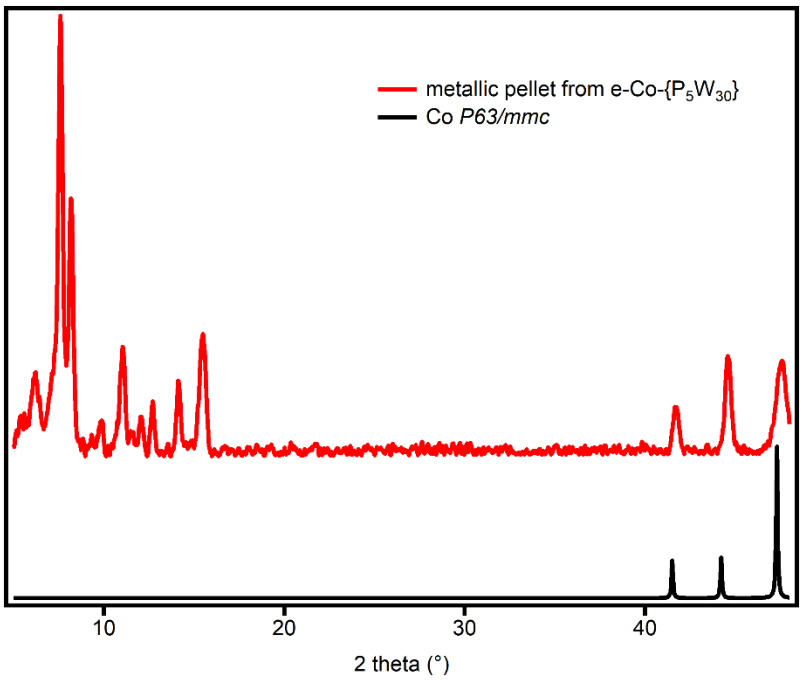
Supplemental Figure 3.18. Powder X-ray diffraction pattern of (i) cathodic product of **divided cell** synthesis with cobalt sacrificial anode, compared to (i) simulated powder pattern of Co-{P_5W_{30}} crystal structure.



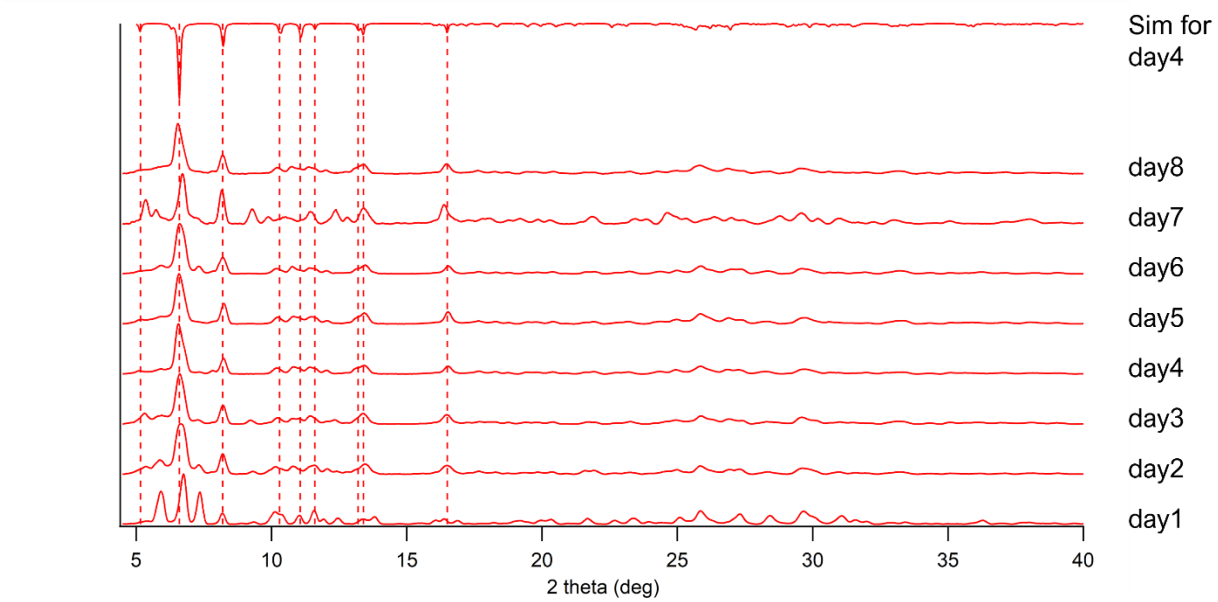
Supplemental Figure 3.19. Scanning electron microscopy image of electrosynthesized Co-{P_5W_{30}} crystals on cathode.



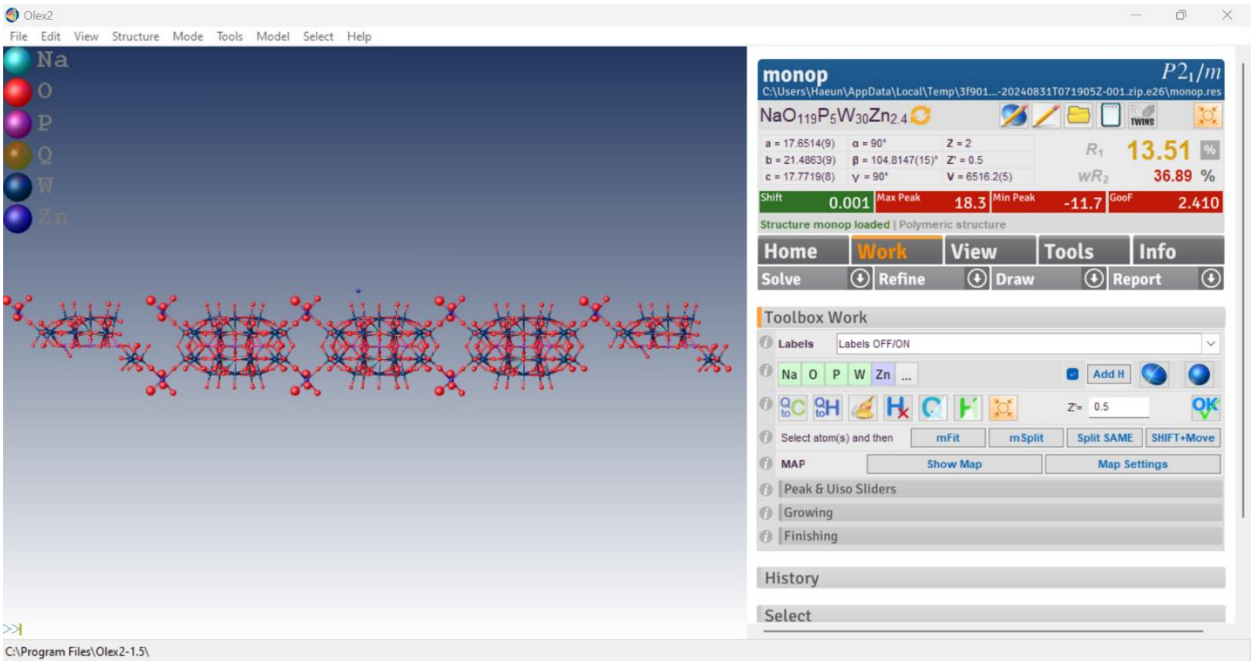
Supplemental Figure 3.20. Snapshot of video microscopy on Co-{P_5W_{30}} single-crystal.



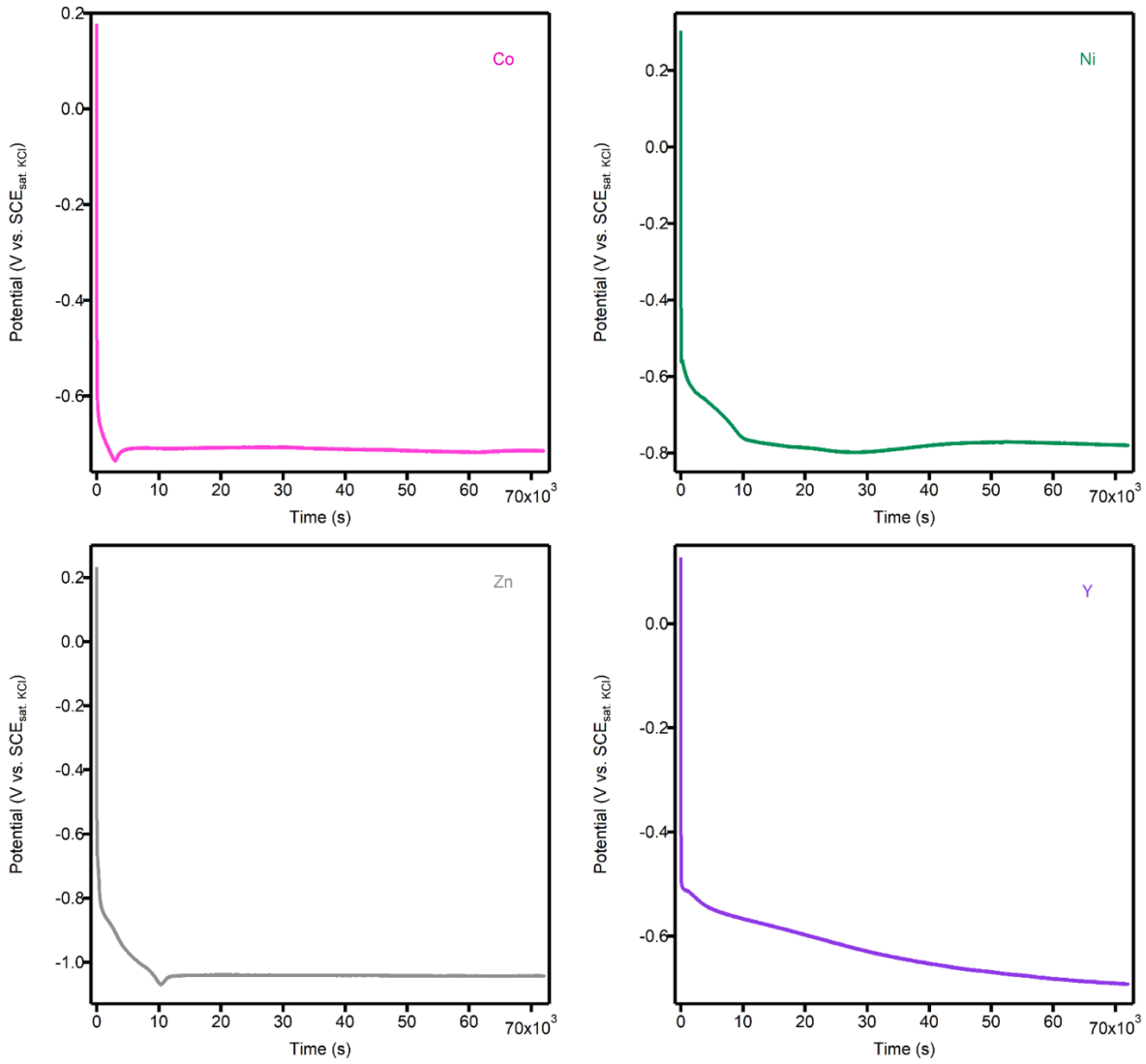
Supplemental Figure 3.21. Powder X-ray diffraction pattern of (i) metallic pellet isolated from cathodic surface after Co-{P5W30} synthesis, compared to (ii) simulated powder pattern of cobalt metal in P63/mmc space group.



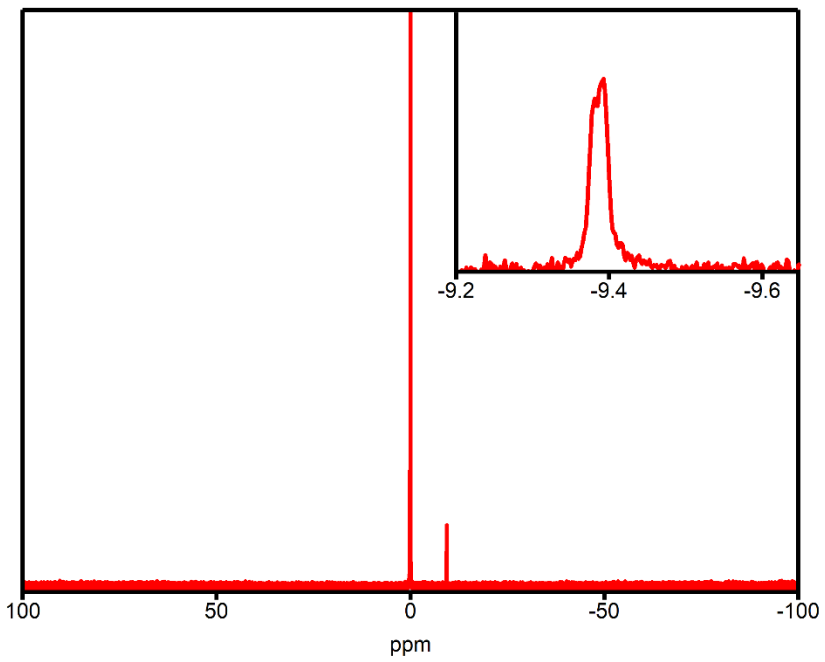
Supplemental Figure 3.22. Powder X-ray diffraction patterns of Zn-{P_5MoW_{29}} taken daily for 8 days since synthesis, compared to simulated powder pattern of preliminary crystal structure solved from day 4 sample. The network was exposed to air throughout the period.



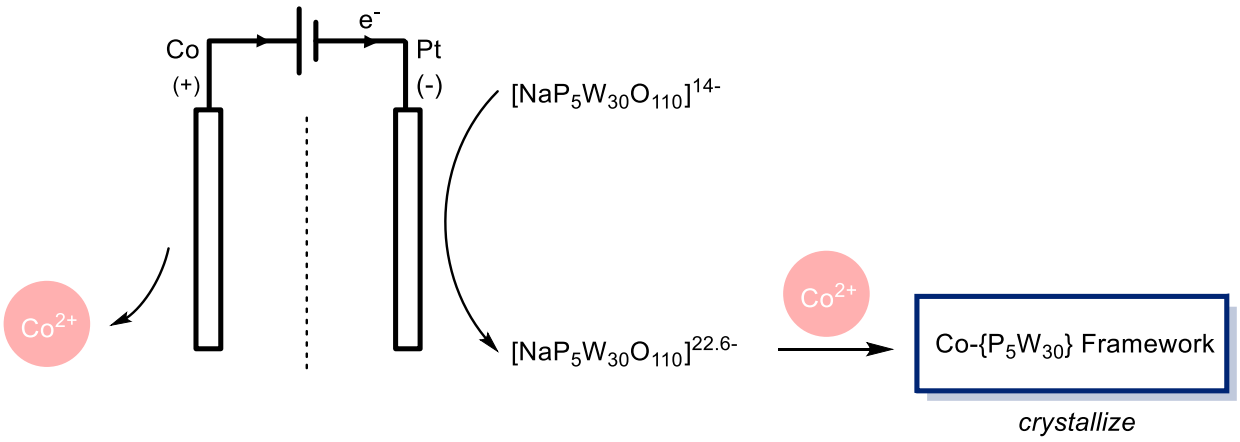
Supplemental Figure 3.23. Preliminary crystal structure solution of Zn-{P_5MoW_{29}} on day 4.



Supplemental Figure 3.24. Chronopotentiograms of (i) Co-{P_5W_{30}}, (ii) Ni-{P_5W_{30}}, (iii) Zn-{P_5W_{30}}, and (iv) Y-{P_5W_{30}}.



Supplemental Figure 3.25. ^{31}P NMR spectrum of {P_5W_{30}} used for electrocrystallization of coordination networks. The phosphorus peak around -9.4 ppm is consistent with literature reported value.[26]



Supplemental Figure 3.26. Scheme of Co-{P_5W_{30}} electrocrystallization in divided cell using sacrificial Co anode.

REFERENCES

(1) Litvinova, Y. M.; Gayfulin, Y. M.; Kovalenko, K. A.; Samsonenko, D. G.; van Leusen, J.; Korolkov, I. V.; Fedin, V. P.; Mironov, Y. V. Multifunctional Metal–Organic Frameworks Based on Redox-Active Rhenium Octahedral Clusters. *Inorg. Chem.* **2018**, *57* (4), 2072–2084. https://doi.org/10.1021/acs.inorgchem.7b02974.

(2) Gillen, J. H.; Moore, C. A.; Vuong, M.; Shajahan, J.; Anstey, M. R.; Alston, J. R.; Bejger, C. M. Synthesis and Disassembly of an Organometallic Polymer Comprising Redox-Active Co4S4 Clusters and Janus Biscarbene Linkers. *Chem. Commun.* **2022**, *58* (31), 4885–4888. https://doi.org/10.1039/D2CC00953F.

(3) Castleman, A. W.; Khanna, S. N. Clusters, Superatoms, and Building Blocks of New Materials. *J. Phys. Chem. C* **2009**, *113* (7), 2664–2675. https://doi.org/10.1021/jp806850h.

(4) Bartholomew, A. K.; Meirzadeh, E.; Stone, I. B.; Koay, C. S.; Nuckolls, C.; Steigerwald, M. L.; Crowther, A. C.; Roy, X. Superatom Regiochemistry Dictates the Assembly and Surface Reactivity of a Two-Dimensional Material. *J. Am. Chem. Soc.* **2022**, *144* (3), 1119–1124. https://doi.org/10.1021/jacs.1c12072.

(5) Horwitz, N. E.; Xie, J.; Filatov, A. S.; Papoular, R. J.; Shepard, W. E.; Zee, D. Z.; Grahn, M. P.; Gilder, C.; Anderson, J. S. Redox-Active 1D Coordination Polymers of Iron–Sulfur Clusters. *J. Am. Chem. Soc.* **2019**, *141* (9), 3940–3951. https://doi.org/10.1021/jacs.8b12339.

(6) Yaghi, O. M.; Sun, Z.; Richardson, D. A.; Groy, T. L. Directed Transformation of Molecules to Solids: Synthesis of a Microporous Sulfide from Molecular Germanium Sulfide Cages. *J. Am. Chem. Soc.* **1994**, *116* (2), 807–808. https://doi.org/10.1021/ja00081a067.

(7) Zheng, Z.; Long, J. R.; Holm, R. H. A Basis Set of Re6Se8 Cluster Building Blocks and Demonstration of Their Linking Capability: Directed Synthesis of an Re12Se16 Dicluster. *J. Am. Chem. Soc.* **1997**, *119* (9), 2163–2171. https://doi.org/10.1021/ja9638519.

(8) Vilà-Nadal, L.; Cronin, L. Design and Synthesis of Polyoxometalate-Framework Materials from Cluster Precursors. *Nat Rev Mater* **2017**, *2* (10), 17054. https://doi.org/10.1038/natrevmats.2017.54.

(9) Miras, H. N.; Vilà-Nadal, L.; Cronin, L. Polyoxometalate Based Open-Frameworks (POM-OFs). *Chem. Soc. Rev.* **2014**, *43* (16), 5679–5699. https://doi.org/10.1039/C4CS00097H.

(10) Kong, X.-J.; Ren, Y.-P.; Zheng, P.-Q.; Long, Y.-X.; Long, L.-S.; Huang, R.-B.; Zheng, L.-S. Construction of Polyoxometalates-Based Coordination Polymers through Direct Incorporation between Polyoxometalates and the Voids in a 2D Network. *Inorg. Chem.* **2006**, *45* (26), 10702–10711. https://doi.org/10.1021/ic061664y.

(11) Turo, M. J.; Chen, L.; Moore, C. E.; Schimpf, A. M. Co2+-Linked [NaP5W30O110]14−: A Redox-Active Metal Oxide Framework with High Electron Density. *J. Am. Chem. Soc.* **2019**, 5.

(12) Chen, L.; San, K. A.; Turo, M. J.; Gembicky, M.; Fereidouni, S.; Kalaj, M.; Schimpf, A. M. Tunable Metal Oxide Frameworks via Coordination Assembly of Preyssler-Type Molecular Clusters. *J. Am. Chem. Soc.* **2019**, *141* (51), 20261–20268. https://doi.org/10.1021/jacs.9b10277.

(13) Champsaur, A. M.; Yu, J.; Roy, X.; Paley, D. W.; Steigerwald, M. L.; Nuckolls, C.; Bejger, C. M. Two-Dimensional Nanosheets from Redox-Active Superatoms. *ACS Cent. Sci.* **2017**, *3* (9), 1050–1055. https://doi.org/10.1021/acscentsci.7b00328.

(14) Kawai, S.; Kher-Elden, M. A.; Sadeghi, A.; Abd El-Fattah, Z. M.; Sun, K.; Izumi, S.; Minakata, S.; Takeda, Y.; Lobo-Checa, J. Near Fermi Superatom State Stabilized by Surface State Resonances in a Multiporous Molecular Network. *Nano Lett.* **2021**, *21* (15), 6456–6462. https://doi.org/10.1021/acs.nanolett.1c01200.

(15) He, W.-W.; Li, S.-L.; Zang, H.-Y.; Yang, G.-S.; Zhang, S.-R.; Su, Z.-M.; Lan, Y.-Q. Entangled Structures in Polyoxometalate-Based Coordination Polymers. *Coordination Chemistry Reviews* **2014**, *279*, 141–160. https://doi.org/10.1016/j.ccr.2014.03.022.

(16) Liu, Q.; Wang, X. Polyoxometalate Clusters: Sub-Nanometer Building Blocks for Construction of Advanced Materials. *Matter* **2020**, *2* (4), 816–841. https://doi.org/10.1016/j.matt.2020.01.020.

(17) Li, D.; Ma, P.; Niu, J.; Wang, J. Recent Advances in Transition-Metal-Containing Keggin-Type Polyoxometalate-Based Coordination Polymers. *Coordination Chemistry Reviews* **2019**, *392*, 49–80. https://doi.org/10.1016/j.ccr.2019.04.008.

(18) Boyd, T.; Mitchell, S. G.; Gabb, D.; Long, D.-L.; Song, Y.-F.; Cronin, L. POMzites: A Family of Zeolitic Polyoxometalate Frameworks from a Minimal Building Block Library. *J. Am. Chem. Soc.* **2017**, *139* (16), 5930–5938. https://doi.org/10.1021/jacs.7b01807.

(19) Pope, M. T.; Müller, A. Polyoxometalate Chemistry: An Old Field with New Dimensions in Several Disciplines. *Angewandte Chemie International Edition in English* **1991**, *30* (1), 34–48. https://doi.org/10.1002/anie.199100341.

(20) Batail, P.; Boubekeur, K.; Fourmigué, M.; Gabriel, J.-C. P. Electrocrystallization, an Invaluable Tool for the Construction of Ordered, Electroactive Molecular Solids. *Chem. Mater.* **1998**, *10* (10), 3005–3015. https://doi.org/10.1021/cm980538s.

(21) Blue crystals were observed upon electrolysis of 788 μM {P5W30} solution prepared in 0.05 M KOAc buffer (pH = 5.6).

(22) Suzuki, K.; Sugawa, M.; Kikukawa, Y.; Kamata, K.; Yamaguchi, K.; Mizuno, N. Strategic Design and Refinement of Lewis Acid–Base Catalysis by Rare-Earth-Metal-Containing Polyoxometalates. *Inorg. Chem.* **2012**, *51* (12), 6953–6961. https://doi.org/10.1021/ic3008365.

(23) Kikukawa, Y.; Suzuki, K.; Sugawa, M.; Hirano, T.; Kamata, K.; Yamaguchi, K.; Mizuno, N. Cyanosilylation of Carbonyl Compounds with Trimethylsilyl Cyanide Catalyzed by an Yttrium-Pillared Silicotungstate Dimer. *Angewandte Chemie International Edition* **2012**, *51* (15), 3686–3690. https://doi.org/10.1002/anie.201200486.

(24) Zhang, Q.; Ondus, J.; Sheriff, K.; Mills, J.; Bahadori, A.; Smith, J.; Hwu, S.-J. Electrochemical Synthesis of Decavanadates-Containing Inorganic Complex and Inorganic-Organic Hybrid in Aqueous Solutions. *Polyhedron* **2021**, *209*, 115459. https://doi.org/10.1016/j.poly.2021.115459.

(25) Zhang, Q.; Ondus, J.; Mills, J.; Bahadori, A.; Smith, J.; Jordan, T.; Xu, H.; Hwu, S.-J. Bench-Top Electrochemical Crystal Growth of POMOFs: In-Situ Synthesis of New Organic-Inorganic Hybrids Containing [V10O28](6+n)− Polyoxovanadate. *Journal of Solid State Chemistry* **2020**, *287*, 121368. https://doi.org/10.1016/j.jssc.2020.121368.

(26) Creaser, I.; Heckel, M. C.; Neitz, R. J.; Pope, M. T. Rigid Nonlabile Polyoxometalate Cryptates [ZP5W30O110](15-n)- That Exhibit Unprecedented Selectivity for Certain Lanthanide and Other Multivalent Cations. *Inorg. Chem.* **1993**, *32* (9), 1573–1578. https://doi.org/10.1021/ic00061a010.

(27) Pope, M. T.; Varga, G. M. Jr. Heteropoly Blues. I. Reduction Stoichiometries and Reduction Potentials of Some 12-Tungstates. *Inorg. Chem.* **1966**, *5* (7), 1249–1254. https://doi.org/10.1021/ic50041a038.

(28) Pope, M. T.; Papaconstantinou, E. Heteropoly Blues. II. Reduction of 2:18-Tungstates. *Inorg. Chem.* **1967**, *6* (6), 1147–1152. https://doi.org/10.1021/ic50052a018.

(29) Fernández, J. A.; López, X.; Bo, C.; de Graaf, C.; Baerends, E. J.; Poblet, J. M. Polyoxometalates with Internal Cavities: Redox Activity, Basicity, and Cation Encapsulation in [Xn+P5W30O110](15-n)- Preyssler Complexes, with X = Na+, Ca2+, Y3+, La3+, Ce3+, and Th4+. *J. Am. Chem. Soc.* **2007**, *129* (40), 12244–12253. https://doi.org/10.1021/ja0737321.

(30) Buzko, V. Yu.; Sukhno, I. V.; Polushin, A. A.; Panyushkin, V. T. DFT Study of the Structural Characteristics of the Yttrium(3+) Aqua Ion. *J Struct Chem* **2006**, *47* (3), 413–419. https://doi.org/10.1007/s10947-006-0316-6.

(31) Chen, L.; Turo, M. J.; Gembicky, M.; Reinicke, R. A.; Schimpf, A. M. Cation-Controlled Assembly of Polyoxotungstate-Based Coordination Networks. *Angewandte Chemie International Edition* **2020**, *59* (38), 16609–16615. https://doi.org/10.1002/anie.202005627.

(32) Moeller, T.; Martin, D. F.; Thompson, L. C.; Ferrús, R.; Feistel, G. R.; Randall, W. J. The Coordination Chemistry of Yttrium and the Rare Earth Metal Ions. *Chem. Rev.* **1965**, *65* (1), 1–50. https://doi.org/10.1021/cr60233a001.

(33) Chen, L. Tunable Transition-Metal-Linked Preyssler Type Polyoxometalate Frameworks: Synthesis, Structural Characterization and Optical Proprieties, UC San Diego, 2018. https://escholarship.org/uc/item/40g2q69v (accessed 2024-08-30).

(34) Sheldrick, G. M. SHELXT – Integrated Space-Group and Crystal-Structure Determination. *Acta Cryst A* **2015**, *71* (1), 3–8. https://doi.org/10.1107/S2053273314026370.

(35) Sheldrick, G. M. Crystal Structure Refinement with SHELXL. *Acta Cryst C* **2015**, *71* (1), 3–8. https://doi.org/10.1107/S2053229614024218.

(36) Dolomanov, O. V.; Bourhis, L. J.; Gildea, R. J.; Howard, J. a. K.; Puschmann, H. OLEX2: A Complete Structure Solution, Refinement and Analysis Program. *J Appl Cryst* **2009**, *42* (2), 339–341. https://doi.org/10.1107/S0021889808042726.

(37) Hayashi, A.; Haioka, T.; Takahashi, K.; Bassil, B. S.; Kortz, U.; Sano, T.; Sadakane, M. Cation Effect on Formation of Preyssler-Type 30-Tungsto-5-Phosphate: Enhanced Yield of Na-Encapsulated Derivative and Direct Synthesis of Ca- and Bi-Encapsulated Derivatives. *Zeitschrift für anorganische und allgemeine Chemie* **2015**, *641* (15), 2670–2676. https://doi.org/10.1002/zaac.201500679.

(38) Takahashi, K.; Sano, T.; Sadakane, M. Preparation and Characterization of Preyssler-Type Phosphotungstic Acid, H15–n[P5W30O110Mn+], with Different Encapsulated Cations (M = Na, Ca, Bi, Eu, Y, or Ce), and Their Thermal Stability and Acid Catalyst Properties. *Zeitschrift für anorganische und allgemeine Chemie* **2014**, *640* (7), 1314–1321. https://doi.org/10.1002/zaac.201400038.

Chapter 4 Polyoxometalates as Thermogalvanic Electrolytes

4.1 Introduction

Over 60% of energy generated from primary resources is wasted as heat, with low-temperature grade heat (< 200 °C) constituting about 66% of this waste.[1] Given the substantial amount of energy lost in this form, it is essential to explore methods for capturing low-grade heat, which is particularly advantageous due to its milder conditions compared to mid- or high-temperature grades, yet it remains sufficient to facilitate various chemical reactions.

Thermogalvanic cells have emerged as a promising solution for low-grade thermal energy utilization. These cells operate by using the temperature gradient between the electrodes to generate cell potentials. The differing temperatures result in different chemical equilibrium states at each electrode. As the system seeks to reach homogenous equilibrium between the electrodes, this process translates into an electromotive force, achieving thermal energy conversion to electrical potential energy.

An essential metric for evaluating the performance of a thermogalvanic cell is the Seebeck coeffficent (S_e), which represents the thermogalvanic cell potential induced in a material as a function of temperature gradient. By using the relationship between free energy (ΔG) and the change in entropy (ΔS) and cell potential (E or V), S_e can be expressed as the equation 4.1,[2] where n is the number of electrons involved in the redox process and F is Faraday's constant.

$$S_e = \partial V/\partial T = \Delta S/nF \qquad (4.1)$$

Coupled with the correlationship (equation 4.2) derived from simplified Born model by Sahami and Weaver,[3] where Z is charge number and r is effective solvation radius, the overall relationship of S_e with Z, n, and r can be represented by equation 4.3. This relationship provides an important insight into designing thermogalvanic cells with high S_e.[4]

$$\Delta S_{rc} \propto {(Z_{ox}^2 - Z_{red}^2)}/{r} \qquad (4.2)$$

$$nFS_e \propto {(Z_{ox}^2 - Z_{red}^2)}/{r} \qquad (4.3)$$

Solution-phase thermogalvanic cells have garnered attention as many systems were able to achieve S_e on the order of mV/K utilizing redox-active electrolytes.[5,6] Polyoxometalates (POMs) are promising as such electrolytes, owing to their structural diversity and tunability, solubility, and rich redox features.[7–9] Especially in relation to equation 4.2, their large negative charges could directly contribute to a high S_e.[4] Indeed, Wang *et al.* recently reported a solution-phase photo-thermogalvanic cell with polyoxovanadate compound {[Ni-(1,10-phenanthrolilne)$_3$][$V_{13}O_{34}$Cl]Cl} as the near-infrared radiation absorbing electrolyte, reaching a large S_e of 6.38 mV/K and an optimized thermal power of 1.2 W/m^2.[10] Despite these exciting results and potential, POMs have not been widely explored as thermogalvanic cell electrolytes, leaving significant opportunities for further research.[4] In this chapter, various POM thermogalvanic systems will be discussed, including the Wells–Dawson cluster, α-$K_6[P_2W_{18}O_{62}]$,[4] and Preyssler-type clusters, $K_{14}[NaP_5W_{30}O_{110}]$ and $H_{3.5}Na_{2.5}K_8[NaP_5MoW_{29}O_{110}]$.

4.2 Results and Discussion

{P_2W_{18}} was synthesized following a literature procedure.[11] Briefly, to an aqueous solution of sodium tungstate dihydrate (Na_2WO_4•$2H_2O$, 150.0 g, 0.46 mol), 4 M hydrochloric

acid (HCl, 125 ml, 0.50 mol) was added dropwise, followed by a slow addition of 4 M phosphoric acid (H_3PO_4, 125 ml, 0.50 mol). The final solution was refluxed for 24 h, then cooled to room-temperature. Potassium chloride (KCl, 75.0 g, 1.01 mol) was subsequently added to the solution to isolate the product through precipitation. Recrystallization of the precipitate in hot deionized (DI) water resulted in yellow crystals of the α-isomer of $\{P_2W_{18}\}$. Nuclear magnetic resonance (NMR) and infrared (IR) spectroscopies confirmed the identity and purity of the product.[4]

$\{P_5W_{30}\}$ was also prepared following a reported procedure.[12,13] Briefly, a solution of $Na_2WO_4 \bullet 2H_2O$ (29.7 g, 90.0 mmol), NaCl (3.51 g, 60.0 mmol), DI water (27.0 ml) and 85% H_3PO_4 (21.0 ml) was heated overnight at 125 °C. The product was collected by precipitation with KCl (9.00 g, 0.120 mol) after cooling. The precipitate was recrystallized several times in hot water to isolate pure $\{P_5W_{30}\}$, which was confirmed by NMR (**Supplemental Figure 4.2)** and IR (**Supplemental Figure 4.3**) spectroscopies. Further synthetic details are provided in Chapter 2.

To gain insights into the thermoelectric properties of $\{P_2W_{18}\}$ and $\{P_5W_{30}\}$, variable-temperature cyclic voltammetry (VTCV) was conducted on aqueous solutions of these clusters under various conditions following the recently reported apporoach.[4] Redox processes are numbered sequentially from 1 to 4 for $\{P_2W_{18}\}$ (**Figure 4.1)** and 1 to 3 for $\{P_5W_{30}\}$, starting with the process that occurs at the highest potential. Cathodic peak potentials (E_c) and anodic peak potentials (E_a) of each redox process were extracted from the voltammograms by averaging the potentials at which the derivative changed from positive to negative. The half-wave potential ($E_{1/2}$) was calculated as the midpoint between E_c and E_a. These three values were each plotted as a function of T and fit to a line. Although S_e is defined for full-cell potentials induced by

temperature gradients, the slope of $E_{1/2}$ *vs T*, which is equivalent for $\Delta V/\Delta T$, where *V* is $E_{1/2}$, was approximated as S_e of a redox process.[4] Corresponding ΔS_{rc} of redox processes were calculated using equation 4.1.

CVs on a 1 mM $\{P_2W_{18}\}$ solution prepared in 0.1 M sodium acetate buffer at a pH of 3.5 showed that the cluster undergoes four separate redox processes (**Figure 4.1)**. The cluster is reduced by a total of six electrons through these processes, reaching a charge of −12, consistent with previous reports.[14] The first two processes each involve one-electron reductions, while the latter two processes each involve two-electron reductions. $\{P_2W_{18}\}$ was tested for thermal stability by collecting a CV at 2 °C, heating the solution to 49.0 °C and collecting a CV, and cooling back to 2.0 °C and collecting another CV (**Supplemental Figure 4.4**). The redox features of $\{P_2W_{18}\}$ were recovered, confirming the structural integrity suitable for VTCV in this temperature range. VTCV on this solution (**Supplemental Figure 4.5)** revealed S_e values of −1.34, −1.64, −1.35, and −1.37 mV/K (**Supplemental Figure 4.6**), with the second redox process having the largest S_e. To consider the number of charge carriers in each process, ΔS_{rc} was calculated using equation 4.1 and was plotted against $Z_{ox}^2 - Z_{red}^2$ (**Supplemental Figure 4.7**). Given that the solvation-shell volume calculated through molecular dynamics (MD) changed by only 1.5% between the 6− and 7− redox states of $\{P_2W_{18}\}$, it was assumed that the effective radius remains essentially constant throughout the redox events.[4] Consequently, the strong linear correlation between ΔS_{rc} and $Z_{ox}^2 - Z_{red}^2$ is as expected according to equation 4.2, as in $\{P_2W_{18}\}$ redox reported at pH 3.40.[4]

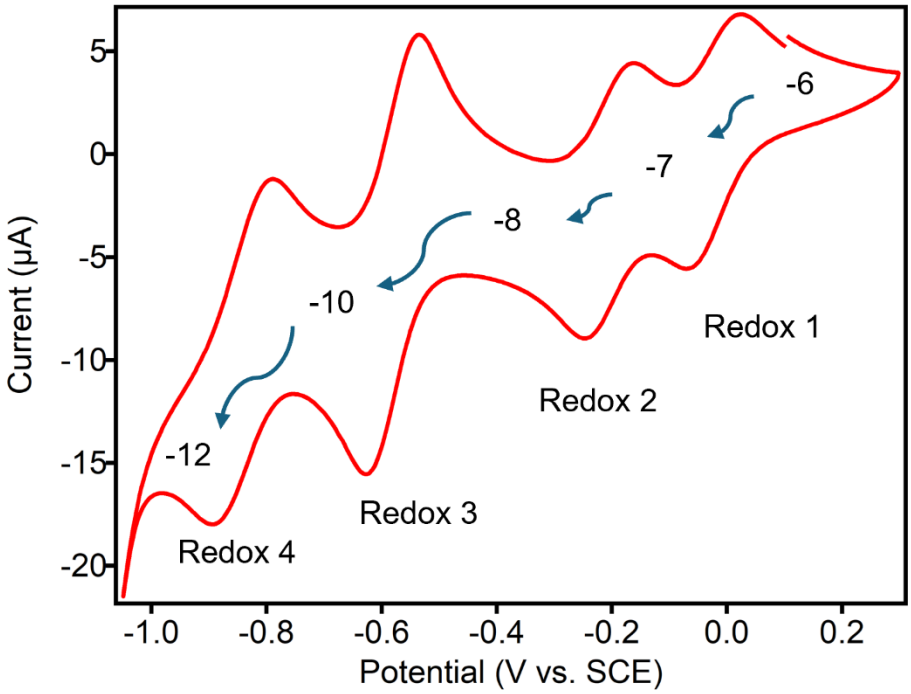


Figure 4.1. Cyclic voltammogram of 1 mM $\{P_2W_{18}\}$ in 0.1 M sodium acetate (pH = 3.5) measured at 21.5 °C.

To study the effect of pH on the S_e values of the $\{P_2W_{18}\}$ redox processes, VTCV data were collected on a $\{P_2W_{18}\}$ solution with a higher pH (1 mM in 0.1 M sodium acetate buffer at pH 5.9; **Supplemental Figure 4.8**). Notably, at this pH, the third two-electron redox process observed at pH 3.5 splits into two single-electron processes, indicated as process 3a and 3b. The S_e values of the redox processes 1 and 2 at pH 5.9 were comparable to those corresponding at pH 3.5. The S_e values, however, were larger than at pH 3.5 for redox processes 3a, 3b, and 4 (**Supplemental Figure 4.9**). They were calculated to be −1.80, −1.45, and −1.62 mV/K, respectively. Even considering the varied number of electrons involved in the third processes at different pH, the collective ΔS_{rc} magnitude of processes 3a and 3b at pH 5.9 is larger than that of process 3 at pH 3.5. At pH 5.9, ΔS_{rc} values are −174 J mol^{-1} K^{-1} for process 3a and −140 J mol^{-1} K^{-1} for process 3b, summing up to −314 J mol^{-1} K^{-1}. In contrast, the ΔS_{rc} of process 3 at pH 3.5

was −261 J mol^{-1} K^{-1}. Overall, the average values of S_e and total ΔS_{rc} of $\{P_2W_{18}\}$ were observed to be larger at higher pH. Additionally, while the anodic peak shift per temperature was greater than the cathodic peak shift at pH 3.5, the opposite trend was observed at pH 5.9, where the cathodic peak shift was greater than anodic peak shift.

For comparative analysis to $\{P_5W_{30}\}$ system (*vide infra*), additional VTCV on a 1 mM $\{P_2W_{18}\}$ solution prepared in aqueous 1 M HCl was conducted (**Supplemental Figure 4.10** and **Supplemental Figure 4.11**). The pH at this condition is 0.0, which is suitable for electrochemical studies of $\{P_2W_{18}\}$, as the cluster is stable below a pH of 6.[15] While the S_e value for redox process 1 was the highest at pH 0.0, calculated as −1.55 mV/K, the S_e values for redox processes 2, 3, and 4 were −1.13 mV/K, −0.561 mV/K, and −0.455 mV/K, respectively, all of which were lower than those at pH 3.5 and 5.9. Notably, $\{P_2W_{18}\}$ exhibited a different trend between ΔS_{rc} and $Z_{ox}^2 - Z_{red}^2$ at pH 0.0. The ΔS_{rc} values of each redox process of $\{P_2W_{18}\}$ were calculated to be −150 J mol^{-1} K^{-1}, −109 J mol^{-1} K^{-1}, −108 J mol^{-1} K^{-1}, and −87.8 J mol^{-1} K^{-1}, decreasing as the $Z_{ox}^2 - Z_{red}^2$ increased, which is opposite to the expected trend from equation 4.2. This deviation may be attributed to a potential significant increase in r during the later redox processes. Since the $\{P_2W_{18}\}$ redox is reported to be proton-coupled at low pH,[16] this increase of r could result from enhanced hydrogen bonding of water molecules to $\{P_2W_{18}\}$ as the cluster gets more reduced, and thus more protonated.

A different species of POM, specifically $\{P_5W_{30}\}$, was evaluated due to its −14 charge, and its ability to undergo ten electron reductions, potentially achieving larger $Z_{ox}^2 - Z_{red}^2$ values than $\{P_2W_{18}\}$. When VTCV was measured on a 1 mM $\{P_5W_{30}\}$ solution prepared in 0.1 M sodium acetate buffer at pH 5.5, a loss of redox features was observed,[4] possibly due to

precipitation of reduced $\{P_5W_{30}\}$ under these experimental conditions. Therefore, further $\{P_5W_{30}\}$ solutions were prepared in aqueous 1 M HCl to maximize the solubility.

CV scans of a 1 mM $\{P_5W_{30}\}$ solution prepared in 1 M HCl(aq) (**Supplemental Figure 4.12**) showed three redox features, identified as four-, four-, and two-electron processes.[9] VTCV results indicated that the third redox process was lost as the hydrogen evolution reaction (HER) potential shifted to less reducing values at higher temperatures.[17,18] The first two redox processes, however, remained quasi-reversible across the temperature range of 20.0 – 51.0 °C. Consequently, the utility of this system is limited to the redox processes 1 and 2, so the analysis was focused on the temperature-dependencies of these two processes.

The S_e values of redox processes 1 and 2 of $\{P_5W_{30}\}$ were calculated to be −0.343 mV/K and −0.393 mV/K , respectively (**Table 4.1** and **Supplemental Figure 4.13**), which are approximately one-fourth of the potential shift rate of $\{P_2W_{18}\}$ redox process 1 (−1.55 mV/K). The $Z_{ox}^2 - Z_{red}^2$ values for these $\{P_5W_{30}\}$ processes, however, are −128 and −160, which are significantly larger than the corresponding value for the first redox pair of $\{P_2W_{18}\}$, which is −13. To investigate this discrepancy, the ΔS_{rc} values for both data sets were calculated to account for different numbers of electrons involved in each species redox. The ΔS_{rc} values of $\{P_5W_{30}\}$ were calculated as −132 and −152 J mol^{-1} K^{-1} for redox processes 1 and 2, respectively. These values are comparable to the ΔS_{rc} of the $\{P_2W_{18}\}$ redox process 1, which is −150 J mol^{-1} K^{-1}. Although this indicates that the smaller S_e values of $\{P_5W_{30}\}$ are partly due to the higher number of electrons involved in its redox processes compared to $\{P_2W_{18}\}$ redox process 1 (four-electron vs. single-electron), the significant difference in $Z_{ox}^2 - Z_{red}^2$ values also suggests that the r of $\{P_5W_{30}\}$ could be much larger than that of $\{P_2W_{18}\}$.

Table 4.1. Charge square difference of redox couple ($Z_{ox}^2 - Z_{red}^2$), number of electrons transferred (n), approximate Seebeck coefficients (S_e), and calculated entropy change (ΔS_{rc}) for each redox process of 1 mM $\{P_5W_{30}\}$ and $\{P_2W_{18}\}$ in 1 M HCl(aq).

1 M HCl(aq)	1 mM $\{P_5W_{30}\}$		1 mM $\{P_2W_{18}\}$			
	Redox 1	Redox 2	Redox 1	Redox 2	Redox 3	Redox 4
$Z_{ox}^2 - Z_{red}^2$	−128	−160	−13	−15	−36	−44
n	4	4	1	1	2	2
S_e (mV K^{-1})	−0.343	−0.393	−1.55	−1.13	−0.561	−0.455
ΔS_{rc} (J K^{-1} mol^{-1})	−132	−152	−150	−109	−108	−87.8

As the parameter r appears to influence the S_e values, preliminary studies were conducted on ion-pair interactions and electronic structures that could potentially impact r. The effect of K^+ concentration on the S_e of $\{P_5W_{30}\}$ was evaluated by adding potassium chloride (KCl) to solutions of 1 mM $\{P_5W_{30}\}$ prepared in 1 M HCl(aq), achieving 50 mM and 100 mM KCl. It was predicted that an increase in $[K^+]$ would yield a monotonic decrease on the S_e values of $\{P_5W_{30}\}$ by increasing the effective hydrodynamic radius. This assumption is supported by the fact that K^+ displays high ion-pairing behavior with polyoxotungstates.[19,20] VTCV analysis (**Supplemental Figure 4.15** and **Supplemental Figure 4.17**) revealed that there was alteration in S_e values with the addition of KCl, but no clear trend was observed as a 46% decrease in S_e of the first redox process at 50 mM KCl was reversed to a 39% increase compared to the original S_e at 100 mM KCl. These preliminary results suggest that significantly high $[K^+]$ may lower the effective radius of the POM by disrupting the solvation sphere around it.[21,22]

The alteration of the electronic structure of $\{P_5W_{30}\}$ and its effect on S_e was assessed on a preliminary basis. $\{P_5W_{30}\}$ is known to have a generally delocalized lowest unoccupied molecular orbital (LUMO) across thirty W atoms.[23] This delocalization can be disrupted by doping $\{P_5W_{30}\}$ with a Mo atom, as Mo has more accessible *d*-orbital energies than W, causing the LUMO to localize around the Mo site.[24] By substituting 27 mmol of $Na_2WO_4 \bullet 2H_2O$ to 5 mmol of $Na_2MoO_4 \bullet 2H_2O$ and 25 mmol of to $Na_2WO_4 \bullet 2H_2O$ in the synthesis of $\{P_5W_{30}\}$, molybdenum-substituted Preyssler ($H_{3.5}Na_{2.5}K_8[NaP_5MoW_{29}O_{110}]$, denoted as $\{P_5MoW_{29}\}$) was synthesized. A single Mo is expected to be doped at a belt position of $\{P_5W_{30}\}$.[24] We hypothesized that the charge distribution impacts r, and that localization of the LUMO would decrease r of the cluster as the charge concentrates around the single Mo atom. Indeed, VTCV results (**Supplemental Figure 4.19** showed an increase in S_e, calculated to be -0.395 mV/K (**Supplemental Figure 4.19**). Further studies will include density-functional theory-based calculations on the LUMO and LUMO+1 of $\{P_5MoW_{29}\}$ and $\{P_5W_{30}\}$, as well as molecular dynamics (MD) calculations on the r of the -18 charge states of these clusters, to confirm the hypothesis.

The author would like to thank the collaborators Erik Svensson Grape, Jiawei Huang, Dwaipayan Roychowdhury, Tekalign T. Debela, Andrew Jenkins, Christopher H. Hendon, and Carl K. Brozek for collaborative work on the project[4] that provided a foundation for the studies presented in Chapter 4.

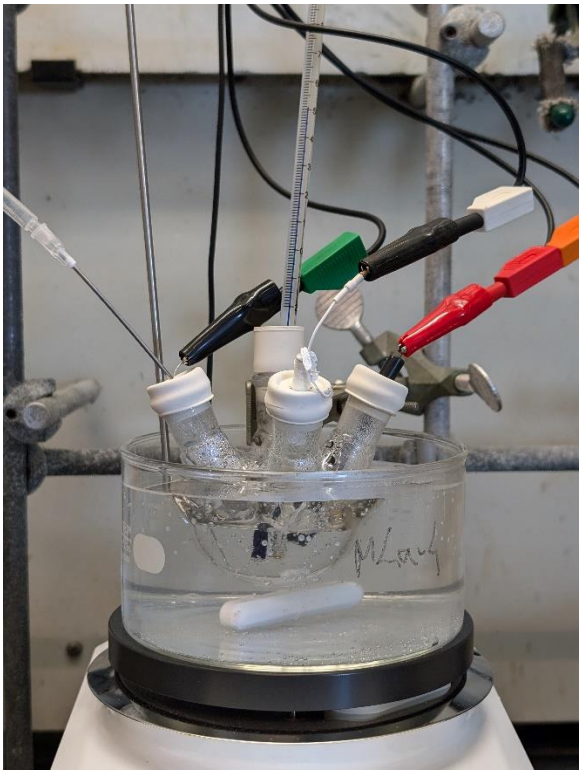
4.3 Supplemental Information

4.3.1 Experimental Details

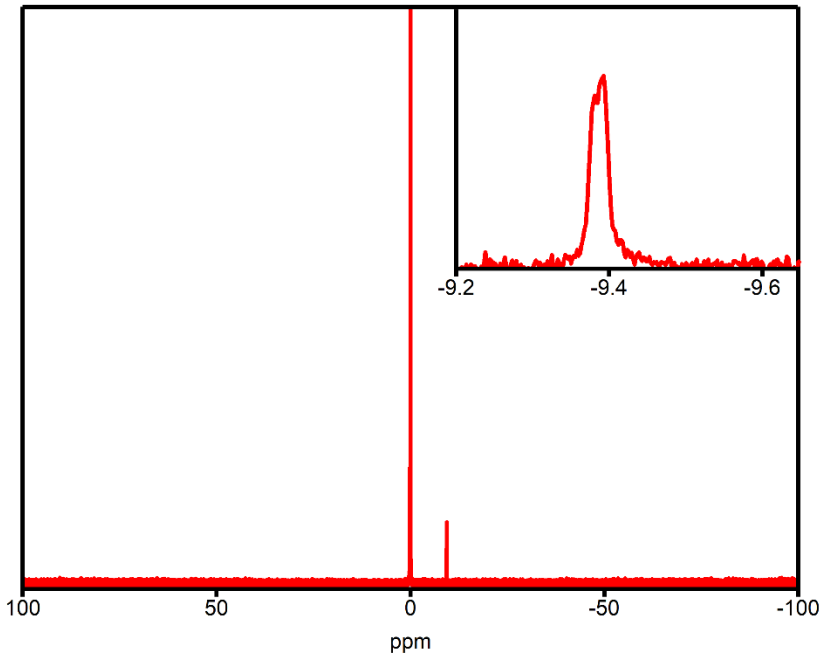
VTCV was measured using a three-electrode setup in a vessel with four ports. Three ports were occupied by electrodes and the fourth port by a thermometer. A glassy carbon electrode and a platinum wire served as working and counter electrodes, respectively. A

saturated calomel electrode (SCE) or a silver/silver chloride (Ag/AgCl) electrode in a 3 M sodium chloride solution was used as the reference. A picture of the typical setup can be found in **Supplemental Figure 4.1**. The VTCV data was collected in 2.0 – 49.0 °C temperature range with 10 °C intervals, or 20.0 – 50.0 °C with 5 °C intervals, approximately. Solutions were sparged with argon or nitrogen for 15 minutes before scans, and for 5 minutes in between the scans.

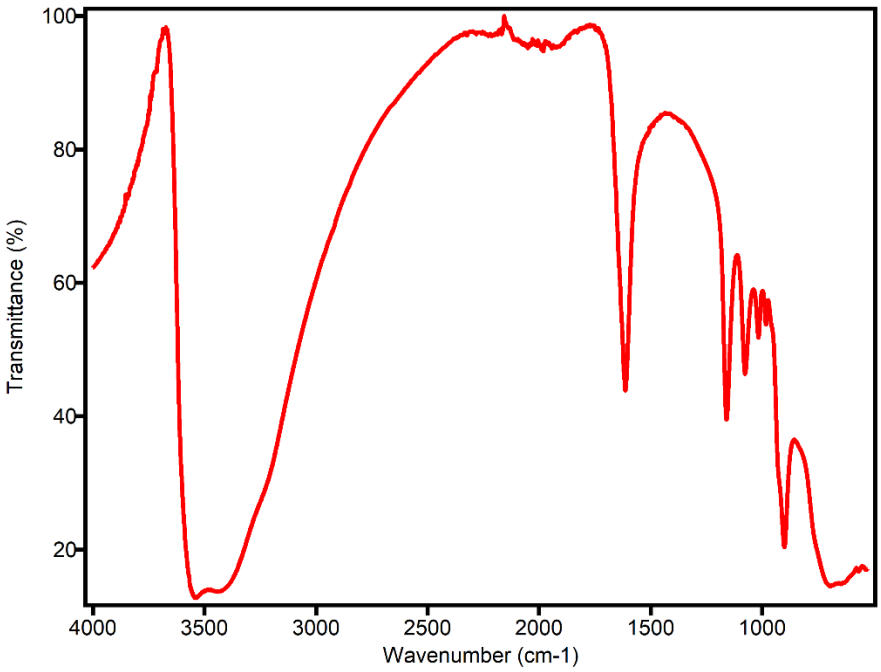
4.3.2 Appendix



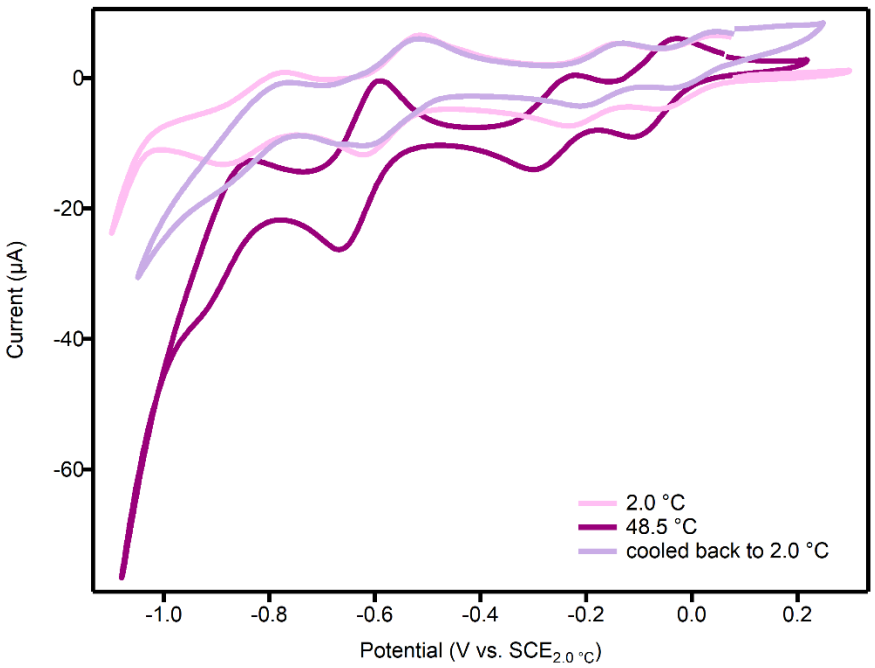
Supplemental Figure 4.1. A typical setup for VTCV experiment.



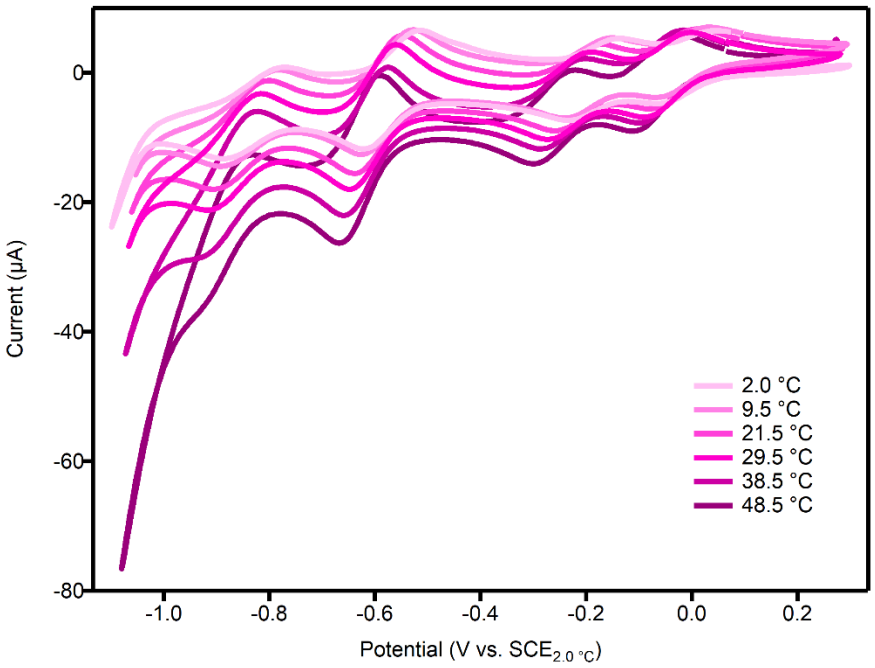
Supplemental Figure 4.2. ^{31}P NMR spectrum of $\{P_5W_{30}\}$ in H_2O.



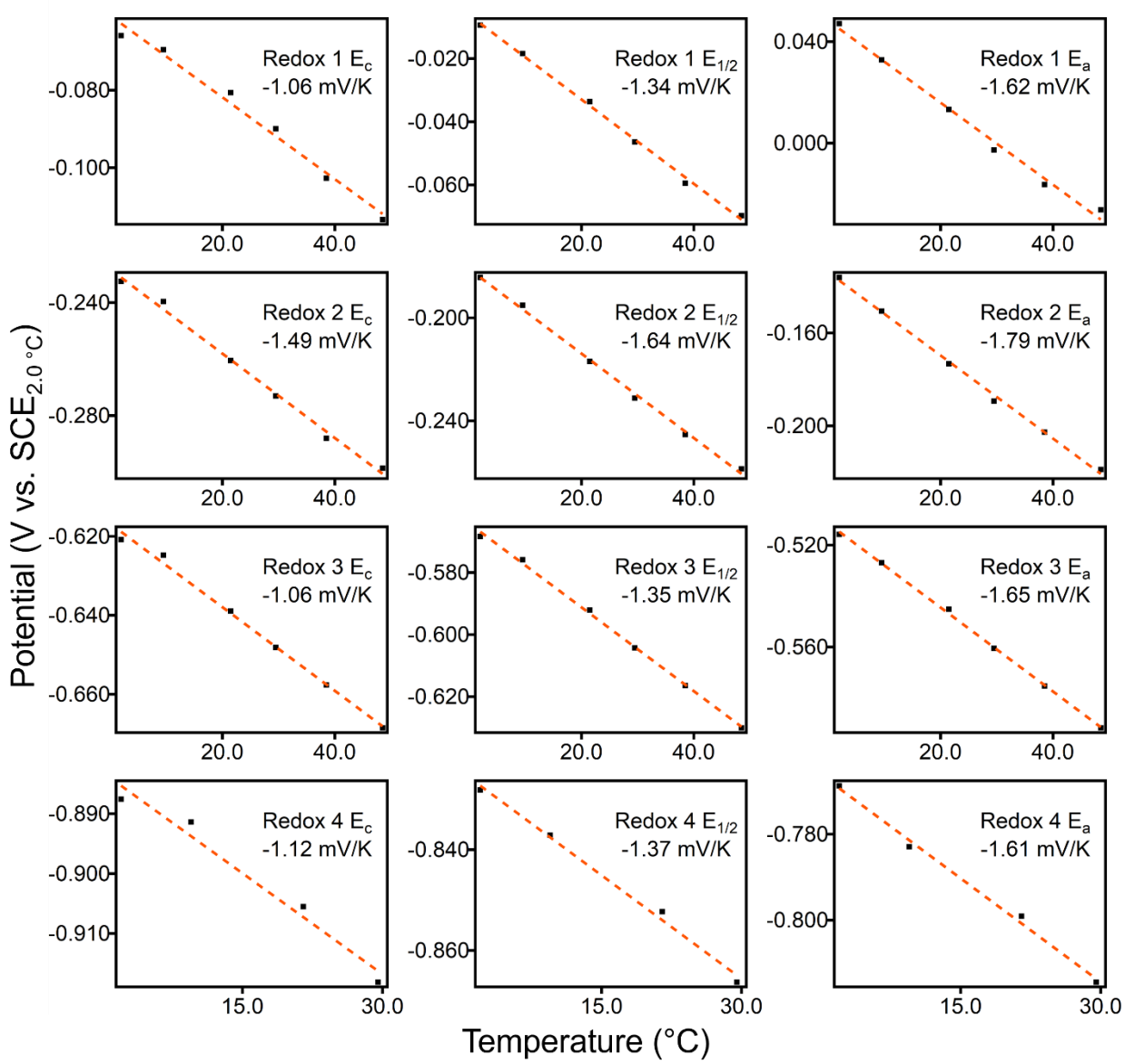
Supplemental Figure 4.3. IR spectrum of $\{P_5W_{30}\}$.



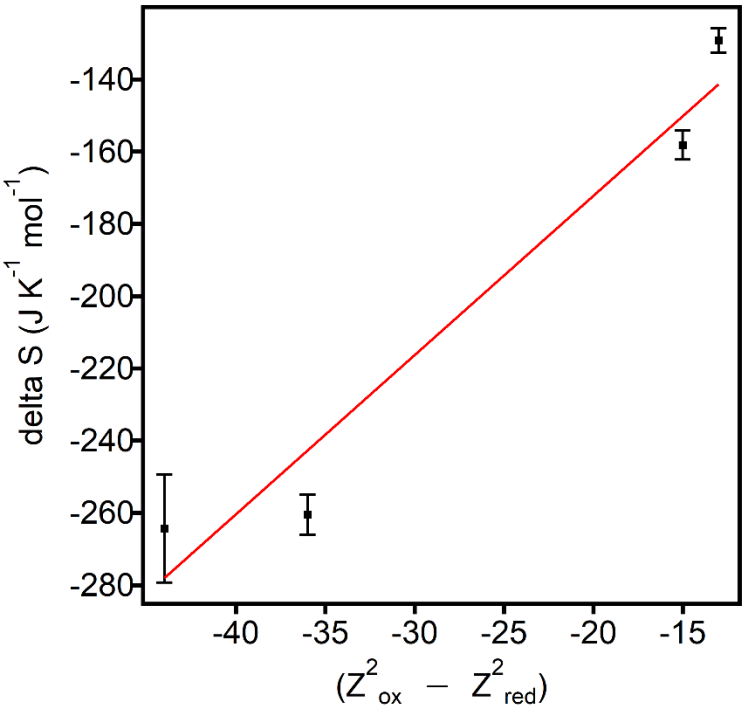
Supplemental Figure 4.4. Cyclic voltammograms of 1 mM $\{P_2W_{18}\}$ in 0.1 M sodium acetate (pH = 3.5) collected at 2 and 49 °C. The violet voltammogram was taken after cooling down the solution from 49 °C to 2 °C.



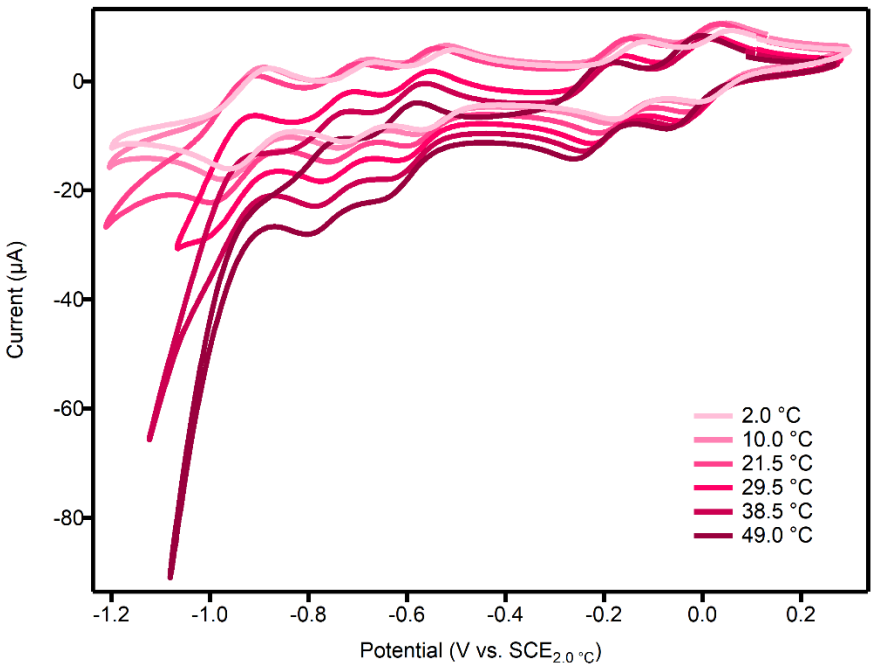
Supplemental Figure 4.5. Variable-temperature cyclic voltammograms of 1 mM $\{P_2W_{18}\}$ in 0.1 M sodium acetate (pH = 3.5) collected at 2.0 – 48.5 °C with a sweep rate of 100 mV/s.



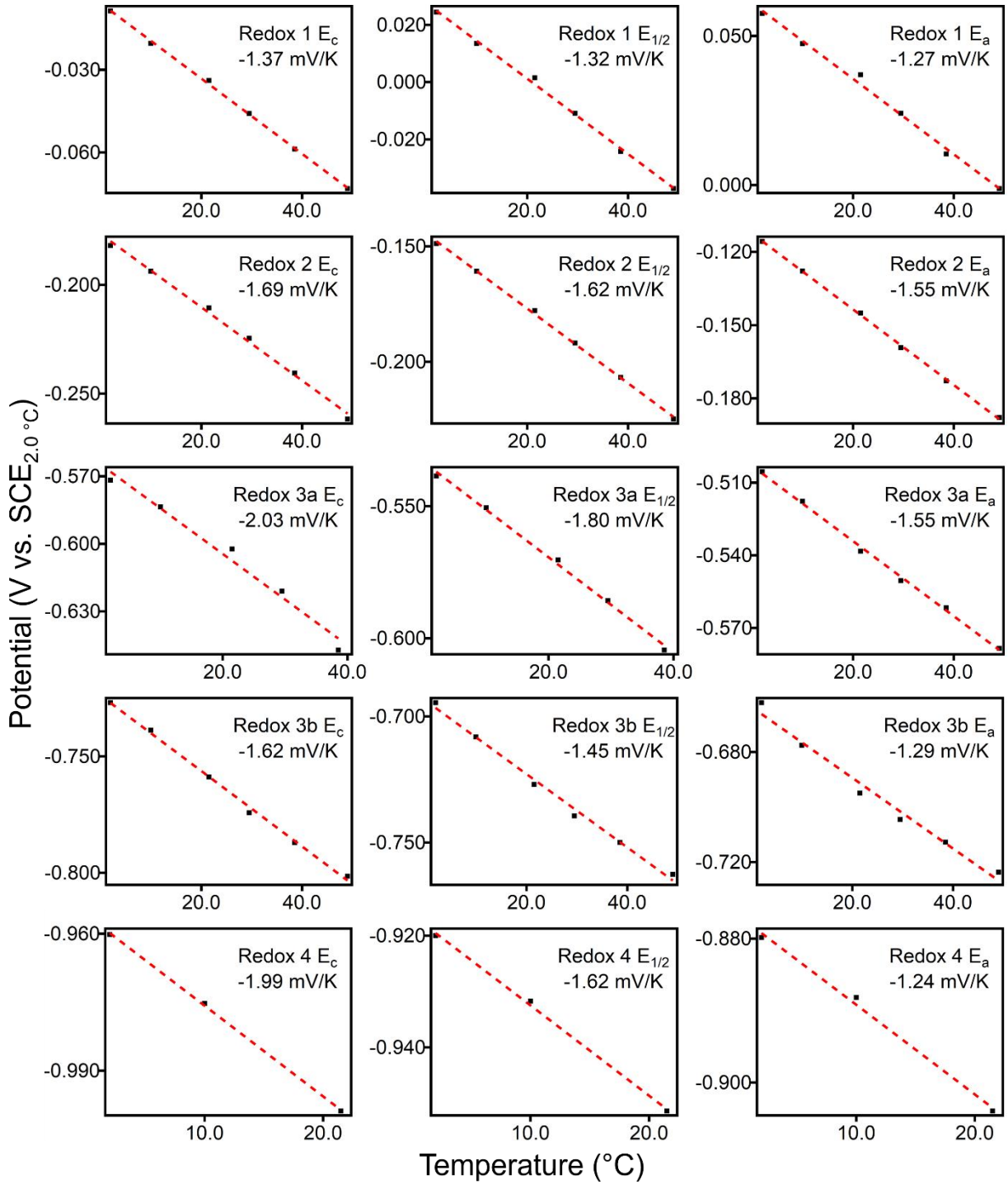
Supplemental Figure 4.6. Rates of cathodic peak (left column), half-wave (middle column), and anodic peak (right column) potential shifts per unit temperature change, extracted from VTCVs on 1 mM $\{P_2W_{18}\}$ in 0.1 M sodium acetate (pH = 3.5) for each redox process.



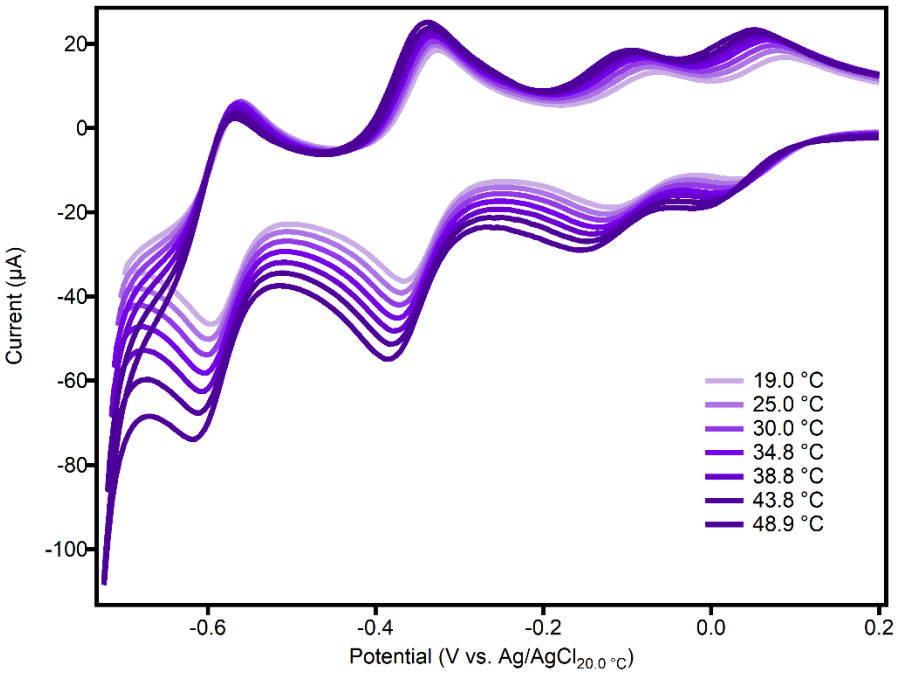
Supplemental Figure 4.7. ΔS_{rc} as a function of $Z_{ox}^2 - Z_{red}^2$ for $\{P_2W_{18}\}$.



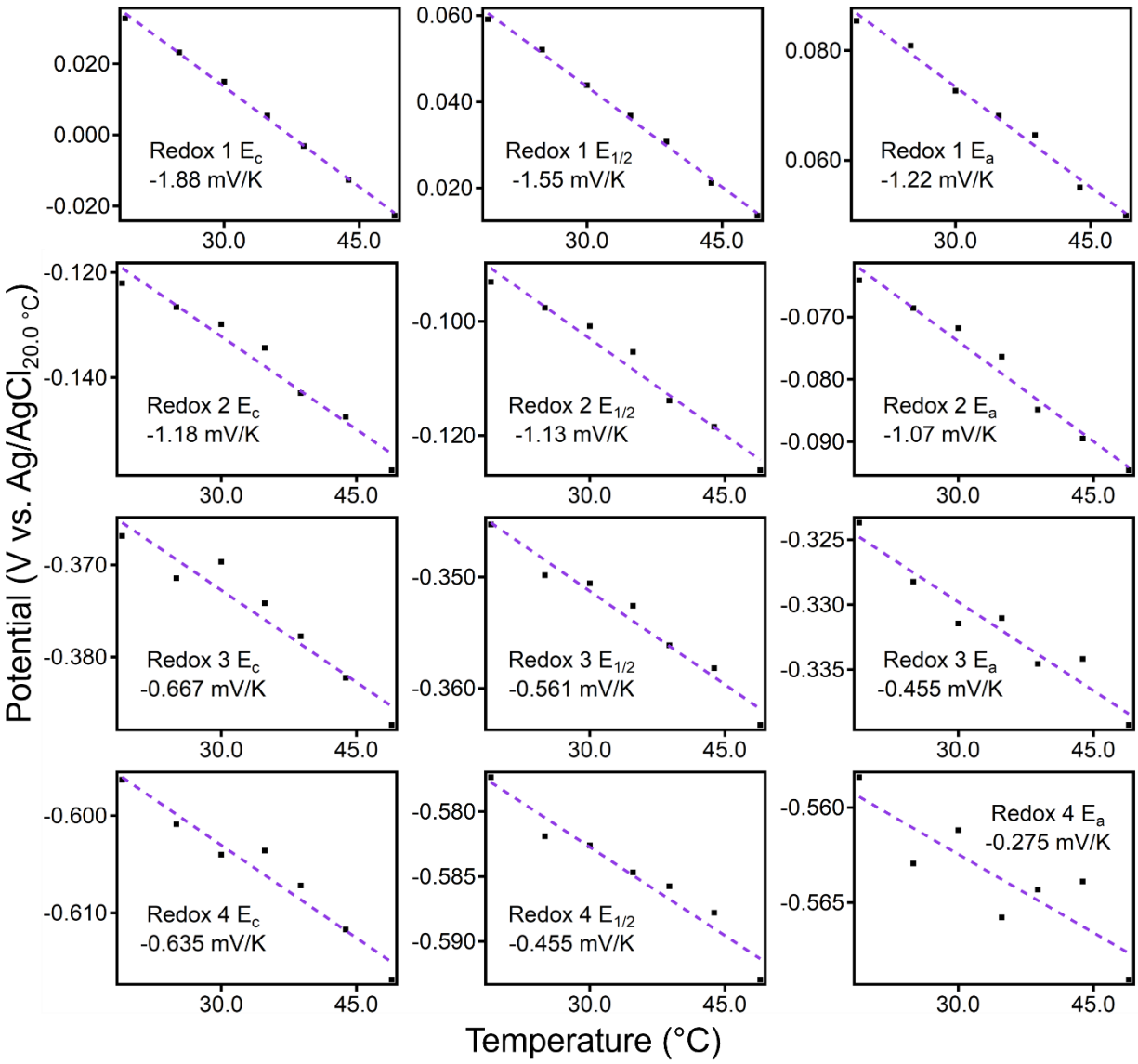
Supplemental Figure 4.8. Variable-temperature cyclic voltammograms of 1 mM $\{P_2W_{18}\}$ in 0.1 M sodium acetate (pH = 5.9) collected at 2.0 – 49.0 °C with a sweep rate of 100 mV/s.



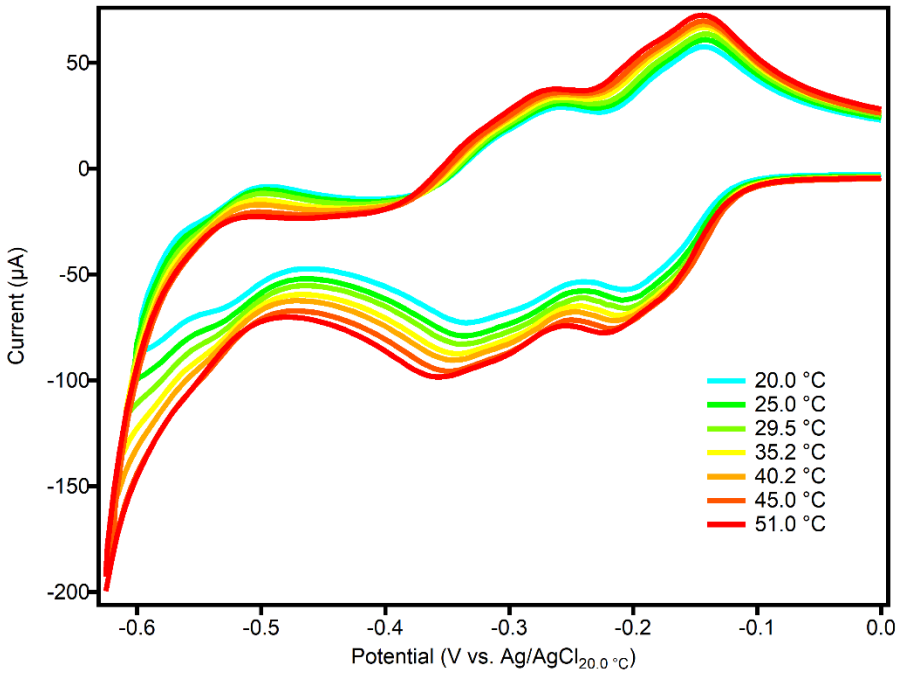
Supplemental Figure 4.9. Rates of cathodic peak (left column), half-wave (middle column), and anodic peak (right column) potential shifts per unit temperature change, extracted from VTCVs on 1 mM $\{P_2W_{18}\}$ in 0.1 M sodium acetate (pH = 5.9) for each redox process.



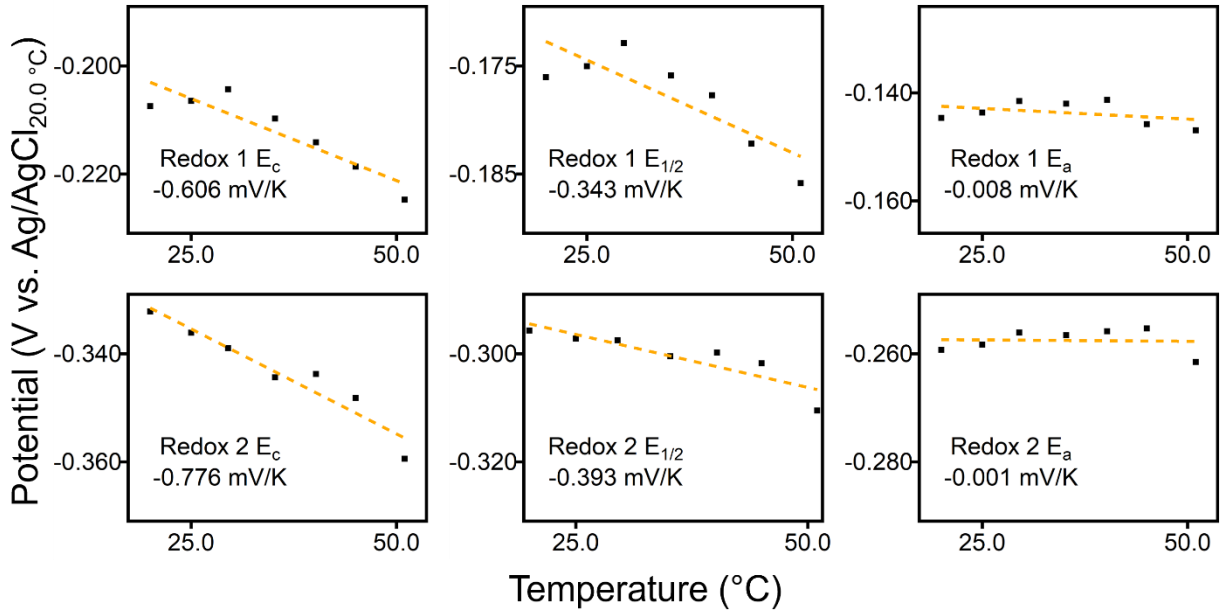
Supplemental Figure 4.10. VTCVs of 1 mM $\{P_2W_{18}\}$ in 1 M HCl(aq) collected at 19.0 – 48.9 °C temperature range with a sweep rate of 100 mV/s.



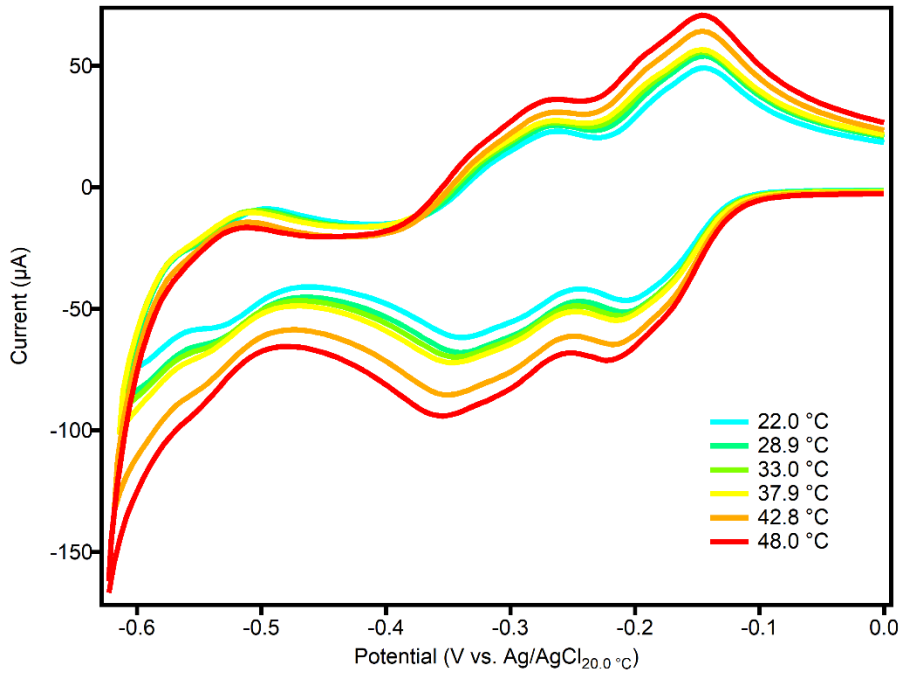
Supplemental Figure 4.11. Rates of cathodic peak (left column), half-wave (middle column), and anodic peak (right column) potential shifts per unit temperature change, extracted from VTCVs on 1 mM $\{P_2W_{18}\}$ in 1 M HCl(aq) for each redox process.



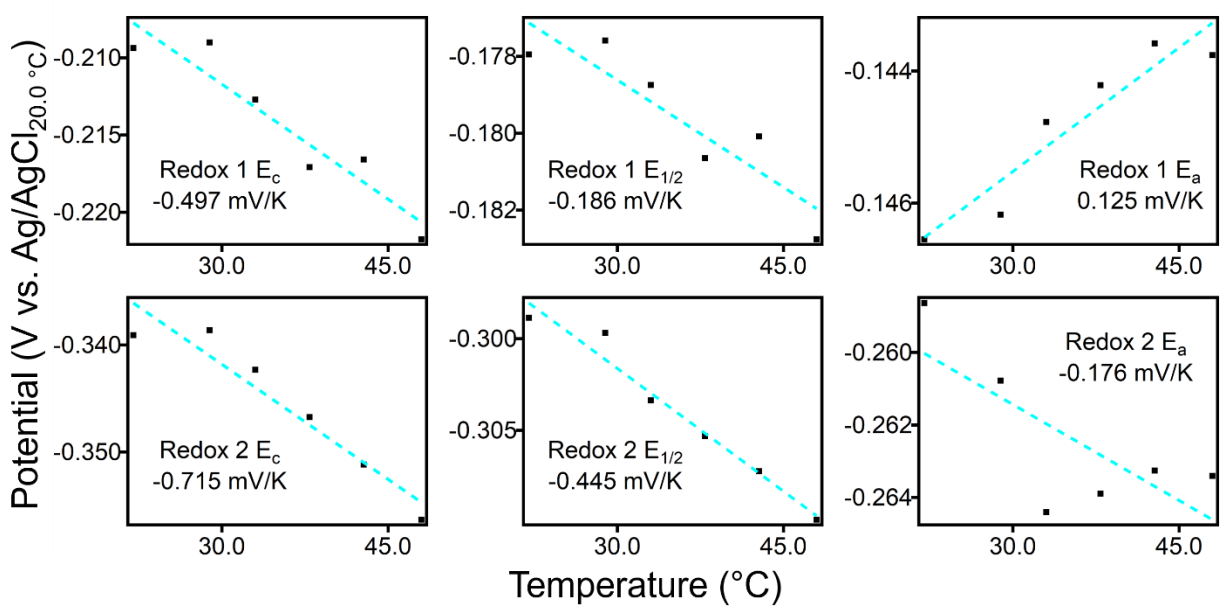
Supplemental Figure 4.12. Variable-temperature cyclic voltammograms of 1 mM $\{P_5W_{30}\}$ in 1 M HCl(aq) collected at 20.0 – 51.0 °C with a sweep rate of 100 mV/s.



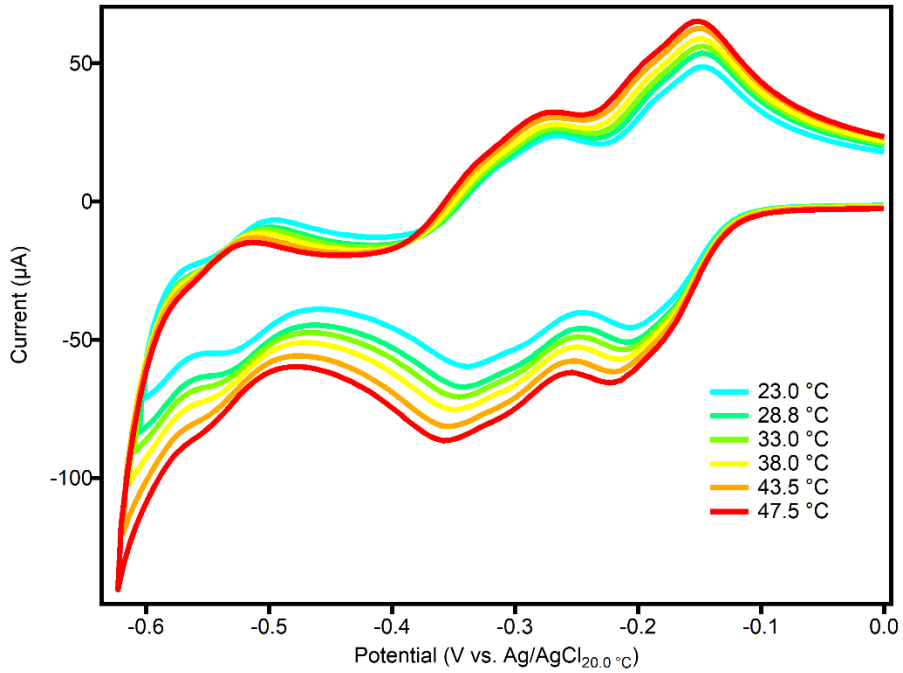
Supplemental Figure 4.13. Rates of cathodic peak (left column), half-wave (middle column), and anodic peak (right column) potential shifts per unit temperature change, extracted from VTCVs on 1 mM $\{P_5W_{30}\}$ in 1 M HCl(aq) for the first two redox processes.



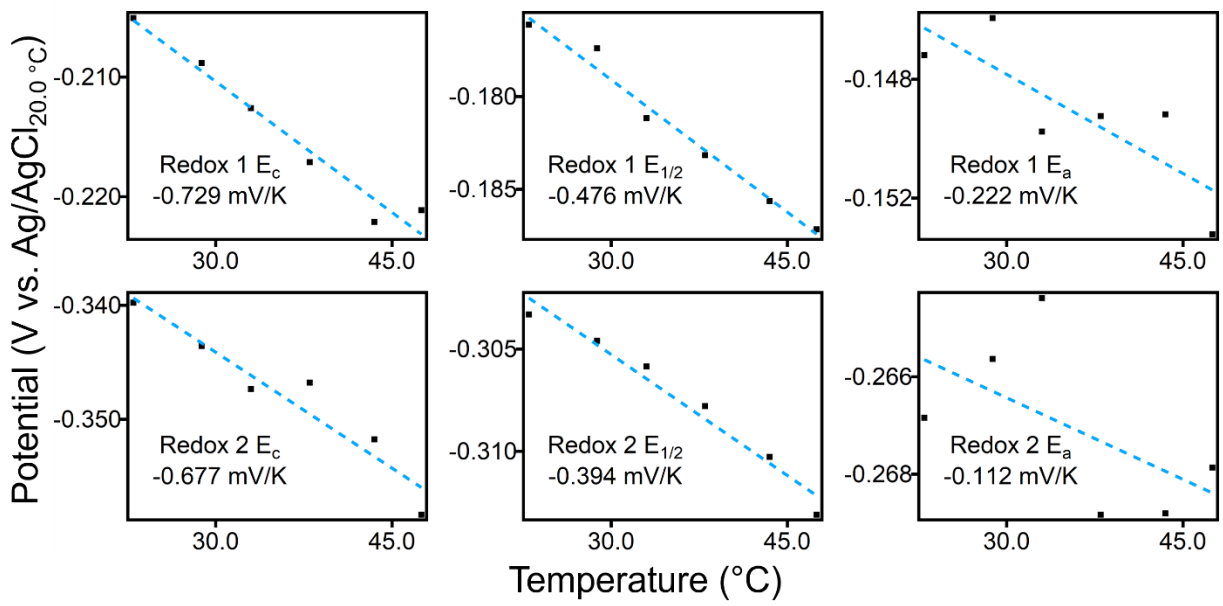
Supplemental Figure 4.14. Variable-temperature cyclic voltammograms of 1 mM $\{P_5W_{30}\}$ solution prepared in 1 M HCl(aq) with 50 mM KCl, measured in the temperature range of 22.0 – 48.0 °C at a sweep rate of 100 mV/s.



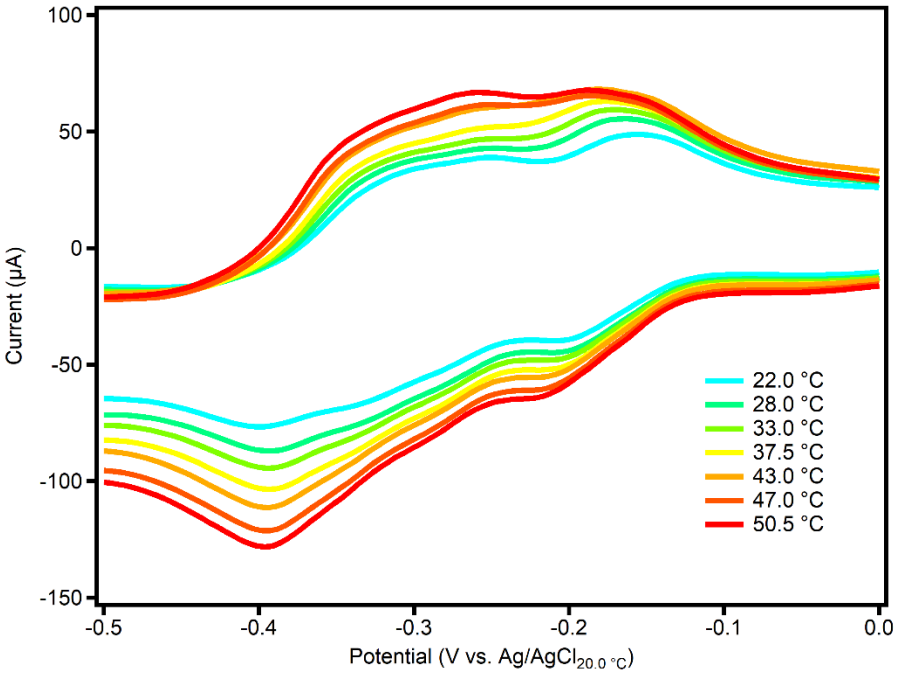
Supplemental Figure 4.15. Rates of cathodic peak (left column), half-wave (middle column), and anodic peak (right column) potential shifts per unit temperature change, extracted from VTCVs on 1 mM $\{P_5W_{30}\}$ in 1 M HCl(aq) with 50 mM KCl for the first two redox processes.



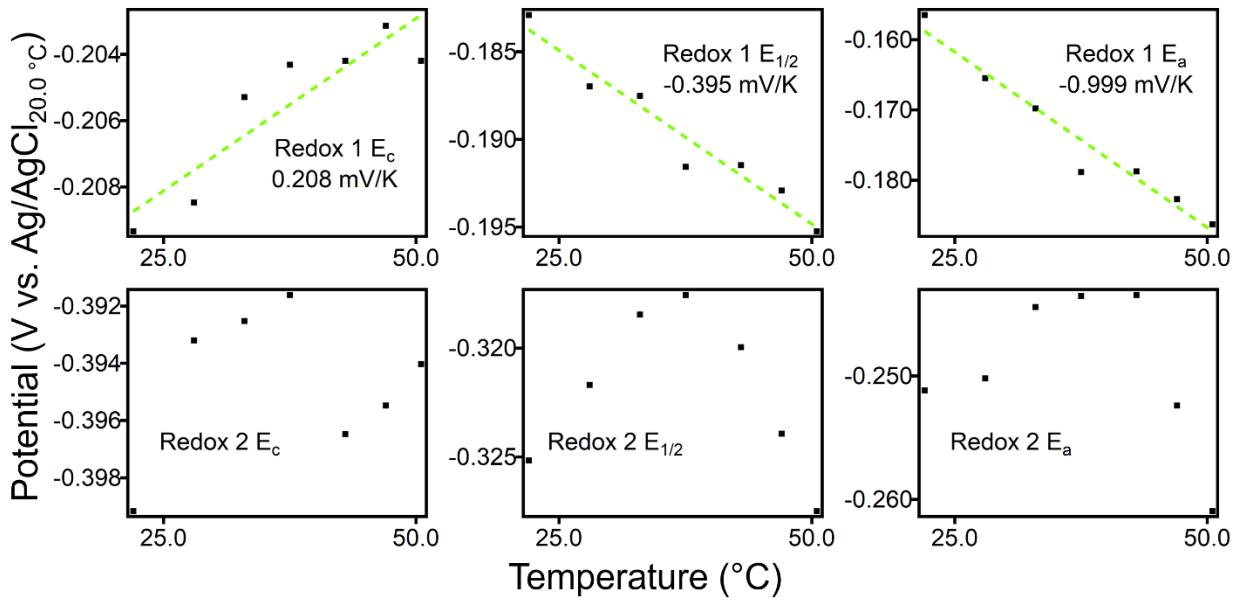
Supplemental Figure 4.16. Variable-temperature cyclic voltammograms of 1 mM $\{P_5W_{30}\}$ solution prepared in 1 M HCl(aq) with 100 mM KCl, measured in the temperature range of 22.0 – 48.0 °C at a sweep rate of 100 mV/s.



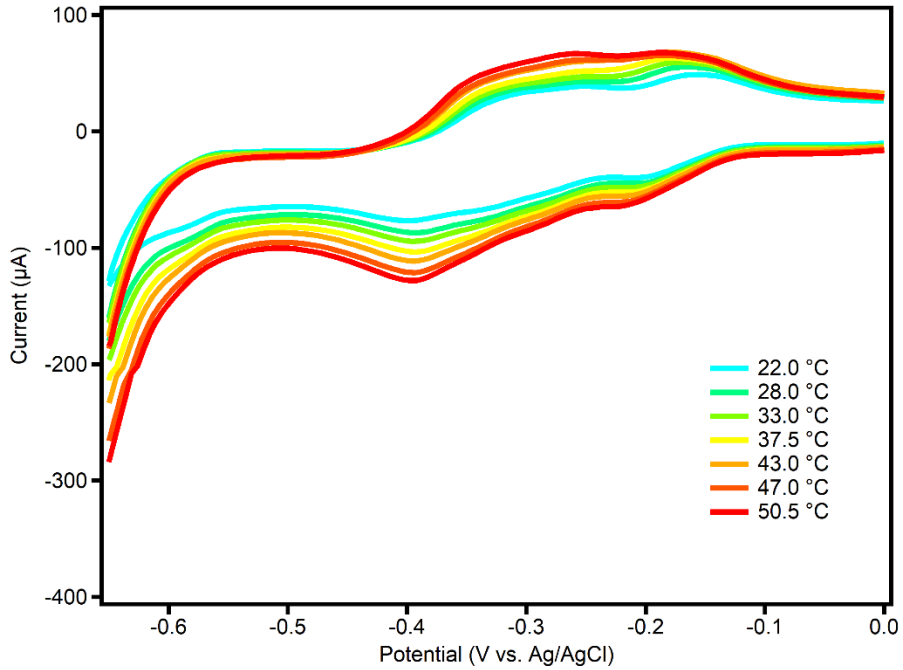
Supplemental Figure 4.17. Rates of cathodic peak (left column), half-wave (middle column), and anodic peak (right column) potential shifts per unit temperature change, extracted from VTCVs on 1 mM $\{P_5W_{30}\}$ in 1 M HCl(aq) with 100 mM KCl for the first two redox processes.



Supplemental Figure 4.18. Variable-temperature cyclic voltammograms of 1 mM $\{P_5MoW_{29}\}$ solution prepared in 1 M HCl(aq) collected in 22.0 – 50.5 °C temperature range with 100 mV/s sweep rate. Only the first two redox processes are represented in this plot.



Supplemental Figure 4.19. (Top row) Rates of cathodic peak (left column), half-wave (middle column), and anodic peak (right column) potential shifts per unit temperature change, extracted from VTCVs on 1 mM $\{P_5MoW_{29}\}$ in 1 M HCl(aq) for the first redox process. (Bottom row) Cathodic peak, half-wave, and anodic peak potentials measured at varied temperatures for the second redox process are shown without linear fits.



Supplemental Figure 4.20. Full representations of variable-temperature cyclic voltammograms of 1 mM $\{P_5MoW_{29}\}$ solution in 1 M HCl(aq).

REFERENCES

(1) Hur, S.; Kim, S.; Kim, H.-S.; Kumar, A.; Kwon, C.; Shin, J.; Kang, H.; Sung, T. H.; Ryu, J.; Baik, J. M.; Song, H.-C. Low-Grade Waste Heat Recovery Scenarios: Pyroelectric, Thermomagnetic, and Thermogalvanic Thermal Energy Harvesting. *Nano Energy* **2023**, *114*, 108596. https://doi.org/10.1016/j.nanoen.2023.108596.

(2) Lee, S. W.; Yang, Y.; Lee, H.-W.; Ghasemi, H.; Kraemer, D.; Chen, G.; Cui, Y. An Electrochemical System for Efficiently Harvesting Low-Grade Heat Energy. *Nat Commun* **2014**, *5* (1), 3942. https://doi.org/10.1038/ncomms4942.

(3) Sahami, S.; Weaver, M. J. Entropic and Enthalpic Contributions to the Solvent Dependence of the Thermodynamics of Transition-Metal Redox Couples: Part II. Couples Containing Ammine and Ethylenediamine Ligands. *Journal of Electroanalytical Chemistry and Interfacial Electrochemistry* **1981**, *122*, 171–181. https://doi.org/10.1016/S0022-0728(81)80148-9.

(4) Svensson Grape, E.; Huang, J.; Roychowdhury, D.; Debela, T. T.; Chang, H.; Jenkins, A.; Schimpf, A. M.; Hendon, C. H.; Brozek, C. K. Converting Heat to Electrical Energy Using Highly Charged Polyoxometalate Electrolytes. *ACS Appl. Energy Mater.* **2024**. https://doi.org/10.1021/acsaem.4c00036.

(5) Duan, J.; Feng, G.; Yu, B.; Li, J.; Chen, M.; Yang, P.; Feng, J.; Liu, K.; Zhou, J. Aqueous Thermogalvanic Cells with a High Seebeck Coefficient for Low-Grade Heat Harvest. *Nat Commun* **2018**, *9* (1), 5146. https://doi.org/10.1038/s41467-018-07625-9.

(6) Buckingham, M. A.; Marken, F.; Aldous, L. The Thermoelectrochemistry of the Aqueous Iron(II)/Iron(III) Redox Couple: Significance of the Anion and pH in Thermogalvanic Thermal-to-Electrical Energy Conversion. *Sustainable Energy Fuels* **2018**, *2* (12), 2717–2726. https://doi.org/10.1039/C8SE00416A.

(7) Pope, M. T. Heteropoly and Isopoly Anions as Oxo Complexes and Their Reducibility to Mixed-Valence Blues. *Inorg. Chem.* **1972**, *11* (8), 1973–1974. https://doi.org/10.1021/ic50114a057.

(8) Gumerova, N. I.; Rompel, A. Synthesis, Structures and Applications of Electron-Rich Polyoxometalates. *Nature Reviews Chemistry* **2018**, *2* (2), 1–20. https://doi.org/10.1038/s41570-018-0112.

(9) Creaser, I.; Heckel, M. C.; Neitz, R. J.; Pope, M. T. Rigid Nonlabile Polyoxometalate Cryptates [ZP5W30O110](15-n)- That Exhibit Unprecedented Selectivity for Certain Lanthanide and Other Multivalent Cations. *Inorg. Chem.* **1993**, *32* (9), 1573–1578. https://doi.org/10.1021/ic00061a010.

(10) Wang, Y.; Liu, C.; Wang, Y.; Zhu, C.; Chen, X.; Liu, B. Efficient Photo-Thermo-Electric Conversion Using Polyoxovanadate in Ionic Liquid for Low-Grade Heat Utilization. *ChemSusChem* **2021**, *14* (24), 5434–5441. https://doi.org/10.1002/cssc.202101532.

(11) Mbomekalle, I.-M.; Lu, Y. W.; Keita, B.; Nadjo, L. Simple, High Yield and Reagent-Saving Synthesis of Pure α-K6P2W18O62·14H2O. *Inorganic Chemistry Communications* **2004**, *7* (1), 86–90. https://doi.org/10.1016/j.inoche.2003.10.011.

(12) Hayashi, A.; Haioka, T.; Takahashi, K.; Bassil, B. S.; Kortz, U.; Sano, T.; Sadakane, M. Cation Effect on Formation of Preyssler-Type 30-Tungsto-5-Phosphate: Enhanced Yield of Na-Encapsulated Derivative and Direct Synthesis of Ca- and Bi-Encapsulated Derivatives. *Zeitschrift für anorganische und allgemeine Chemie* **2015**, *641* (15), 2670–2676. https://doi.org/10.1002/zaac.201500679.

(13) Turo, M. J.; Chen, L.; Moore, C. E.; Schimpf, A. M. Co2+-Linked [NaP5W30O110]14−: A Redox-Active Metal Oxide Framework with High Electron Density. *J. Am. Chem. Soc.* **2019**, 5.

(14) Pope, M. T.; Papaconstantinou, E. Heteropoly Blues. II. Reduction of 2:18-Tungstates. *Inorg. Chem.* **1967**, *6* (6), 1147–1152. https://doi.org/10.1021/ic50052a018.

(15) Briand, L. E.; Valle, G. M.; Thomas, H. J. Stability of the Phospho-Molybdic Dawson-Type Ion P2Mo18O626– in Aqueous Media. *J. Mater. Chem.* **2002**, *12* (2), 299–304. https://doi.org/10.1039/b106769a.

(16) Chen, J.-J.; Vilà-Nadal, L.; Solé-Daura, A.; Chisholm, G.; Minato, T.; Busche, C.; Zhao, T.; Kandasamy, B.; Ganin, A. Y.; Smith, R. M.; Colliard, I.; Carbó, J. J.; Poblet, J. M.; Nyman, M.; Cronin, L. Effective Storage of Electrons in Water by the Formation of Highly Reduced Polyoxometalate Clusters. *J. Am. Chem. Soc.* **2022**, *144* (20), 8951–8960. https://doi.org/10.1021/jacs.1c10584.

(17) Fernandes, D. M.; Araújo, M. P.; Haider, A.; Mougharbel, A. S.; Fernandes, A. J. S.; Kortz, U.; Freire, C. Polyoxometalate-Graphene Electrocatalysts for the Hydrogen Evolution Reaction. *ChemElectroChem* **2018**, *5* (2), 273–283. https://doi.org/10.1002/celc.201701210.

(18) Huang, M.; Bi, L.; Shen, Y.; Liu, B.; Dong, S. Nanocomposite Multilayer Film of Preyssler-Type Polyoxometalates with Fine Tunable Electrocatalytic Activities. *J. Phys. Chem. B* **2004**, *108* (28), 9780–9786. https://doi.org/10.1021/jp0494335.

(19) Antonio, M. R.; Nyman, M.; Anderson, T. M. Direct Observation of Contact Ion-Pair Formation in Aqueous Solution. *Angewandte Chemie International Edition* **2009**, *48* (33), 6136–6140. https://doi.org/10.1002/anie.200805323.

(20) Leroy, F.; Miró, P.; Poblet, J. M.; Bo, C.; Bonet Ávalos, J. Keggin Polyoxoanions in Aqueous Solution: Ion Pairing and Its Effect on Dynamic Properties by Molecular Dynamics Simulations. *J. Phys. Chem. B* **2008**, *112* (29), 8591–8599. https://doi.org/10.1021/jp077098p.

(21) Zhang, Q.; Chen, H.; Wu, T.; Jin, T.; Pan, Z.; Zheng, J.; Gao, Y.; Zhuang, W. The Opposite Effects of Sodium and Potassium Cations on Water Dynamics. *Chemical Science* **2017**, *8* (2), 1429. https://doi.org/10.1039/c6sc03320b.

(22) Mancinelli, R.; Botti, A.; Bruni, F.; Ricci, M. A.; Soper, A. K. Hydration of Sodium, Potassium, and Chloride Ions in Solution and the Concept of Structure Maker/Breaker. *J. Phys. Chem. B* **2007**, *111* (48), 13570–13577. https://doi.org/10.1021/jp075913v.

(23) Alizadeh, M. H.; Harmalker, S. P.; Jeannin, Y.; Martin-Frere, J.; Pope, M. T. A Heteropolyanion with Fivefold Molecular Symmetry That Contains a Nonlabile Encapsulated Sodium Ion. The Structure and Chemistry of [NaP5W30O110]14-. *J. Am. Chem. Soc.* **1985**, *107* (9), 2662–2669. https://doi.org/10.1021/ja00295a019.

(24) Chen, L.; San, K. A.; Turo, M. J.; Gembicky, M.; Fereidouni, S.; Kalaj, M.; Schimpf, A. M. Tunable Metal Oxide Frameworks via Coordination Assembly of Preyssler-Type Molecular Clusters. *J. Am. Chem. Soc.* **2019**, *141* (51), 20261–20268. https://doi.org/10.1021/jacs.9b10277.